UNIVERSITÀ DEGLI STUDI DI MILANO
SCUOLA DI SPECIALIZZAZIONE IN FISICA MEDICA
FACOLTÀ DI MEDICINA E CHIRURGIA

Clinical implementation of MRI-only radiotherapy treatment workflow for prostate cancer with a standard linac

Relatore: Prof. Cristina Lenardi
Correlatore: Dott. Angelo Filippo Monti
Correlatore: Dott. Domenico Lizio

Tesi di Specializzazione di:
Marco Maria Jacopo Felisi
Matr. S61578

Anno Accademico 2018-2019

TABLE OF CONTENTS

ABSTRACT iii
Background and Aim iii
Material and Methods iii
Results and Discussions iv
Conclusions v
INTRODUCTION 1
1.1. Background 1
1.2. Clinical implementation of an MRI-only workflow 2
1.2.1. MR Imaging 3
1.2.2. Contour delineation and sCT generation 4
1.2.3. Dosimetric evaluation of treatment planning 6
1.2.4. Patient setup verification 6
1.3. Aim of the thesis 6
MATERIALS AND METHODS 8
2.1. MRI-only workflow 8
2.2. MR Imaging 9
2.2.1. MR Sequence 9
2.2.2. Acquisition Setup 12
2.2.3. Geometric Distortions 16
2.3. Contour Delineation and sCT generation 18
2.3.1. ADMIRE 20
2.3.2. Electron Densities 23
2.4. Dosimetric Evaluation 23
2.4.1. Dose Volume Histogram (DVH) 26
2.4.2. Gamma Analysis 26
2.5. Patient Setup Verification 27
RESULTS 30
3.1. MR Imaging 30
3.1.1. MR Sequence 30

3.1.2. Acquisition Setup 30
3.1.3. Geometric Distortions 31
3.2. Contour Delineation and sCT generation 32
3.2.1. Electron Densities 33
3.3. Dosimetric Evaluation 34
3.4. Patient Setup Verification 44
DISCUSSIONS 46
4.1. MR Imaging 46
4.2. Contour Delineation and sCT generation 47
4.3. Dosimetric Evaluation 48
4.4. Patient Setup Verification 50
4.5. Benefits and Drawbacks 50
CONCLUSIONS 52
REFERENCES 54
ADDENDUM 65
Abstract 65
Background and Aim 65
Material and Methods 66
Results 67
Discussions 68
Conclusion 69
Addendum References 70
ACKNOWLEDGMENTS 72

ABSTRACT

BACKGROUND AND AIM

The purpose of this work is the clinical implementation of radiotherapy treatment workflow for prostate cancer based only on MRI images (MRI-only) with a standard linac, using the technological tools available in a big general hospital. In the recent years the growing interest in using solely MRI images, due to the excellent soft tissue contrast that makes it unique, both for identification and precise delineation of target volumes and organs at risk (OAR), emerged strongly. Especially in those regions characterized by soft tissues, as the pelvis site, the method has several benefits, including improvement of inter-observer robustness in target delineation, a reduction in contoured structures which potentially leads to smaller irradiated volumes and a major efficiency of the workflow by both reducing the time and costs of patients imaging and removing residual registration error compared to a CT/MR workflow.

However, there are several challenges in the implementation and application of MRI-only workflow; the most important one is the Electron Densities (ED) estimation. In fact, unlike CT images, where the voxels intensities are directly linked to the physical properties of the tissues ED, required by the Treatment Planning System (TPS) for dose calculation, MRI signals do not depend on ED but correlate with tissue proton density and thus cannot be directly used. Therefore, it is mandatory to convert MRI data to ED maps to allow the dose distribution even in this case. These generated maps are known as *synthetic CT* (sCT).

Several aspects of the implementation have been examined in this thesis in order to validate the overall workflow.

MATERIAL AND METHODS

Imaging acquisition was performed using a 3D T1 VIBE Dixon gradient echo sequence that is a good compromise between image quality and acquisition time; it takes 2 minutes and 30 seconds and provides 4 contrasts (Water, Fat, In-phase and Out-of-phase) useful for the visualization of target and different OARs. The acquisition on the MR scanner was possible thanks to the use of a home-made table-top, commercial MR safe markers and properly controlled internal laser system; furthermore, the geometric distortions in obtained images were evaluated.

A hybrid method was adopted to generate sCT from MRI; it consists in a combination of bulk ED and multi atlas-based approach. For this purpose, the MR images of 20 volunteers and patients undergoing diagnostic acquisitions were collected, manually contoured in bones and main OARs, and then inserted, after verification by a radiation oncologist, as reference in the database of ADMIRE software (research version 1.13.5, Elekta AB, Stockholm, Sweden), utilized for automatic contouring process. The software approximates the anatomy contours by comparing several individual atlases, applying elements of maximum likelihood forms to a new patient image-set, and creates a structure set to fit the actual patient's anatomy. Therefore, sCTs were finally generated in the TPS by assigning to each structure bulk ED values, calculated averaging over 20 patients who previously underwent prostate radiotherapy.

Once the sCT was generated, different evaluations were made using quantitative methods such as dose-volume histogram (DVH) and 2D local gamma analysis, in order to test the dose differences between the sCT and the gold standard CT, both in terms of homogeneous EDs assignment and contours delineated on the MR images.
At first, 20 VMAT prostate treatment plans, calculated on standard CT images with 10 MV X-rays, were recalculated using the same field, segments and monitor unit (MU) arrangements on the sCT, where only fixed EDs were assigned instead of the heterogenous ones.
Afterwards, the combination between the assignment of an average ED and the different contours in the two imaging modalities was evaluated for 7 patients undergoing both CT and MR acquisitions. The optimized plans, calculated on the CT images, were first copied using the same field, segment and MU arrangements and recalculated on the sCTs, obtained by MRI, and thus were optimized again keeping the same plan constraints as CT-based ones.
Finally, the feasibility of patient positioning in the linac room using CBCT-MR matching was verified. For 9 selected images of different fractions and patients, the shifts obtained through CT-CBCT registration were compared to the those resulting from the evaluations of three radiation oncologists, who blindly and manually matched the CBCT images with those from MRI.

RESULTS AND DISCUSSIONS

The MR sequence used for this work was optimized in order to achieve adequate image quality in a reasonable time, reducing the artifacts and minimizing the patient discomfort.
Furthermore, the internal laser system of the MRI scanner, used patient positioning, was checked. It was verified that the laser cross, projected from a single point inside the scanner, was centered in the isocenter and not tilted. The mean tilt angle was 0.3°± 0.2° (range 0.2° to 0.4°) in all positions tested, corresponding to difference approximately of 1±0.4 mm at 15-20 cm from the isocenter.
In addition, the geometric distortions, evaluated in the absence of the patient less than 2 mm, are minimized by the active shimming system of the scanner.
The auto-contouring delineation process performed by ADMIRE (research version 1.13.5, Elekta AB, Stockholm, Sweden) was executed in an average time of approximatively 20 minutes and considered satisfactory by radiation oncologists; further 5 to 10 minutes were needed to better define some contours and to identify the target.
Regarding the evaluation made on the same CT images, where only the EDs were changed, the mean deviation of PTV and OARs DVH parameters were approximately 0.5%, except for the rectum were the percentage difference reached higher values (D_{mean} of 1% and V40 of 2.4%) due to different filling. In addition, further evaluations performed by 2D local γ-analysis resulted in average passing rate from 98.5% to 99.4% in the three views, using an acceptance criterion of 2%-2mm.
On the sCT obtained by MR images, despite the mean percentage differences in PTV coverage were limited, below the 1% in the first case and around 0.5% in the second one, the differences for OARs were considerably higher; mean percentage differences for bladder and femoral heads were approximatively -25% and -2% in both the described steps, while D_{mean} of rectum ranged from +11.5% to +4% and V40 passed from +26% to +8%.
Anyhow, this issue is not relevant in the implementation of the workflow, as only MRI acquisitions will be made for planning purposes. Rather, this behaviour is representative of the differences in

filling of different OARs, such as rectum and bladder, between two consecutive fractions of the treatment.
Moreover, however, the PTV and OARs compliance with the constraints, used in our center, was evaluated for the re-optimized plans: for 7 patients and 8 different parameters, only 1 time over 56 a constraint exceeded the limits.
Finally, as far as the matching between CBCT-MR for patient positioning before each treatment fraction, the averaged differences in displacements respect to standard CT-based method, resulted 2.8±1.7 mm, 3.8±1.6 mm and 0.1±1.4 mm for transverse, longitudinal and vertical directions respectively, despite the physiological differences of the rectum and bladder between the two imaging modalities.

CONCLUSIONS

This study demonstrates that MRI-only workflow for prostate patients seems to be feasible using the clinical optimized method, providing a better contrast in the structures of clinical interest. Therefore, the future goal is to gradually move towards the use of MRI-only in the clinical routine. Meanwhile, the proposed method will be used for special cases, such as patient with metal hip prosthesis.

INTRODUCTION

1.1. BACKGROUND

Magnetic Resonance Imaging (MRI) has been used as a support for radiotherapy (RT) treatment planning for a long time, since it provides superior soft tissue contrast over the gold standard Computed Tomography (CT) [1-9]. In the last few years, the idea of developing a radiotherapy treatment planning technique using exclusively Magnetic Resonance Imaging (MRI-only) has emerged strongly, as also shown by the increase number of MRI-linear accelerators (MRI-linac) in several cancer centers [10-25]. This innovative method, which aims to completely replace the classical CT planning approach, has various benefits, especially in those regions characterized by soft tissues, where CT images can lead to difficult delineations of both targets and organ at risks (OARs) [7, 26], as shown in Fig. 1. The main anatomical areas where the advantage of using MRI is of considerable importance, both from a diagnostic point of view and for radiotherapy treatment planning, are brain, head and neck, liver, pancreas, spine and pelvis [19]. In particular, the tumor of prostate, endemic cancer in the male population with over 100 cases diagnosed every day in Italy [27], is the most studied case.

In addition to the gain in volume definitions accuracy, both for target and OARs, the benefits of using MRI as the only imaging modality for treatment planning include improvement of inter-observer robustness in target delineation [28-33], a reduction in contoured volumes [6, 30, 34, 35, 36, 37], which potentially leads to smaller irradiated volumes and hence a lower dose to the surrounding OARs, as rectum and bladder, and a major efficiency of the workflow by reducing the time and costs of patients imaging [25]. Moreover, the registration between MRI, commonly used for contouring purposes, with the planning CT leads to systematic geometric errors, estimated to be 2-3 mm [28, 31, 38]: these uncertainties are removed with only one imaging modality.

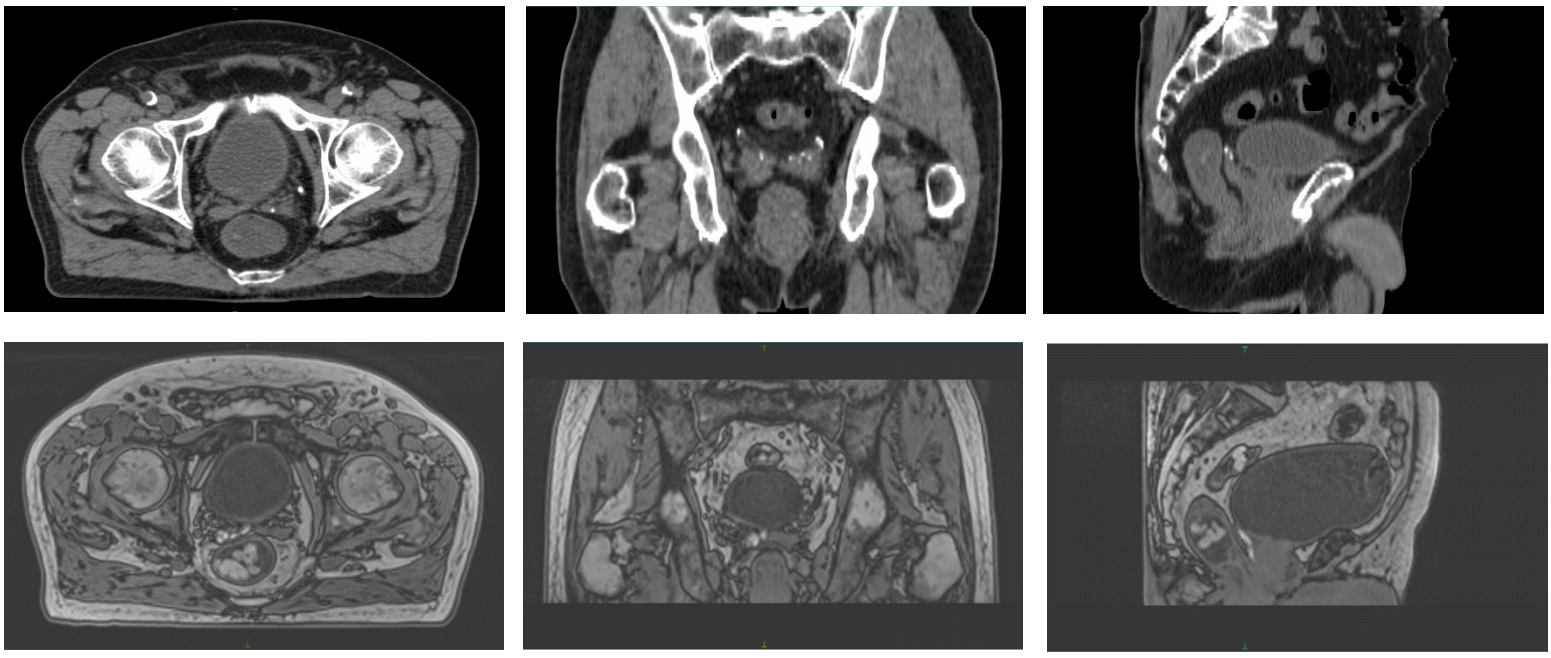

Fig. 1: CT images (top row) vs MR ones (bottom row) used for planning purpose in our hospital.

However, there are several challenges in the implementation and application of MRI-only workflow, as it will be detailed in the paragraph 1.2; the most important one is the Electron Densities (ED) estimation. In fact, unlike CT images, where the voxels intensities are directly linked to the physical properties of the tissues ED, required by the Treatment Planning System (TPS) for dose calculation, MRI signals do not depend on the ED but correlate with tissue proton density and thus cannot be directly used [24, 39]. Therefore, it is mandatory to convert MRI data to ED or Hounsfield Unit (HU) maps to allow the dose distribution even in this case. These generated maps are known as *synthetic CT* (sCT) or *pseudo CT*; we will adopt the term sCT throughout the text.

1.2. CLINICAL IMPLEMENTATION OF AN MRI-ONLY WORKFLOW

In recent years, it is possible to find in the literature an increasing number of publications on MRI-only RT topic. Some groups worked on the clinical implementation of an MRI-only workflow for prostate cancer radiotherapy [12, 14, 18, 23, 25, 40, 41], while others focused only on very specific topics, for example MRI-based dose calculation or patient set-up strategy [42-46].
However, there are few radiotherapy centers around the world that implemented an MRI-only workflow for the prostate cancer, as reported below in Table 1.

Author / Reference	Center	Year	Number of Patients Treated
Christiansen et al. [12]	Odense University Hospital, Odense, Denmark	2017	1
Tyagi et al. [25]	Memorial Sloan Kettering Cancer Center, New York, USA	2017	42
Koninklijke [41]	Turku University Hospital, Turku, Finland	2017	91
Kerkmeijer et al. [18]	University Medical Center, Utrecht, The Netherlands	2018	-
Tenhunen et al. [40]	Helsinki University Hospital, Helsinki, Finland	2018	125
Persson et al. [23]	Skåne University Hospital, Lund, Sweden	2018 - 2020	39

Greer et al. [14]	Calvary Mater Hospital, Newcastle, Australia Liverpool Hospital Cancer Therapy Centre, Sydney, Australia	2019	23

Tab. 1: List of centers that implemented MRI-only workflow for prostate cancer.

The clinical implementation of any new workflow must to be properly validated, considering each step necessary to build it [11, 21, 23, 47, 48]. The workflow can be divided as follow: MR Imaging, contour delineation and sCT generation, dosimetric evaluation of treatment planning and patient setup verification.

1.2.1. MR IMAGING

The first task is composed of different aspects: the choice of the most suitable MR sequence, the patient positioning in the scanner, with suitable markers, laser system and the relative immobilization devices, the checking of geometric accuracy of obtained MR images.
Several types of MRI sequences and techniques are reported in the literature for the purpose of this work. They can be divided into four main categories, depending on the contrast: T1-weighted (T1w), T2-weighted (T2w), ultra-short echo time (UTE) and Dixon family [39, 49, 50, 51].
The images of first category (T1w), with short repetition time (TR) and echo time (TE) relative to the tissue T1, are preferred for visualizing anatomy. On the other hand, T2w images have long TR and long TE, similar to tissue T2, and are suitable for visualizing pathology [52, 53, 54].
The third category, the ultra-short echo time (UTE), are used to visualize solid structures as bone, ligaments or tendons, characterized by a very short T2 relaxation time [55, 56]. However, it is not a sequence available for all vendors.
At last, the Dixon technique includes the Dixon family of fat-water separation applied on both T1w and Tw2 sequences [12, 18, 25, 48, 50, 57, 58]. This kind of sequence exploits the feature of protons' resonance frequencies in fat and water, which are offset of 3.5 parts per million (ppm), resulting in periodic opposing phase for fat and water tissues every 2.2 ms at 1.5 T. This way, using a dual echo acquisition, one of the most common and simple Dixon techniques, a first acquisition is performed with an echo time with fat and water protons in phase and subsequently a second acquisition is performed with an appropriate echo time with fat and water protons out of phase. Then, adding the in-phase to out-of-phase images water protons images are obtained (with fat signal suppressed), while subtracting them, images showing fat signal are visualized (with water signal suppressed). In the in-phase images, bones are better defined; on the contrary, with out-of-phase images edges of bladder, rectum, prostate and seminal vesicles are more clearly visible. The remaining images, fat and water, allow the clinician to evaluate other aspects in more detail.
In the literature, in some works the T2w are used [23, 52, 59], in others the Dixon are preferred [12, 16, 18, 25, 40, 48]. The first category is suggested by the ESTRO SCROP consensus guidelines [7], while the Dixon family has the advantage of providing four different contrast in a reasonable time and can be weighted towards T1 or T2. In any case, whatever the sequence chosen, the acquisition must take place with a large field of view (LFOV) geometry and preferably using a short single acquisition sequence to limit the internal OARs motion [60].

Patient positioning within the scanner is of paramount importance to ensure reproducible daily setup. To achieve this, a flat table-top and feet and knee supports are basic for prostate radiotherapy [61, 62]. In addition, MR safe external laser system and markers are necessary too; commercial products are available (for example LiquiMark™ MRI Marker Bulk, Suremark® - Simi Valley, California, USA).

Furthermore, in order to use MR images in radiotherapy planning, high geometric accuracy is needed. Magnetic field gradients provide a linear relationship between resonant frequency and position, and hence to assign signals to their spatial origins. Imperfections in the static magnetic field uniformity, eddy current and gradient linearity may lead to geometric distortion. The distortion caused by imperfection in the static magnetic field and the gradient linearity are referred as system-induced distortions. On the other hand, also patient can induce distortion caused by the different magnetic susceptibility within the patient; this effect is known as patient-induced distortions [24].

These distortions increase in magnitude with the radial distance from the isocenter and therefore are strongly dependent on the FOV size used [63, 64]; in particular, acquisition for radiotherapy purposes, which requires a large FOV, are more sensitive to this aspect [65].

Geometric distortions can be reduced by using magnetic field shimming [66, 67]. MR scanner are equipped with passive and active shimming. Passive shimming method concerns the use of ferromagnetic materials, typically iron or steel, placed in a regular pattern at specific locations along the inner bore of the magnet. In reverse, active shimming uses dedicated coils with adjustable current. It is patient specific, since an algorithm, implemented in the MRI system, calculates in a completely automatic way (in the seconds just before the scan) the optimal shim currents that generate an extra corrective magnetic field to better improve the homogeneity in the FOV. A high acquisition bandwidth (BW) can be used to reduce the distortions due to susceptibility effects too. However, an increased BW could lead to a reduced signal-to-noise ratio, therefore an appropriate balance is necessary [68].

However, the geometric distortions in the absence of the patient are evaluated in literature. To quantify the geometric distortions several phantoms are presented in different papers; some of them are commercial, as the one provided by Spectronic Medical AB™ (Helsingborg, Sweden) or Philips (Amsterdam, The Netherlands) [46, 65, 69, 70], while others are homemade or adapted from phantoms available for different purposes [71-75]. Anyhow, all of them have in common the characteristic of having a grid inside them, usually made of plastic material, with several hundred equally spaced markers, in the all three spatial directions in order to quantify the difference between the theoretical distance between successive points and the measured one.

1.2.2. CONTOUR DELINEATION AND SCT GENERATION

Once the MR images have been acquired, the crucial task is the target and OARs definition, and in particular the sCT generation. There are plenty of methods for generating the sCT, such as bulk, voxel-based, atlas-based or hybrid ones. Important considerations in choosing the method to use concern the time required and the amount of manual work, as well as the dose calculation accuracy compared to classical CT and the clinical availability of the selected method.

One of the principal drawbacks in the choice of the method is the manual delineation of structures, which increases the variability in contour extensions, and it is time consuming, making this process not optimal in a clinical workflow [6, 28-37].

A rapid increase in the number of published sCT methods has been observed in recent years [39, 74-83]. The generation methods can be classified into different approaches: bulk, voxel-based, atlas-based, hybrid, deep learning-based [39, 78, 79].

In the first and basic method, introduced more than twenty years ago, a bulk ED value, equivalent to water, is assigned within the entire body contour [86, 87]. There is no need for any contouring, but uncertainties up to 3% are introduced in the prostate region.

A development of this method concerns the introduction of one or more structures segmentation (e.g. air or bone) to which appropriate relative ED values are assigned, thereby reducing the dosimetric uncertainties to 2% [45, 88, 89]. The ED values assignment is based on generic values provided by ICRU report n. 46 [88] or by other different method proposed in the literature [45, 88, 89]. However, structures delineation is manually performed, making this approach time-consuming and, therefore, not practical for clinical use.

The voxel-based approach [54, 91, 92, 93] relies on the information about voxel intensities to assign ED; limited information about voxel location is included. The method is mainly based on the machine learning concept, in which a subset of the available data is used to train a model, which is then applied to the remaining part to create the sCT; standard image processing can be also applied. Different advantages can be found using this method: accurate image registration is not necessary [47, 78], manual contouring is not required if statistical methods are used and patient with atypical anatomy are handled better than with other methods. One of the main drawbacks of this method is the need to have a large number of patients to train the model [81]; otherwise, the robustness of the method can be hindered.

The atlas-based method relies on the deformable registration of the MR images composing the atlas to the patient MR ones [88, 94, 95]. The atlas can either contain a single or average patient (template) or can be composed of multiple patients (multi-atlas). Known correlations between the MRI voxels and the values of interest, such as CT number or organ label are present in the atlas; once the alignment has taken place, the CT number, retrieved from the atlas, is assigned to the patients' MRI converting it into sCT. The use of an atlas enables automatic delineation of structures, which further optimizes the workflow, reducing the amount of manual work and time, and reduce inter-observer variability. This method typically uses a single MRI sequence; this ensures the scan time is kept to a minimum, reducing the patients' movement. Nevertheless, sCT generation is based on an accurate registration, in contrast to purely voxel-based method.

Furthermore, both methods rely upon a direct database which can be troublesome for patients with different anatomies from those present in the training data [81].

From the last two derive hybrid methods, which exploit the characteristics of both and are used especially in commercial solutions [84, 96].

In recent years, methods based on deep learning have been developed [81, 82, 97, 98]. They usually consist of convolutional neural networks, as generative adversarial networks. In these approaches the network is trained to learn the relationship between CT and MR images: the input is the MRI and the output is the sCT. After a proper training, sCT generation is very fast and suitable to be used for adaptive purposes, as in the MRI-linac [99].

The choice of the method to generate the sCT is fundamental in the workflow development. Two possible solutions are available: a homemade way, developed internally in the hospital, or commercial solutions, which are more expensive but at the same time make the implementation process more straight forward. Among them, the two main ones are MRCAT from Philips [85, 100],

which is MR-vendor dependent and belongs to voxel-based method, and MriPlanner from Spectronic Medical [84], which is MR-vendor independent and exploits a hybrid method.

1.2.3. DOSIMETRIC EVALUATION OF TREATMENT PLANNING

Once sCT has been generated, the obtained images are completely compliant with the TPS, allowing the dose calculation and consequently the creation of the treatment plan. It is mandatory the validation of those treatment plans from a dosimetric point of view, even if in the literature there is a lack of standardization about it [11, 23]. The validation criteria are based on both Dose Volume Histogram (DVH) parameters and 2D γ-analysis, as used in clinical routine [101]. The first one takes into account DVH parameters, regarding targets and OARs: PTV mean dose, PTV dose near to maximum/minimum, mean dose and some constraints of most important OARs are common examples. The γ-analysis is performed with different acceptance criteria (3%/3mm, as suggested by [102], 2%/2mm, 2%/1mm or 1%/1mm used in [12, 14, 22]), different dose cut off (10%, as suggested by [102], or 15%) and different passing rate, depending on different centers.

1.2.4. PATIENT SETUP VERIFICATION

The workflow ends with creation of reference images for patient setup verification prior to treatment delivery. There are few works reported in the literature dealing with this subject compared to the number of published studies on the MRI-only topic; CBCT images [85, 103, 104] or planar images [4, 103] are used depending on the strategy chosen. A large part of the studies is performed manually, through visual evaluations by different radiation oncologists in different fractions; in this way the inter and intra observer variability is tested. In many cases, prostate fiducial markers are also used to help match CBCT or planar images to reference images [83]. Anyway, the handling of this task varies greatly from center to center and there are no guidelines in this case either.

1.3. AIM OF THE THESIS

This thesis is a continuation of a preliminary study in which the possibility of implementing an MRI-only workflow for prostate cancer was evaluated and initially planned in our hospital [105, 106]. This consists in replacing CT with MRI in all steps of the radiotherapy treatment of prostate cancer, from simulation to planning and patient repositioning.

The aim of the present work is the clinical implementation of a radiotherapy workflow that leads to a move towards routinely clinic planning using MRI alone, initially considering the prostate cancer. To do this, the various resources present in a big general-purpose hospital, as Niguarda is, were used.

The available resources in Niguarda hospital were used in this work: a 1.5 T MRI-scanner (Magnetom Aera, Siemens Healthcare, Erlangen, Germany) and a standard linac (Synergy-S, Elekta AB, Stockholm, Sweden) were exploited.

The MRI-only workflow consisted of several steps, from a proper acquisition protocol, with optimized MRI sequence, dedicated flat table, immobilization devices, laser systems and markers, passing throughout the generation of an atlas in order to auto contouring the patient images and

leading to the creation of a sCT, with which the TPS can calculate the dose distribution and concluding with patient repositioning before each RT fraction.
The laser system was checked, and the MR markers were tested to correctly position the patient inside the scanner during MRI acquisition. Then, MR atlases of 20 patients, previously subjected to radiological examinations for diagnostic purposes, were implemented in order to lead to an auto-contouring of new MR images acquired, and allowing in this way the creation of sCT, after a correct assignment of the bulk EDs, taken from 20 patients that previously underwent prostate RT, for each of the 12 detected structures. The advantage is to reduce intra- and inter-observer variability and to get, in a few minutes, the contours of the main OARs saving clinician time.
Therefore, the generated sCT were dosimetrically validated; initially, a comparison between CT images and the same ones with bulk EDs for each structure was performed on 20 other patients who underwent prostate RT during the last year. As a second step, for 7 patients, whose images were acquired both with CT and MR scanner, treatment plans were compared in terms of dose distributions, considering DVH parameters and γ-analysis.
Finally, the patient setup verification prior to treatment delivery was performed by the CBCT images; the matching between these images and MRI reference ones, be they CT or MR, was performed and the two modalities resulting shifts were compared.

MATERIALS AND METHODS

2.1. MRI-ONLY WORKFLOW

The clinical implementation workflow of prostate cancer radiotherapy developed in this thesis consists of different steps, as illustrated in Fig. 2. It includes:

- MR Imaging: choice of suitable MR sequence – selection of appropriate markers and control of laser system for patient positioning in the scanner – checking of geometric accuracy of obtained images.
- Contour delineation: implementation of an auto-contouring method.
- sCT generation: creation of images to be used in the TPS for dose calculation.
- Dosimetric evaluation: validation of the treatment planning dose distributions calculated on sCT in comparison with ones obtained by the classical CT.
- Patient setup evaluation: comparison between the match of the daily CBCT with MR or CT reference images.

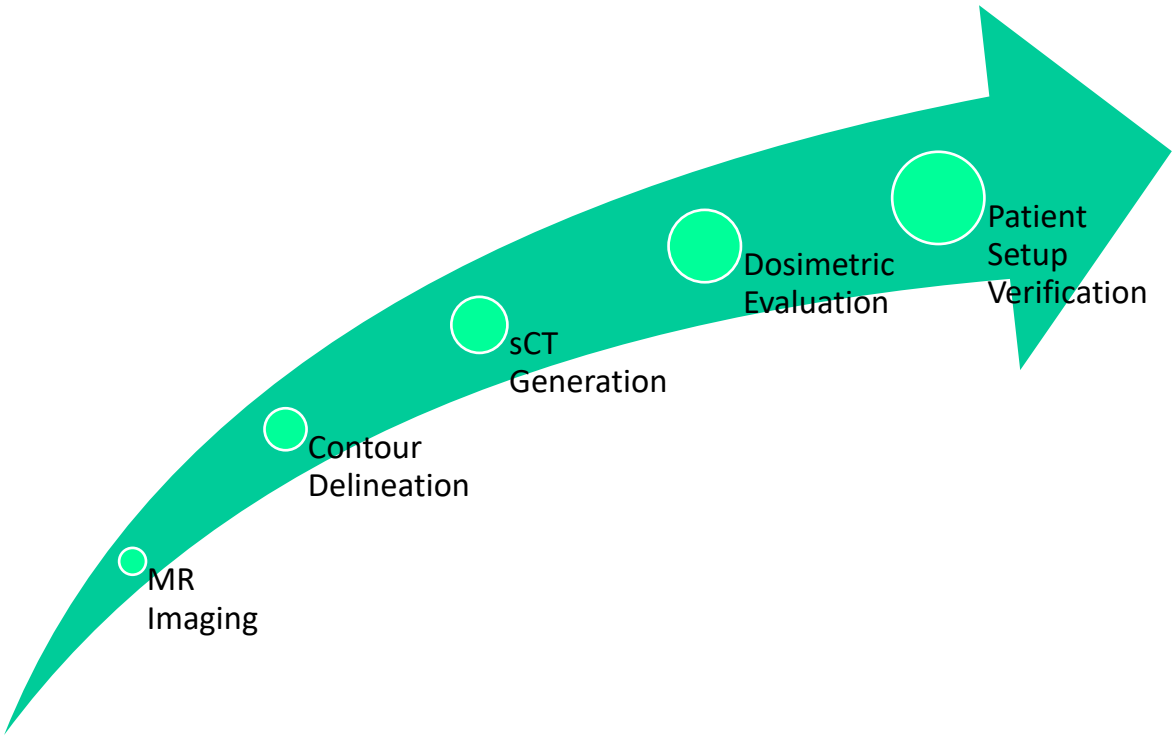

Fig. 2: MRI-only clinical workflow.

The resources present in a big general hospital as Niguarda, were used in this work: in particular, a 1.5 T MRI-scanner (Magnetom Aera, Siemens Healthcare, Erlangen, Germany) and a standard linac (Synergy-S, Elekta AB, Stockholm, Sweden) were exploited.

Several aspects of the implementation have been examined in this thesis, as reported below, in order to validate the overall workflow. Some other tasks were evaluated in a preliminary work and are reported here for completeness [105, 106].

2.2. MR IMAGING

A 70 cm wide-bore Magnetom Aera 1.5 T scanner (Siemens Healthcare, Erlangen, Germany) was utilized in this thesis.

The first phase of this work is composed of different aspects: the choice of the most suitable MR sequence, the patient positioning in the scanner, with suitable markers, laser system and the relative immobilization devices, the checking of geometric accuracy of obtained MR images.

2.2.1. MR SEQUENCE

The sequence chosen for our purposes belongs to the Dixon family; the first ones were developed in 1984 and have been evolving since then [50, 57, 58]. They have the advantage of separating fat and water. To do this, the offset between the resonant frequencies of the protons in the fat and in the water, approximately every 2.4 ms at 1.5 T, is exploited; this phenomenon is known as chemical shift.

The basic principle behind these techniques is to encode the signal periodically at the fixed offset between protons of fat and water during the acquisition, and subsequently estimate the contribution of water and fat protons to the measured signal during postprocessing.

One of the most common Dixon techniques is the two-echo acquisition (or two-point) and is schematically described below and illustrated in Fig. 3. A first acquisition is performed with an echo time (TE) with fat and water protons in phase; afterwards, a further acquisition is performed with an appropriate TE with fat and water protons out of phase (corresponding to a difference of 2.4 ms at 1.5 T). Then, adding the two acquisitions, images showing water contribute are obtained (with suppression of fat signal); on the other hand, subtracting of the out-of-phase from the in-phase acquisitions results in images showing fat contribution (with suppression of water signal). Thus, four sets of images are postprocessed and automatically reconstructed, as shown in Fig. 4.

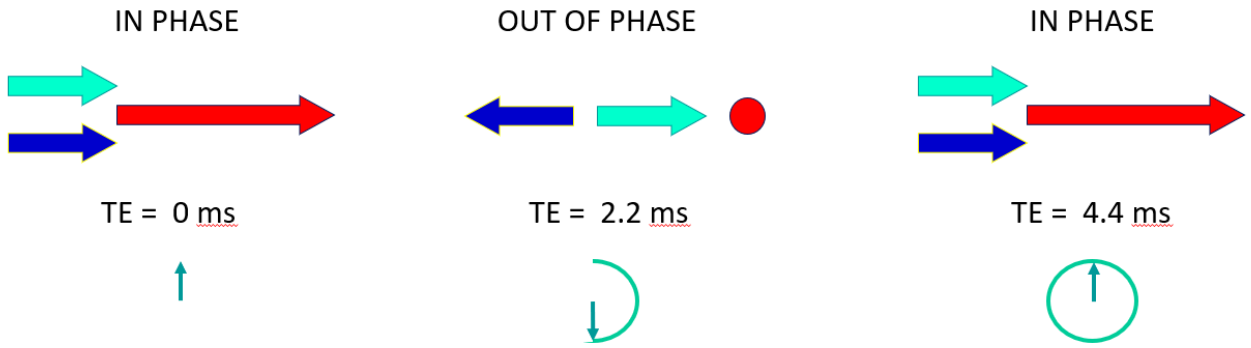

Fig. 3: Two-echo Dixon sequence: in green the magnetization direction of water, in blue that of the fat. At TE = 0 ms water and fat have the same direction, thus creating a strong signal. At TE = 2.2 ms (at 1.5 T) they have opposite directions and so create no signal. Once the TE = 4.4 ms, fat and water add up again.

In the in-phase images, bones are better defined; on the contrary, with out-of-phase images edges of bladder, rectum, prostate and seminal vesicles are more clearly visible. The remaining images, fat and water, allow the clinician to evaluate other aspects in more detail.

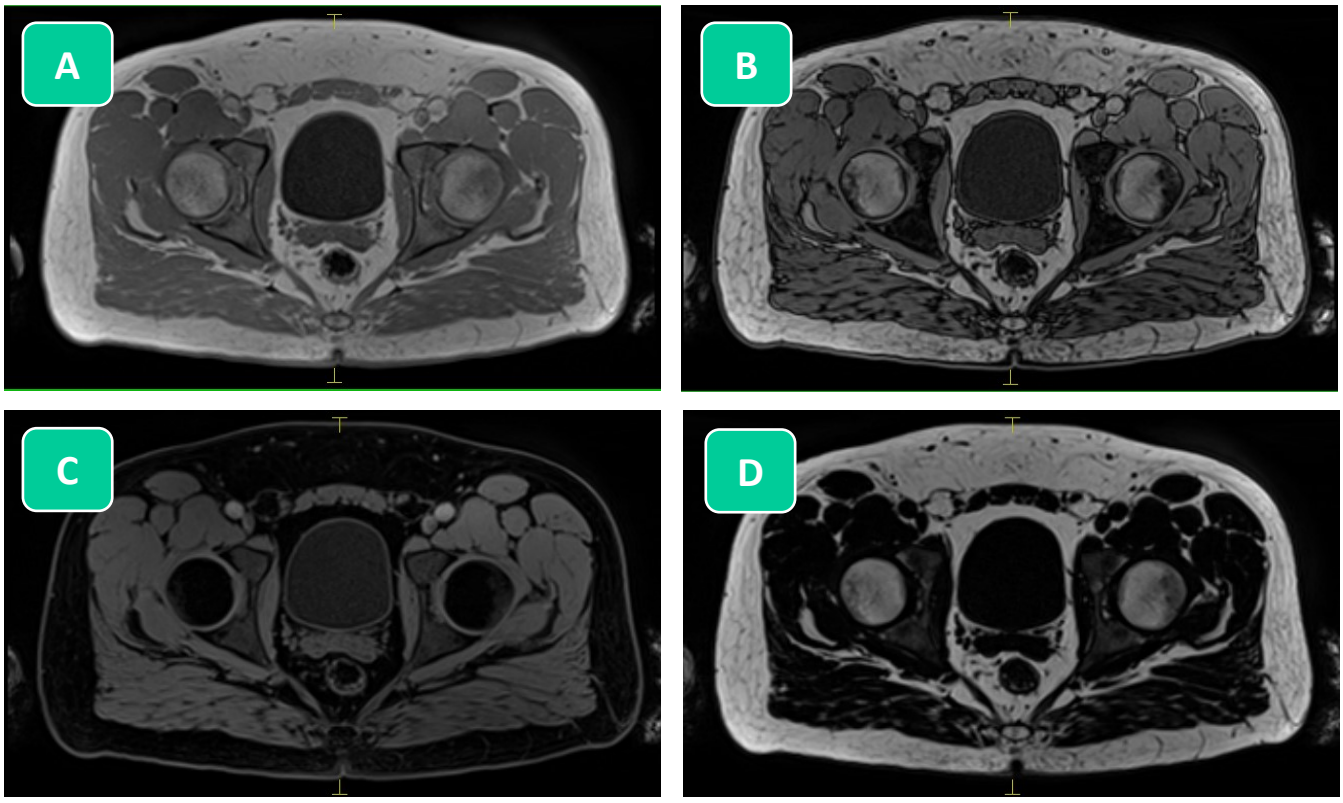

Fig. 4: 3D T1-VIBE-Dixon sequence used in this work. Left to right, top to bottom: in-phase (A), out-of-phase (B), water (C) and fat (D) images.

The Dixon techniques have the advantage of providing four contrasts, with an high signal to noise ratio, in one single acquisition and in a reasonable time, can be weighted towards T1 or T2 and can be implemented in both gradient-echo (GE) and spin-echo (SE) sequences.

The Dixon sequences in the Magnetom Aera 1.5 T scanner (Siemens Healthcare, Erlangen, Germany) were suitably optimized in the previous thesis in order to reach a good compromise between image quality and acquisition time. The images used in this work were acquired using a Cartesian T1-weighted 3D Volumetric Interpolated Breath-hold Examination (VIBE) Dixon sequence.
The sequence is a spoiled gradient-echo acquisition that uses a gradient at the end of the repetition and additionally varies the phase of each RF pulse to eliminate transverse magnetization, providing pure T1 contrast. In a simplified way, a diagram of the sequence is shown in Fig. 5.
The acquisition parameters are reported in Table 2. The field of view was set to cover the whole outer body contour for RT purpose.
In addition, all examinations were conducted using partial parallel acquisitions imaging GRAPPA (acceleration factor = 2) with 18-channel body RF coils.

Parameter	Value
Repetition Time (TR)	7.0 ms
Echo Time 1 (TE_1)	2.39 ms
Echo Time 2 (TE_2)	4.77 ms
Flip Angle (FA)	10°
Isotropic Voxel Size	~ 1 mm^3
Bandwidth (BW)	445 Hz/pixel
Number of Slices	176
Scan Time	2 min and 30 sec

Tab. 2: The optimized acquisition parameters of *3D T1-VIBE-Dixon sequence used in this work.*

Since the acquisitions were performed during free breathing, which could lead to ghost artefacts related to respiratory movement, especially if the phase encoding direction is anterior-posterior (AP), the phase encoding was changed to right-left direction (RL), with a 90% oversampling phase.

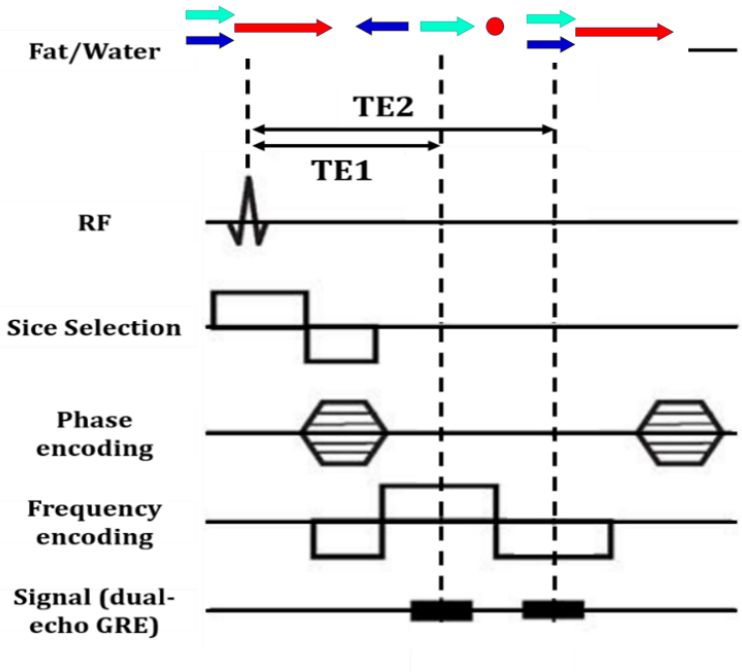

Fig. 5: Dual gradient-echo sequence with Dixon technique: in green the magnetization direction of water, in blue that of the fat. After the initial excitation, two gradient echoes at different echo times (TEs) are acquired in two-point Dixon, the magnetizations of fat and water would be opposed-phase in one echo (TE_1) and in-phase in another echo (TE_2). The water-only and fat-only images can be generated from the combination of in-phase and opposed-phase data sets.

2.2.2. ACQUISITION SETUP

Patients positioning within the scanner is of paramount importance to ensure reproducible daily setup. To achieve this, a flat table-top and feet and knee supports are basic for prostate radiotherapy [60, 61].

Actually, the typical MRI couch is not flat as the one of the standard CT and linac, because it is designed to ensure comfort for the patient undergoing diagnostic purpose. To reproduce the same setup as during irradiation at linac, an 8 mm wooden bi-laminated rigid flat table was manufactured by carpenters at the Niguarda hospital, as shown in Fig. 6. It is light, weighting less than 6 Kg, and easy to handle. The table, 50 cm in width and 134.5 cm in length, was designed to avoid unbalanced effects in the patient positioning and enable the insertion of the abdomen receiver coil.

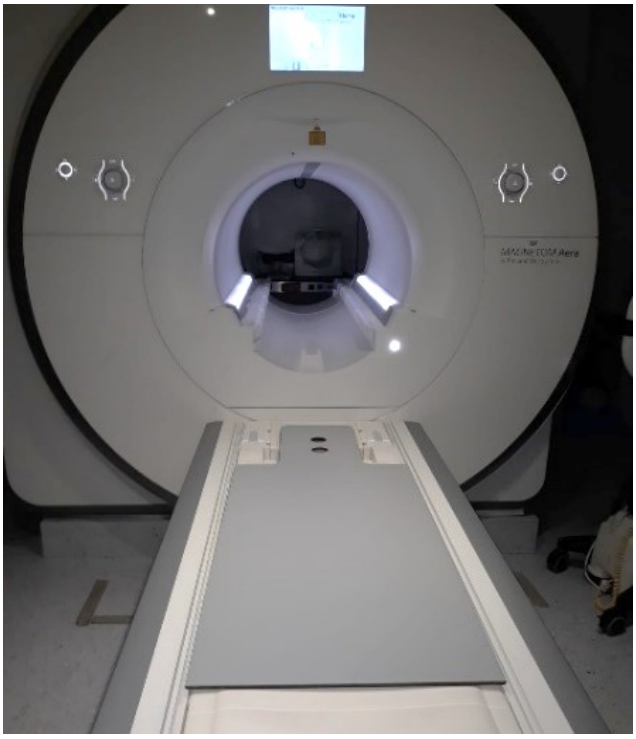

Fig. 6: Magnetom Aera 1.5 T MR (Siemens Healthcare, Erlangen, Germany) scanner with the 8 mm wooden bi-laminate rigid flat table.

Patients were positioned in the MR scanner just like in the CT scanner, with feet fixation and with knee support, and with 18-channel body RF coils, as visible in Fig. 7. Furthermore, their training and physical condition are essential for a reproducibility purpose; they had no dietary restriction prior to the session but were asked to drink 0.5 l of water, half an hour before the imaging acquisition to have a filled bladder.

Fig. 7: Patient positioned on the 8 mm wooden bi-laminate rigid flat table, with fixation devices and 18-channel body RF coils, ready for MRI acquisition.

In addition to the aspects developed in the previous thesis, laser system and fiducial markers were also considered in this work.

A calibrated laser system is essential for correct patient positioning in the scanner before acquisition. Normally, an external laser system is installed in the CT room; as the feasibility of implementing the MRI-only workflow was considered in this work, an MR safe external laser system has not yet been purchased. It was therefore decided to use the internal laser system of the MRI scanner. It is formed by a cross projected from a single point inside the scanner, located on the upper side; although the isocenter, detected by the laser system, can be correctly identified, a small rotation in the projected cross is sufficient to cause a shift of several millimeters at a distance of 20 cm from the center.

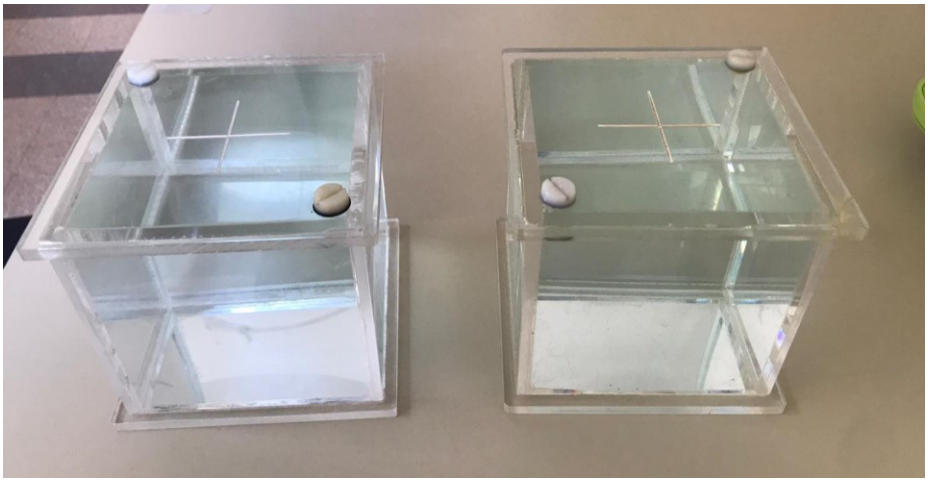

Fig. 8: Couple of cubic phantoms of 10 cm side, used to check the MR internal laser system. A cross on the upper side, used to position them in the correct position, can be noticed.

Apart from the quality controls performed by Siemens twice a year, further measurements to check and validate the clinical use of the internal laser also per positioning purposes in RT workflow, were carried out. To do so, dedicated phantoms were used, as displayed in Fig. 8. They are a couple of cubic plastic phantoms, with side of 10 cm, filled with a solution of nickel chloride and sodium chloride to provide contrast in MR acquisitions; on their upper side there is a cross that allows to center them in the MR scanner.

To verify that the laser cross was not tilted, the phantoms were positioned on the rigid flat table, with the body RF coils above them, as reported in Fig. 9. The quality assurance process consisted of three different measurements with the 3D-T1-VIBE Dixon sequence:

- One of the cubes was positioned at the isocenter, based exclusively on the correspondence of the laser system cross with that on the upper face of the phantom. The other cube was placed on its right at 15 cm distance (from center to center). Each phantom was positioned independently, based solely on the laser cross.
- The previous measurement was repeated by placing one of the two cubes to the left of the central one.
- Finally, the two phantoms were placed at 5 cm from the table edges, to obtain a distance from the two cubic of 28 cm (center to center), to test all the typical acquisition FOV.

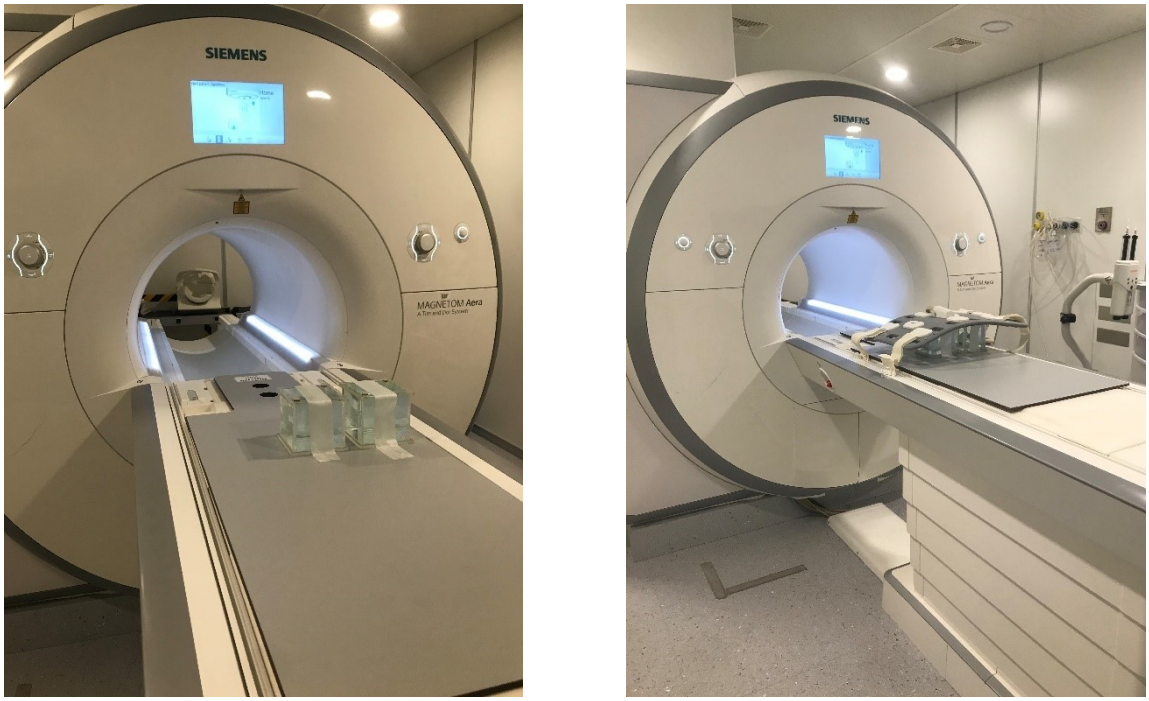

Fig. 9: Example of measurement configuration with the two cubic phantoms used for internal laser check

Once the images were acquired, a straight line from the middle of the central phantom, corresponding to the center of the MR image, was drawn to the other cube, with Image J software. Furthermore, the difference (in distance and in angle) between the center of the lateral phantom and the theoretical one, indicated by the line, was measured. Moreover, the same calculation was

performed for the furthest phantom edge. The process is shown in Fig. 10. The acceptance criterion adopted for this measurement is 2 mm, as occurs for external lasers in CT simulation [107].

These measurements were repeated 2 months apart to assess repeatability and any drift.

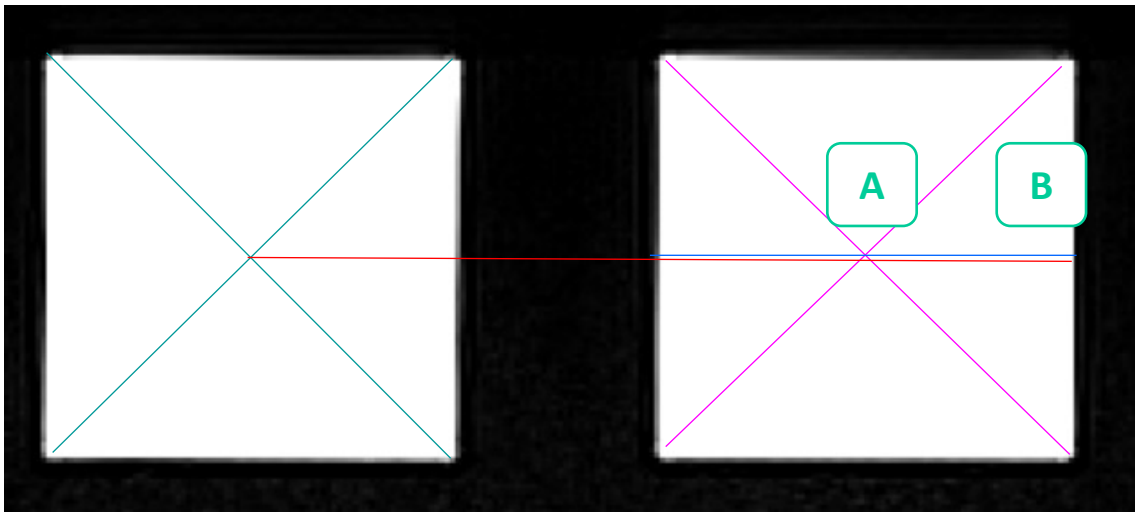

Fig. 10: Example of laser system tilt measurement. On the left the phantom placed at the isocenter, on the right the other one positioned at 15 cm distance (center to center). The red line passes through the isocenter, while the blue line crosses the center of the lateral phantom. This way the laser system tilt is measured both in the center of the lateral cubic phantom (A) and at its further edge (B).

In the patient positioning procedure, lasers are usually positioned on tattoos made on the patient's skin; markers are therefore necessary to identify the position of the tattoos in the imaging acquisition. In particular, the ones used in planning CT acquisitions could not be used in the MR room. Different options are tried, from home made to commercial solutions; finally, the LiquiMark™ MRI Markers (Suremark® - Simi Valley, California, USA) were chosen, since provided the better contrast in our MR images. In the Fig. 11 these non-metallic spheres of 8 mm diameter, filled with specific gel, are presented.

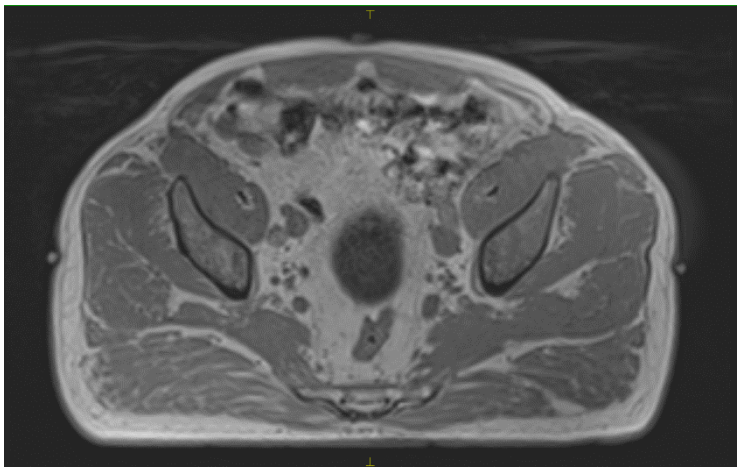

Fig. 11: LiquiMark™ MRI Markers.

2.2.3. GEOMETRIC DISTORTIONS

High geometry accuracy is mandatory for MR images used for RT purposes. Nevertheless, imperfections in the static magnetic field uniformity, eddy current and gradient linearity may lead to geometric distortion, which are typically divided into two main categories: system or scanner related distortions, caused by inhomogeneities in the main magnetic field and gradient nonlinearities, and patient-induced distortions due mainly to magnetic susceptibility variations at the interface of different tissues [24]. In particular, tissue magnetic susceptibility-induced effects are patient-dependent, and their behavior is difficult to assess and predict.

These distortions increase in magnitude with the radial distance from the isocenter and therefore are strongly dependent on the FOV size used [63, 64]; in specific, acquisition for radiotherapy purposes, which requires a large FOV, are more sensitive to this aspect [65].

Besides, geometric distortions can be reduced by using magnetic field shimming [66, 67]. MR scanner are equipped with passive and active shimming. Passive shimming method concerns the use of ferromagnetic materials, typically iron or steel, placed in a regular pattern at specific locations along the inner bore of the magnet. Contrariwise, active shimming uses dedicated coils with adjustable current. It is patient specific, since an algorithm, implemented in the MRI system, calculate automatically (in the seconds just before the scan) the optimal shim currents that generate an extra corrective magnetic field to better improve the homogeneity in the FOV.

Moreover, our MRI scanner systems features TrueForm™ Magnet Design (Siemens Healthcare, Erlangen, Germany). It is optimized for a cylindrical shape of the homogeneous volume of the magnetic field, rather than the typical spherical or ellipsoid volume. The benefit of TrueForm™ Magnet Design is a better depiction of the edges of the 3D FOV. This is particularly beneficial for large FOV coronal imaging as abdomen-pelvis. A representation of TrueForm™ Magnet Design is shown in Fig. 12.

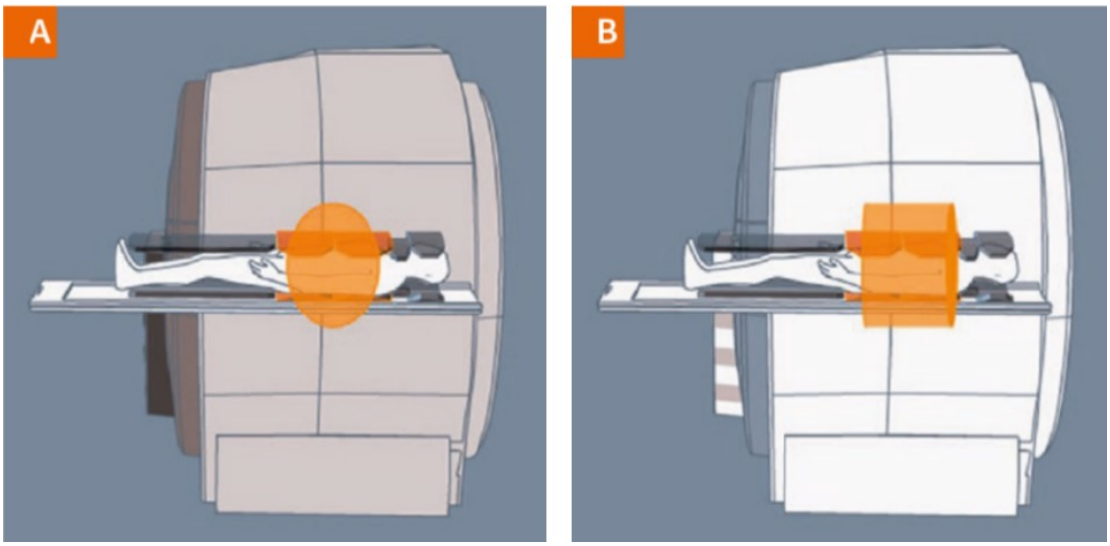

Fig. 12: Scheme of the imaging volumes of a conventional magnet with spherical/ellipsoid volume (A) vs TrueForm Magnet Design with a cylindrical volume (B). The figure is taken from Blasche et al. 2017.

A high acquisition bandwidth can reduce the geometric distortion too [68]: for this purpose, in the optimized sequence, the chosen bandwidth (BW) is equal to 445 Hz/pixel.

Although phantom studies experiments are unlikely to reflect the full complexity of the clinical case, including differences in patient setup and internal movements between acquisitions, the system-related and patient-induced geometric distortions can be measured and quantified.
Regarding this topic we discussed with the manufacturer, who explained to us that the active shimming present on the scanner corrects the distortions in each acquisition in a suitable way. Moreover, periodic QA controls in the MR scanner are performed every three months with ACR phantom to check the stability of the scanner performances [108, 109].
However, the geometric distortions in the absence of the patient were evaluated in the previous thesis work, by a cylindrical MRI Leksell phantom (Elekta AB, Stockholm, Sweden) as reported in Fig. 13.
It is made of acrylic plastic and was 180.5 mm in diameter and 131 mm in height. In this volume, there are 190 marker points of 2 mm in diameter and 2.5 mm in height respectively, placed in a 3D-grid, made of plastic material. In this way it is possible to evaluate the geometric distortion by quantifying the difference between the theoretical distance between successive points and the measured one in the all directions.

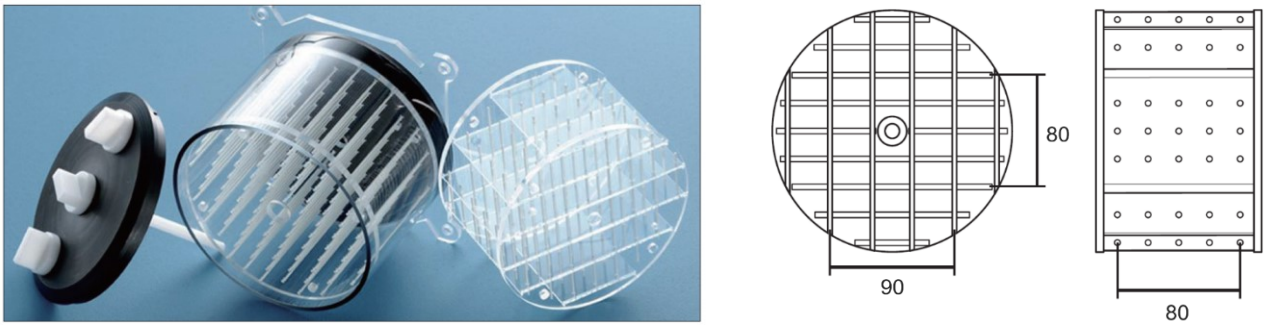

Fig. 13: the Elekta (Elekta AB, Stockholm, Sweden) magnetic resonance imaging phantom. On the right, the scheme of the grid in all directions.

In order to investigate the geometric distortions in the different positions of the FOV with a phantom of such a small size, a rigid indexed support fixed to the flat table was used. The phantom was acquired at the isocenter, in two lateral positions at 15 cm (center to center) from the starting position and at 12.5 cm cranially from isocenter. The measurements setup is displayed in Fig. 14.
All the MR images were scanned with the same FOV of 45 cm centered at the isocenter and with the same optimized sequence reported below.
For more details on how the distance measurements were performed, I refer you to the previous thesis work [105].

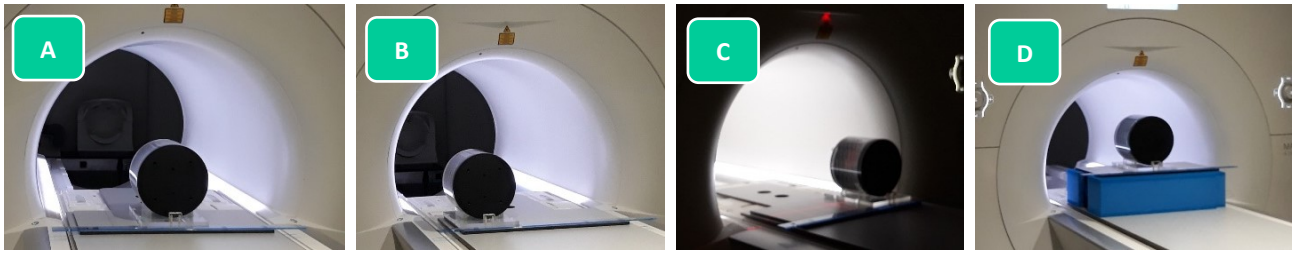

Fig. 14: Phantom position on flat table-top on MRI scanner. From left to right. Isocenter (A), 15 cm right (B), 15 cm left (C) and 12.5 cm cranially from isocenter (D).

2.3. CONTOUR DELINEATION AND sCT GENERATION

Once the MR images have been acquired, the next task is to define the volumes of both target/s and OARs directly on them. Actually, in addition to the OARs usually identified on CT images, due to the demands of dose constraints used in our hospital [110], further structures need to be contoured because of the sCT generation method chosen. Indeed, in this thesis a hybrid method is proposed: it is a combination of bulk and atlas-based approach. This consists of creating atlases of MRI images from healthy volunteers and patients, who underwent to MRI for diagnostic purposes, with a corresponding set of organ labels and assign them average EDs. The 12 structures identified in the images are: Bladder, External, Femurs, Femoral Heads, Pelvic Bones, Prostate, Rectum, Sacrum and Seminal Vesicles.

Patient / Volunteer	Age (Years)	Weight (Kg)	Height (cm)	BMI
V	29	80	184	23.6
V	28	85	175	27.8
V	56	96	178	30.3
V	56	80	180	24.7
V	66	70	174	23.1
V	27	100	185	29.2
V	64	100	190	27.7
V	58	76	172	25.7
V	55	65	180	20.1
V	32	75	170	26.0
V	25	65	175	21.2
V	29	60	160	23.4
V	28	70	170	24.2
V	40	70	180	21.6
P	63	94	170	32.5
P	65	75	170	26.0
P	65	87	178	27.5
P	76	79	178	24.9
P	64	80	170	27.7
P	75	60	160	23.4
Mean	**50**	**78**	**175**	**25.5**
Range	29 - 64	70 - 86	170 - 180	23.4 - 27.7

Tab. 3: List of patients used to form the atlases. Age, weight, height and Body Mass Index (BMI) are reported. In the last two rows Mean values and Range (25th percentile – 75th percentile) are highlighted.

In this thesis work 20 pelvic MRI images from healthy volunteers and patients are used as atlases, as schematically reported in Table 3.

The four contrasts MRI Dixon images (in-phase, out-of-phase, water, fat) of the 20 men were uploaded into the Monaco® treatment planning software (version n. 5.51, Elekta AB, Stockholm, Sweden) and the structures were manually contoured with extreme precision for all the 176 slices, taking advantage of the different contrasts provided by the Dixon sequence. The contouring was done by the medical physicist and subsequently corrected and validated by the supervisors, a team of physicists, radiologists and radiation oncologists. The in-phase images were preferred to contour the bones, while out-of-phase to delineate the soft tissues, as bladder, rectum, prostate and seminal vesicles. The remaining images, fat and water, allow the clinician to evaluate eventually further details on the prostate. One of the advantages of using Dixon sequences, is the possibility to switch from one contrast to another without losing accuracy in the delineation, since they are acquired simultaneously. An example of a manually contoured images is reported in Fig. 15.

Finally, it was decided, together with the radiation oncologists, to use atlases of only one contrast: the in-phase images were selected, since they were the best compromise between the four different contrasts.

To contour a new image of a patient, the atlases are registered via Deformable Image Registration (DIR) to the subject's image to obtain a good correspondence between structurally equivalent regions in the two images, and then labels defined on the atlases are propagated to the image. For image registration and label fusion, the ADMIRE software (research version 1.13.5, Elekta AB, Stockholm, Sweden) was used.

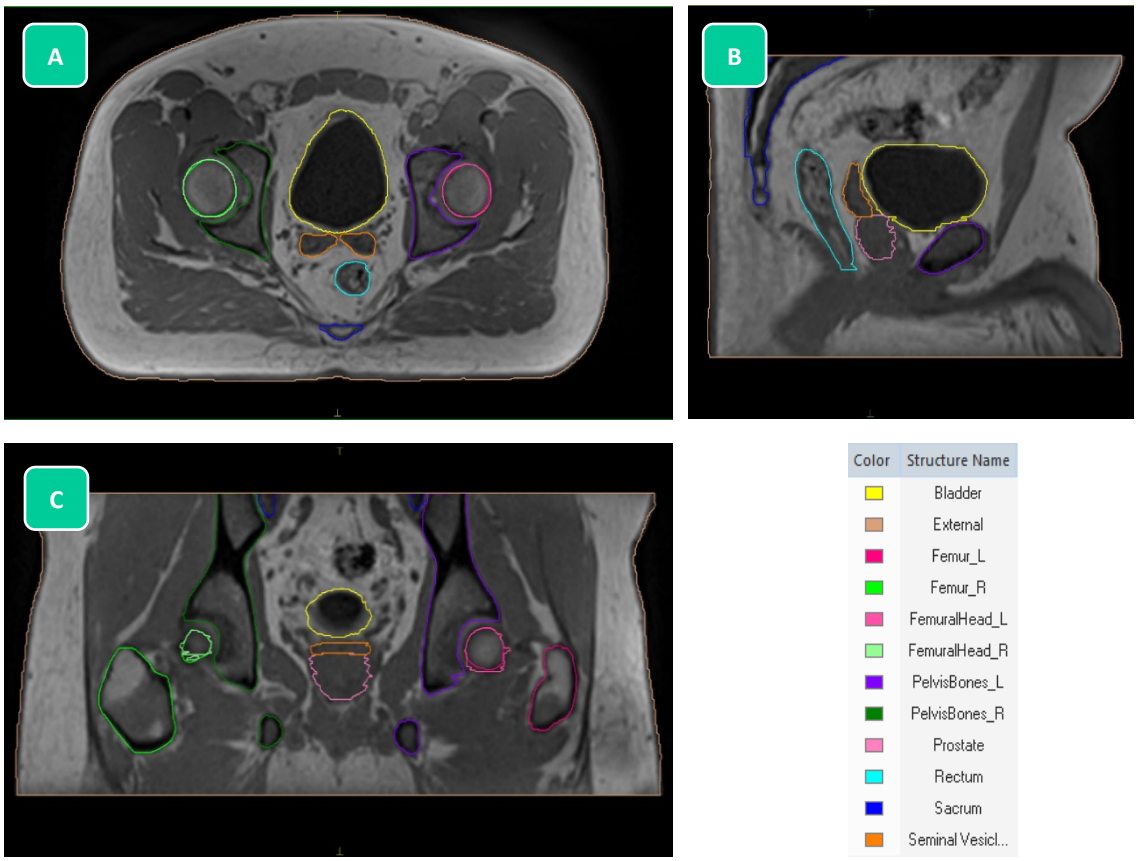

Fig. 15: Axial (A), sagittal (B) and coronal (C) views of out-of-phase 3D-T1-VIBE Dixon, manually contoured. On the bottom right corner, the considered structures are reported.

2.3.1. ADMIRE

ADMIRE (ADvanced Medical Imaging Registration Engine, research version 1.13.5, Elekta AB, Stockholm, Sweden) is a software that enables the contouring of structures on new images using knowledge that was previously labelled in a dataset (atlas); an example could be MR images manually contoured by an expert team.
To transfer atlas contours to the image data of a new patient, atlas images are firstly non-rigidly registered to the image data to the new subject image data, then with the transformation vectors, it is possible to transform the atlas contours to the new patient. The complete process is presented in Fig. 16.
The registration strategy includes the shape of structures in the atlas to help improve the registration efficiency and robustness [111].

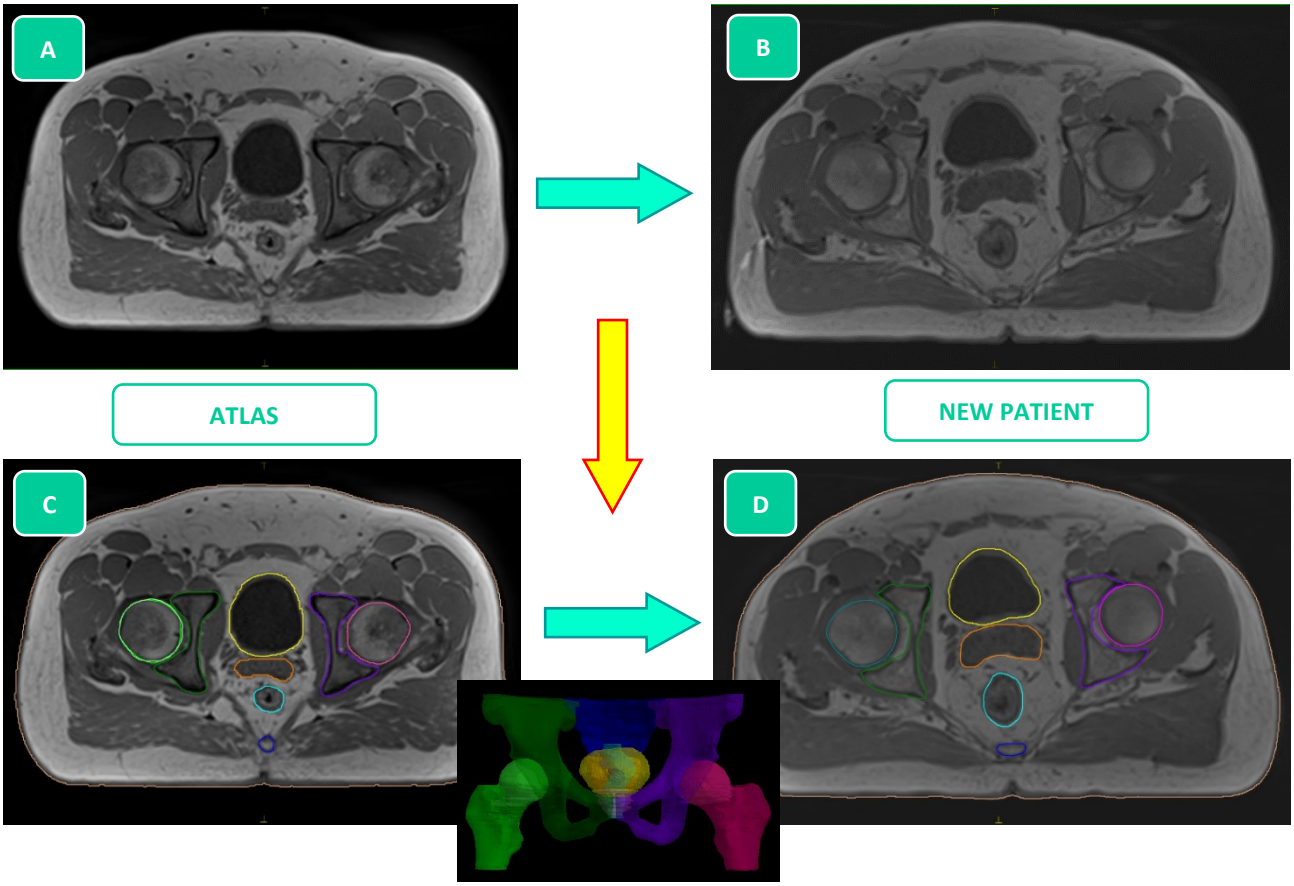

Fig. 16: Schematic representation of ADMIRE. At the begin, the image data of the atlas (A) is non-rigidly registered the new subject image data (B), then the atlas contours (C) are transformed to the new patient images (D).

Furthermore, this software uses a multi-atlas fusion strategy that usually provides a significantly improved accuracy in segmentation than using a single atlas alone, which is unable to adequately consider the differences in the anatomy of patients [112].
In the beginning, the multiple individual atlases are applied independently to get multiple contours of the same subject, which are then combined in a multi-classifier framework to get a final unique segmentation [113].
For label fusion, 2 different algorithms can be selected in ADMIRE (research version 1.13.5, Elekta AB, Stockholm, Sweden): the STAPLE label fusion [114, 115] and Patch label fusion [116]. The STAPLE

algorithm works with a statistical framework that simultaneously estimates the underlying truth segmentation and the accuracy of each individual atlas. It ignores the image data and uses only the segmentations when computing the label fusion. In contrast, the Patch algorithm considers the accuracy of the initial image registration by comparing the intensity similarity between the atlas and the patient after being aligned, to get better label fusion results. This process is called intensity weighting. With a multi atlas consisting of 20 patients the difference between the two methods is limited.

The overall framework of the ADMIRE method is summarized in Fig. 17.

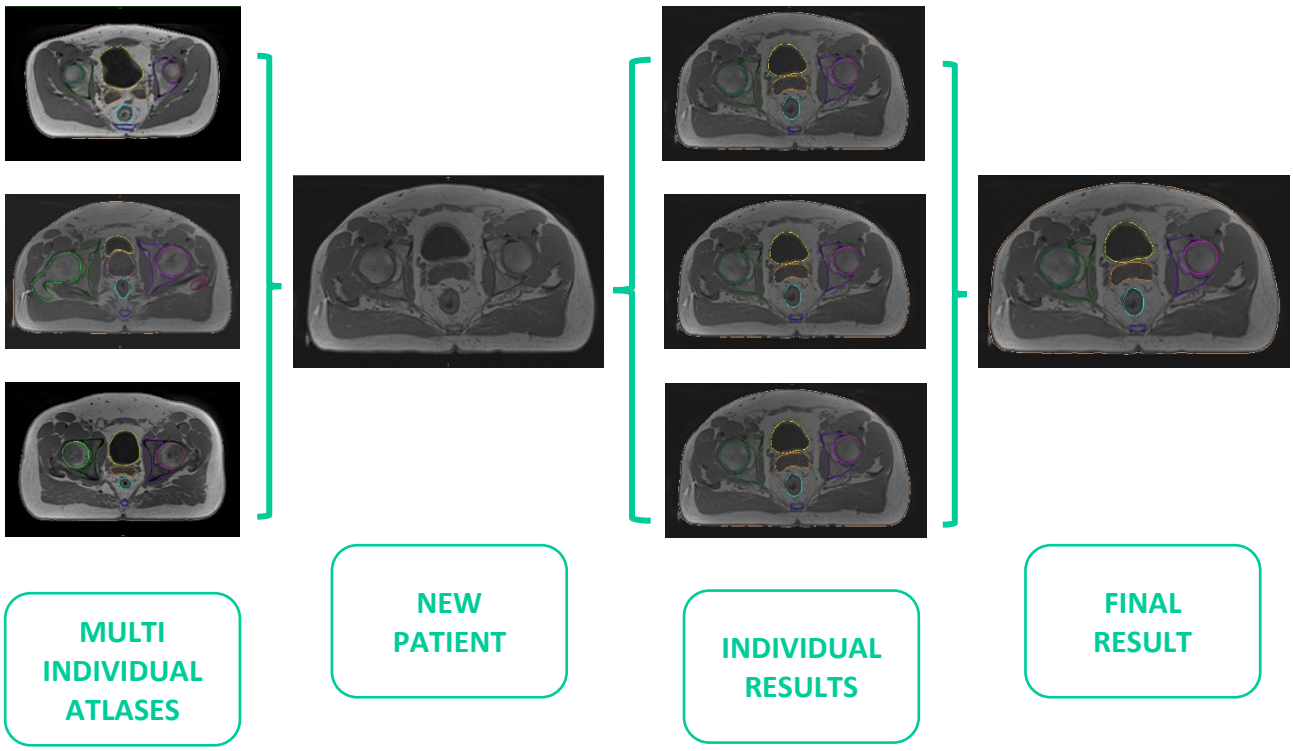

Fig. 17: Simplified scheme of ADMIRE method. First, the multiple individual atlases are applied independently to get multiple segmentations of the same subject, which are then combined in a multi-classifier framework to get a final unique segmentation.

For a better comprehension of the process, the workflow for computing the automatic contouring in prostate subjects, using a single atlas, is summarized in Fig. 18. The core algorithm is a hierarchical atlas registration method that consists of three major steps: a linear registration, an object-driven poly-smooth non-linear registration, and a dense hybrid deformable registration. These three steps gradually increase the degrees of freedom for image matching, and the result of an earlier step is used to provide initialization for the next step that follows.

The linear registration aims to correct for global differences in position, orientation, and size between an atlas and a subject image. The software uses linear registration model with 9 degrees of freedom, where the free parameters include three translation, three rotation, and three scaling factors. To find the optimal transformation parameters, it maximizes the global mutual information (MI) between the atlas and subject images using a multi-resolution stochastic gradient-descent optimization scheme with a random sampling pattern of about 100 image patches at each iteration [117].

The poly-smooth nonlinear registration is the first 3D non-linear registration step in ADMIRE software (research version 1.13.5, Elekta AB, Stockholm, Sweden). The basic idea is to reduce the degrees of freedom of the non-linear registration in order to achieve a more robust registration. The poly-affine framework, however, restricts each object to follow an affine transformation, which is insufficient to model large inter-subject shape variations. An ad-hoc solution that splits a large object into multiple smaller components was developed [118]. Instead, it is only necessary to have points belonging to the same object to deform consistently; that is, the deformation vector field should be smooth along the boundary surface of each object. Thus, this model is more flexible and can naturally handle large inter-subject shape changes.

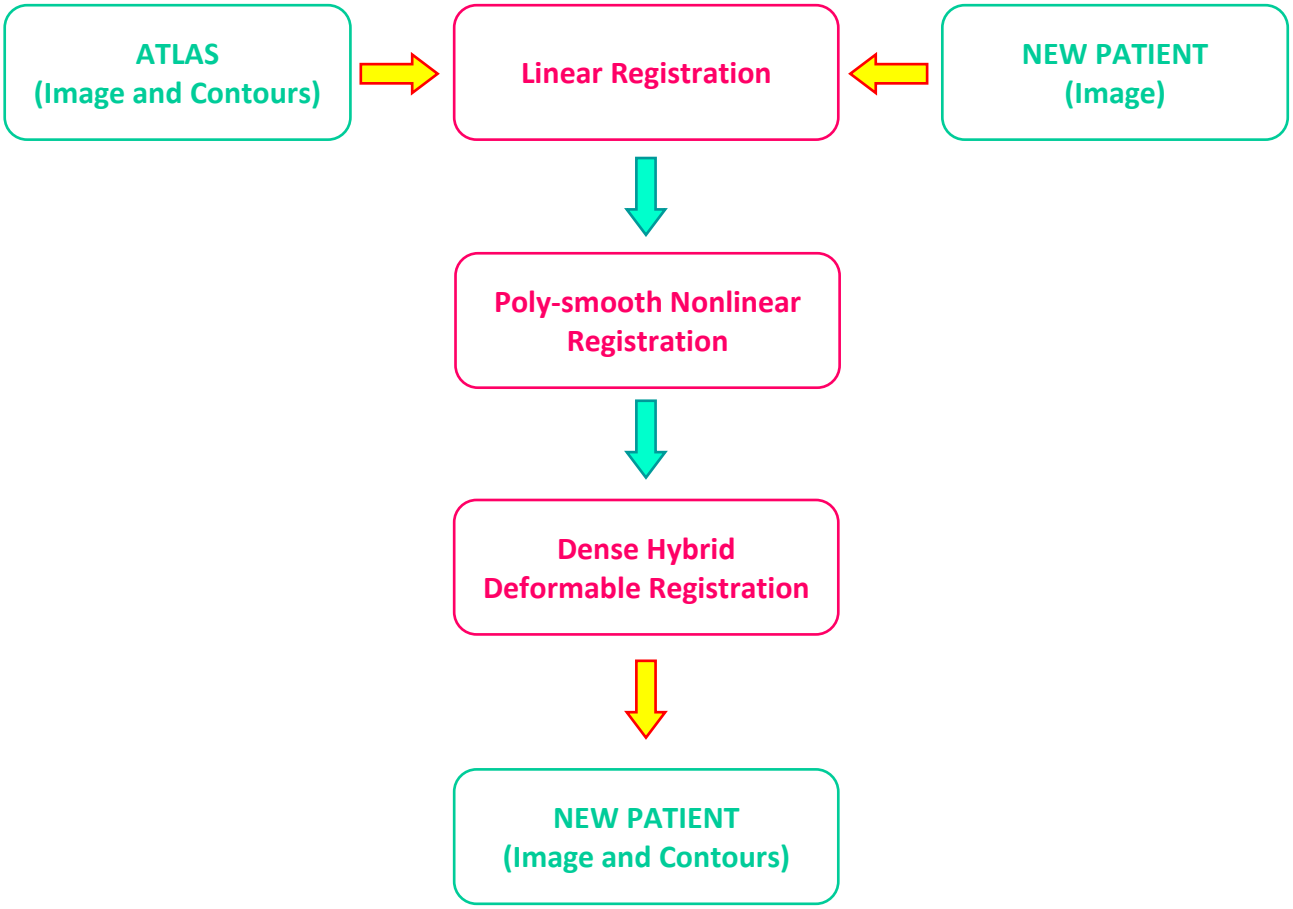

Fig. 18: Example of auto-segmentation workflow with a single atlas.

In the final phase of the atlas registration, a full free-form deformable registration is calculated to further refine the recording of results from the previous phase and to align the detailed structures of the atlas with the images of the subject.

In order to better overlap the boundaries of the object, while remaining robust to changes in image contrast, a hybrid image has been developed that matches the metrics to be used in this phase, which is a combination of the traditional mutual information (MI) and a new standardized sum-of-square-difference metric (NSSD) [119].

This hybrid similarity method provides better alignment of image edges than using the MI metric alone since the latter cannot account for local image contrast changes. On the contrary, the NSSD metric is an edge-based alignment metric and can naturally handle local image contrast changes.

However, using the NSSD metric alone is sensitive to initialization because it cannot differentiate well between neighboring edges with similar orientation. The hybrid metric combines the advantage of each term, providing more robust results.

2.3.2. Electron Densities

When the structures have been automatically contoured, it is necessary to assign an electron density to each of them. In the method proposed in this thesis, an average ED value is associated with each structure. To obtain these values, in the previous work a set of 20 patients who underwent radiotherapy for prostate cancer during last year, were selected. Their mean age was 77 years old (range 70-82 years) and their CT images were acquired on a Philips big bore Brilliance CT scanner (Philips Medical System, Amsterdam, The Netherlands), with 120 kVp and 3 mm of slice thickness. The patients were in a supine position, with knee support and fixation of the feet, exactly as described for MRI acquisition. Moreover, they had no dietary restriction prior to the session but were asked to drink 0.5 l of water, half an hour before the imaging acquisition to have a filled bladder.
For the automatic segmentation of bones and organs of interest, ADMIRE (research version 1.13.5, Elekta AB, Stockholm, Sweden) was used with its pre-set of three CT atlases (small, medium and large anatomies). For femurs, femoral heads, pelvic bones and sacrum, the automatic contouring provided excellent results while for the bladder, rectum and seminal vesicles it was worse than the one performed by the clinician for treatment planning, probably due to the small number of atlases that do not perform well for those particular anatomies.
Therefore, for femurs, femoral heads, sacrum and pelvic bones we considered the contours resulting from ADMIRE and for bladder, rectum and seminal vesicles the contours carried out by the clinician.

2.4. Dosimetric Evaluation

Once sCT has been generated, the obtained images are completely compliant with the TPS, allowing the dose calculation and consequently the creation of the treatment plan. It is mandatory the validation of those treatment plans from a dosimetric point of view, even if in the literature there is a lack of standardization about it [11, 23].
The dosimetric evaluation on sCTs consisted of two different phases. In the first one, the EDs assignment was assessed recalculating the dose distributions obtained with the CT on the same images, in which only the EDs were changed, passing from a continuous value to a fixed one. In this case, the OARs (bladder, external, femoral heads, rectum) contoured by the radiation oncologist on the CT were copied and kept on the sCT, while the remaining structures of interest (femurs, pelvis, sacrum) were manually contoured by the same radiation oncologist afterwards. Subsequently, the same process was performed on sCT, this time obtained from MR images, where structures were automatically contoured by ADMIRE (research version 1.13.5, Elekta AB, Stockholm, Sweden); in this case the combination between the assignment of an average ED and the different contours in the two imaging modalities was evaluated.
At first, 10 MV X-rays VMAT prostate treatment plans of 20 patients (see Table 4) were calculated on CT images. The prescribed dose was 72 Gy in 30 fractions (2.4 Gy per fraction). The treatment

plans were calculated with the X-rays Voxel Monte Carlo algorithm with 0.3 cm grid-size and 2% MC uncertainty per calculation in Monaco® TPS (version 5.51, Elekta AB, Stockholm, Sweden). The dose optimization process was conducted by minimizing high dose volumes in healthy tissues, especially at the OARs, such as the rectum and the bladder wall, without compromising the target coverage. In detail, the dose-volume constraints for OARs, used for conventional fractionation and followed in our hospital, derived from [110] and are reported in Table 6.

Patient	# PTV	Age
1	1	70
2	1	77
3	1	80
4	1	66
5	1	75
6	1	72
7	1	63
8	1	58
9	1	76
10	1	64
11	1	77
12	1	76
13	1	77
14	1	78
15	1	78
16	2	70
17	2	72
18	2	70
19	3	73
20	3	54
Mean		**71**
Range		69 - 77

Tab. 4: List of patients used in the first part of sCT validation. Number of PTVs and age are reported. In the last two rows Mean values and Range (25^{th} percentile – 75^{th} percentile) are highlighted.

The optimized plans were copied using the same field arrangements and recalculated on the sCTs, obtained by CT images, as described in the section 2.2.2, only replacing the ED density of each structure with the average one, previously calculated. The validation criteria used in this work are based on both Dose Volume Histogram (DVH) parameters and 2D γ-analysis [99], as detailed in the following sections (2.3.1 and 2.3.2). Dose deviations between calculations based on standard CT image and the synthetic CT were evaluated using those quantitative and efficient methods.

Therefore, the validation of sCT generated directly by MRI images was performed. For this purpose, 7 patients, eligible for MRI-only workflow, were selected during last year, as schematically reported in Table 5.

Patient	# PTV	Age (Years)	Weight (Kg)	Height (cm)	BMI
1	3	74	80	184	23.6
2	1	79	85	175	27.8
3	1	77	96	178	30.3
4	1	73	80	180	24.7
5	2	76	70	174	23.1
6	1	79	100	185	29.2
7	1	73	100	190	27.7
Mean		**76**	**77**	**173**	**25.7**
Range		73 - 78	75 - 78	170 - 178	24.4 - 27.1

Tab. 5: List of patients used in the MRI-only workflow validation. Number of PTV, age, eight, height and Body Mass Index (BMI) are reported. In the last two rows Mean values and Range (25^{th} percentile – 75^{th} percentile) are highlighted.

In this validation phase, a parallel workflow was performed, based on both CT and MR imaging.
Firstly, patients were scanned with a big bore Brilliance CT scanner (Philips Medical System, Amsterdam, The Netherlands), with 120 kVp and 3 mm of slice thickness. All patients were in a supine position, with knee support and fixation of the feet. The CT room is equipped with external laser system; tattoos were applied to patients at this stage. Moreover, no dietary restriction prior to the session were asked, only to drink 0.5 l of water, half an hour before the imaging acquisition to have a filled bladder. Once the first acquisition was performed, patients were asked to visit the toilet and then drink 0.5 l of water again. Therefore, after half an hour the MRI acquisition were performed on a 70 cm wide-bore Magnetom Aera 1.5 T MR scanner (Siemens Healthcare, Erlangen, Germany), with the T1-weighted 3D VIBE Dixon, described in section 2.1.1. The patients were positioned in the MR scanner just like in the CT scanner, on the dedicated flat table-top, with fixation of feet and with knee support, and with 18-channel body RF coils, as visible in Fig. 7.
Once the double set of images were acquired, the CT images were contoured manually by the radiation oncologist, while the MR ones are automatically contoured by ADMIRE software (research version 1.13.5, Elekta AB, Stockholm, Sweden); only the PTV was drown manually in both cases. Then the treatment plan was calculated on CT images with the same specifications as in the previous case, so a X-rays Voxel Monte Carlo algorithm with 0.3 cm grid-size and 2% MC uncertainty per calculation in Monaco® TPS (version 5.51, Elekta AB, Stockholm, Sweden). The plan was optimized to have an adequate target coverage and to respect the dose constraints used in our hospital (Table 6) [110]. Hence, the optimized plans were copied using the same field arrangements and shifts respect to imaging isocenter, and recalculated on the sCT images, obtained by MRI. In addition, the

same plan was optimized again with the same plane constraints, and then recalculated. The dose evaluation was performed using DVH parameters and 2D γ-analysis also in this case.

2.4.1. DOSE VOLUME HISTOGRAM (DVH)

The relative differences between dose distribution in CT and sCT were calculated for the relevant DVH points of PTV coverage and OARs dose constraints (bladder, femoral heads and rectum).
For the PTV, these were the minimum coverage dose of 95% of the target (D95), the near-minimum (D98), the near-maximum (D2) and the median (D50) absorbed doses in agreement with the recommendations from the ICRU report n. 83 [120].
The constraints used in our center [110] and evaluated in this work are reported in Table 6.
In addition, mean dose of all the mentioned OARs were evaluated. For all of them, the percentage difference was evaluated subtracting the CT value to the MR one, and dividing the result by the CT value, considering in this way the CT as the gold standard. An acceptance criterion can be identified from a comparison with the literature, where dose differences ranged up to 2.0% for different DVH parameters considered [15, 22, 39].

Organ at Risk	Parameter	Constraint (%)
Bladder	V40	60
	V65	50
	V70	35
Femoral Heads	D_{mean}	45
Rectum	V40	40
	V50	50
	V65	20
	V70	10

Tab. 6: List of DVH constraints used in our hospital [107].

2.4.2. GAMMA ANALYSIS

The gamma evaluation method was proposed by D. Low more than twenty years ago [101] for comparison of two dose distributions; it consider both dose (Dose Difference, %Diff) and spatial differences (Distance-to-Agreement, DTA) between them.
This method is applicable in 1 to 3 spatial dimensions. There are three essential parameters to take into account on gamma analysis: %Diff, DTA and dose threshold. The latter consists of the percentage value that rejects the dose points below the dose threshold chosen of the planned maximum dose. The Report of the AAPM Task Group 119 [102] asserts that 3% for %Diff and 3 mm for DTA are the most common criteria with dose threshold value equal to 10%; the acceptable threshold of gamma passing, defined as the ratio between the number of points that passes the gamma calculation and the total number of points evaluated, is assessed to be 90%.

In this thesis, 2D local γ-analysis with 10% of dose threshold was performed to compare the dose distributions between the CT and sCT CT-based plans and CT and sCT MRI-based plans. The criteria of 3%-3mm, 2%-2mm, 2%-1mm 1%-1mm are used to compare 2D dose distributions in the all planes and in the most significant slices (i.e. anatomical regions in the presence of bones, bladder and rectum). The calculations were performed by SNC Patient™ software (Sun Nuclear, Melbourne, Florida, USA). γ-analysis with 10% of dose threshold acceptance criteria, chosen for dose calculation on sCT, were pass rate >99% for 3%-3mm, >98% for 2%-2mm and >95% for 2%-1mm.

2.5. PATIENT SETUP VERIFICATION

The workflow ends with creation of reference images for patient setup verification prior to treatment delivery. There are few works reported in the literature dealing with this subject; CBCT images are used in most cases, with a large part of the studies performed manually [85, 103, 104].
In this thesis, the feasibility of matching the daily CBCT and MR reference images was verified on the X-ray Volume Imaging (XVI) at Synergy-S linac (Elekta AB, Stockholm, Sweden), through visual evaluations by different radiation oncologists; in this way the inter and intra observer variability is tested.
The patient setup verification in an MRI-only workflow does not differ in principle from that in the CT-based workflow. However, in order to be able to send images from Monaco® (version 5.51, Elekta AB, Stockholm, Sweden) to XVI, it is necessary to change the image modality in the SOP classes, transforming it from MR to CT; this was done automatically by a script.

Fig. 19: Patient positioned on rigid flat table in the linac bunker, with fixation devices, ready for CBCT acquisition.

The CBCT acquisition was performed with 120 kV, 660 mAs, F0 filter and medium collimator FOV; the patient was positioned in the same way as in the MR scanner, as shown in Fig 19.

Patient	# CBCT	Age
1	12	78
2	5	77
3	5	67
4	22	70
5	11	55
6	11	81
7	9	70
8	7	69
9	17	73
10	10	77
11	10	75
12	9	73
13	10	80
14	5	83
15	5	80
16	10	70
17	5	72
18	10	75
19	8	66
20	5	77
Mean	**9**	**73**
Range	5 - 11	70 - 78

Tab. 7: List of patients used to determinate average shifts in patient positioning with CBCT images. Number of CBCT images acquired and age are reported. In the last two rows Mean values and Range (25^{th} percentile – 75^{th} percentile) are highlighted.

Once the acquisition was performed, the CBCT images were compared with both CT and MR ones, previously rigid registered each other by translation only, following the protocol used in our hospital. In the usual CT-based workflow, the comparison between CT and CBCT images is performed in three different way: an automatic match based on both gray levels and bones in the clip box around the target region, and subsequently a manual one. The results of the described

method are evaluated by the radiation oncologist and the properly shifts are chosen. In our hospital the adopted protocol is an off-online CBCT one. It consists in the acquisition of the kV images during all the 5 fractions in the first week; subsequently, average shifts are calculated and used in the following fractions. A CBCT is performed at the beginning of each treatment week as a check.
In this work, for the patients presented in Table 5, matches between CT and CBCT images of different fractions were performed by different radiation oncologists. Therefore, the obtained shifts were compared with the ones obtained by manual match with the MR image, and the resulting discrepancies are analyzed. In addition, 20 patients, presented in Table 7, that performed prostate RT on the Synergy-S linac, were selected in order to evaluate an average shift in their in room-verification positioning; the obtain results were then used as a comparison with those previously achieved.

RESULTS

3.1. MR IMAGING

3.1.1. MR SEQUENCE

MRI sequence used for MRI-only planning workflow was an optimized 3D T1 VIBE Dixon gradient echo. It was obtained starting from a standard sequence duration of 40 minutes; the clinical sequence is now only 2 minutes and 30 seconds long. It is a good compromise between image quality and acquisition time, reducing the breathing artifacts, which generally creates distortions in OARs, such as the bladder and the discomfort of the patient. The optimization process is shown in Fig. 20, where the original sequence, an intermediate step lasting 5 minutes and the final result are displayed. This new short sequence permits also a good maintaining of patient position reducing discomfort and then related movement artifacts.

Fig. 20: Optimization step of Dixon sequence: original sequence lasting 42 minutes (A), an intermediate acquisition (5 minutes) (B) and the final result, 2 minutes and 30 seconds long (C).

3.1.2. ACQUISITION SETUP

Patients positioning accuracy is mandatory to ensure a reproducible daily setup. A flat table-top, feet and knee supports, suitable markers and a calibrated laser system are required to achieve this. In particular, a calibrated laser system is essential for correct patient positioning in the scanner before acquisition. An external laser system is commonly installed in the CT room; periodically, a dedicated QA program is executed on it. Before making the MR-based workflow a standard, an MR safe external laser system was not available. Therefore, internal laser system of the MRI scanner was used: QA measurements were fundamental to check if the laser cross, projected from a single point inside the scanner, was not tilted.

For all the three cases of section 2.1.2, the differences from the isocenter, due to the rotation of the laser cross, are reported in Table 8 together with the related tilt angle values, as described in detail in Fig. 21. For all the three setup configurations, the measured distances are consistent between them, leading to tilt angles very similar to each other at the 2 different distances: (0.3° both at 15 and at 20 cm).

These measurements were made in three different slices corresponding to different heights in the phantom and were repeated 2 months apart to assess repeatability and any drift.

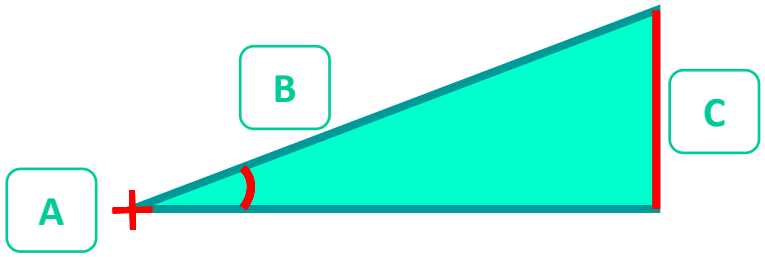

Fig. 21: Scheme of measured distance (C) and relative tilt angle (B) from the isocenter (A).

Position	Slice Height	Distance to Center (mm)	Distance (mm) (±0.4 mm)		Tilt Angle (°) (±0.2°)		Distance to Edge (mm)	Distance (mm) (±0.4 mm)		Tilt Angle (°) (±0.2°)	
Center - Left	Up	150	0.5	**0.6**	0.2	**0.2**	200	0.7	**0.7**	0.2	**0.2**
	Middle		0.6		0.2			0.7		0.2	
	Down		0.7		0.3			0.8		0.2	
Center - Right	Up	150	1.0	**1.1**	0.4	**0.4**	200	1.2	**1.3**	0.3	**0.3**
	Middle		1.3		0.5			1.4		0.4	
	Down		0.9		0.3			1.1		0.3	
Left - Right	Up	280	1.2	**1.0**	0.5	**0.4**	380	1.4	**1.2**	0.4	**0.4**
	Middle		0.8		0.3			1.0		0.3	
	Down		1.1		0.5			1.1		0.3	
Mean				**0.9**		**0.3**			**1.1**		**0.3**

Tab. 8: List of evaluations on laser system. Distances and tilt angles, averages of two different measurements, reported for three representative heights in the phantom. In bold their mean values are highlighted. In the last row Mean values of different measurements setup are shown.

3.1.3. GEOMETRIC DISTORTIONS

Although phantom studies experiments are unlikely to reflect the full complexity of the clinical case, the results of measurements made on the cylindrical grid MRI Leksell phantom (Elekta AB, Stockholm, Sweden) are reported below. The mean differences between consecutive grid points obtained for the axial section, in horizontal and in vertical directions, and for the coronal section in all the four FOV positions described in Fig. 14, are shown in Table 9. Difference between the calculated mean distance and the nominal distance (in red) were less than 2 mm for all views and for the four tested positions with radial distances lower than 30 cm from the isocenter.

View	Central (mm) (±0.7 mm)	Left (mm) (±0.7 mm)	Right (mm) (±0.7 mm)	Central Up (mm) (±0.7 mm)	Nominal (mm)
Horizontal	20.3	20.0	20.1	20.3	**20**
Vertical	30.2	30.2	30.1	30.3	**30**
Coronal	20.3	20.4	20.7	20.5	**20**

Tab. 9: Distances between consecutive points for different views and position in the FOV. On the last column, the nominal reference is reported.

3.2. CONTOUR DELINEATION AND SCT GENERATION

The acquired MRI images of 7 patients reported in Table 5, were automatically contoured by Admire software (research version 1.13.5, Elekta AB, Stockholm, Sweden), as described in section 2.2.1. The average time taken for this operation is shown in the Table 10 for each patient: a further 5 to 10 minutes are necessary for the radiation oncology to better define some contours and to draw the target. The contoured images obtained were validated by both a radiologist and the senior radiation oncologist who followed the all work.

Patient	Time (min:sec)
1	18:03
2	20:57
3	22:13
4	17:54
5	19:52
6	19:28
7	18:48
Mean	**19:36**
Range	18:26 - 20:25

Tab. 10: List of times taken by Admire to auto-contour each patient. In the last row the Mean value and the Range (25th percentile – 75th percentile) are highlighted.

An example of the Admire output is shown below in Fig. 22.

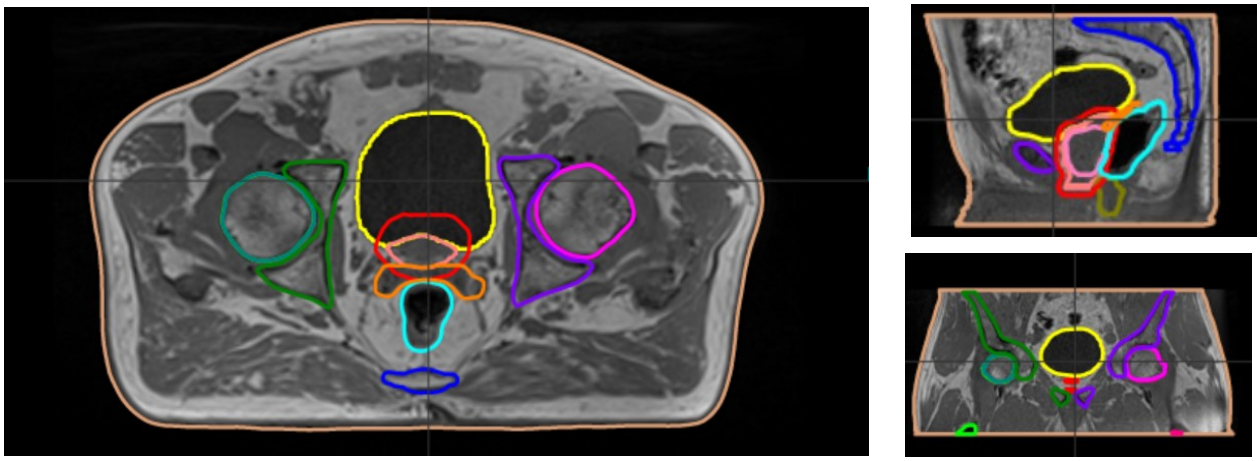

Fig. 22: Example of MR images automatically contoured by Admire software.

3.2.1. Electron Densities

The average ED values of each structure, taken in the previous work from work a set of 20 patients who underwent radiotherapy for prostate cancer during 2019 and used in this thesis, are listed in Table 11.

Structure	Electron Density (g/cm^3)
Bladder	1.030
External	1.000
Femoral Head_L	1.170
Femoral Head_R	1.170
Femur_L	1.225
Femur_R	1.225
Pelvis_L	1.196
Pelvis_R	1.196
Prostate	1.000
Rectum	0.992
Sacrum	1.110
Seminal Vesicles	1.000

Tab. 11: List averaged EDs used for each structure in this work.

3.3. DOSIMETRIC EVALUATION

The dosimetric evaluation on sCTs consisted of two different phases. In the first one, the EDs assignment was assessed by the comparison of dose distributions obtained on the same CT images, in which only the EDs were changed, passing from a continuous value to a fixed one.

As an example, in Fig. 23 are reported dose distributions and DVH of both CT-based plan and sCT-based one for a single patient. In more detail the DVH of both plans is shown in Fig. 24.

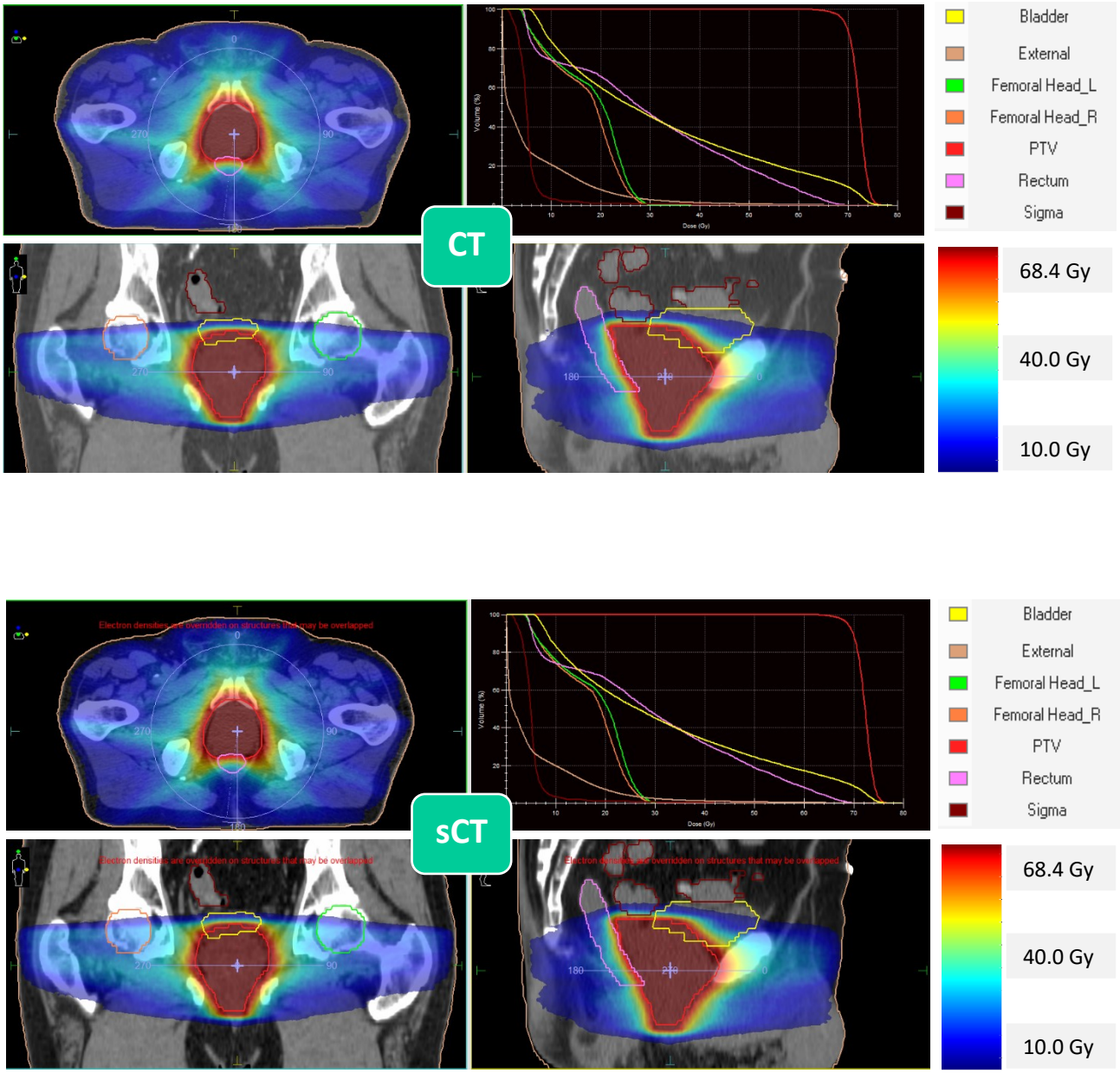

Fig. 23: Example of CT-based plan (top) and sCT-based one (bottom), in which a fixed ED was assigned for each structure.

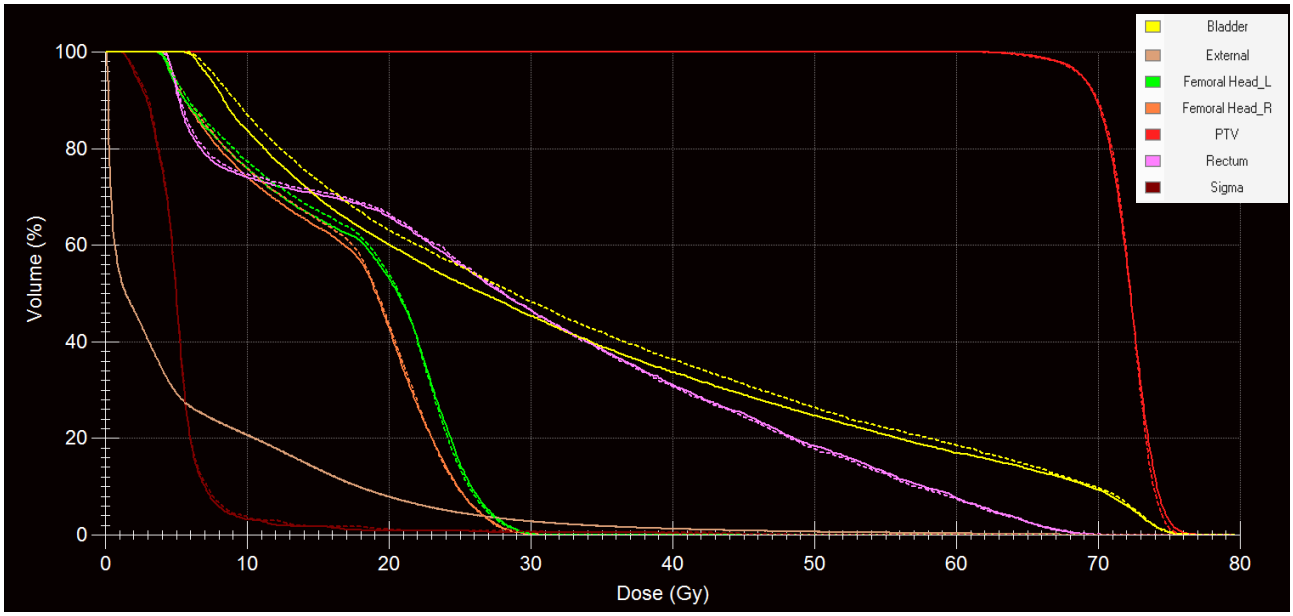

Fig. 24: Example of DVH comparison between CT-based plan (continuous line) and sCT-based one (dashed line) reported in Fig. 22.

The comparison between the two image types was performed considering the CT as the gold standard; the mean differences of DVH parameters in terms of PTV coverage and OARs constraints (see Table 6) are reported in Table 12.

Structure	DVH Parameter			
	D98	**D95**	**D2**	**D_{mean}**
PTV (Prostate Gland)	**0.31**	**0.33**	**0.82**	**0.57**
	-3.15	-3.08	0.05	-1.24
	0.99	1.19	1.80	0.90
	D98	**D95**	**D2**	**D_{mean}**
PTV 2* (Seminal Vesicles)	**0.12**	**0.14**	**0.69**	**0.18**
	-1.71	-1.56	0.03	-1.35
	0.68	0.69	1.21	0.64
	D98	**D95**	**D2**	**D_{mean}**
PTV 3** (Pelvi)	**0.66**	**0.59**	**0.51**	**0.55**
	0.58	0.55	0.49	0.55
	0.74	0.64	0.52	0.56

	V65	V40	D_{mean}
Bladder	**1.85**	**-0.25**	**0.14**
	-0.40	-9.86	-6.41
	1.40	5.90	1.25
		Dmean L	**Dmean R**
Femoral Head		**0.10**	**0.13**
		-1.22	-1.57
		1.00	1.09
	V50	**V40**	D_{mean}
Rectum	**5.03**	**2.41**	**1.06**
	1.00	-1.05	-0.87
	10.12	4.31	1.75

** Only 7 patients.*

*** Only 3 patients.*

Tab. 12: List of mean deviations of DVH parameters for PTV and OARs of 20 considered patients. The reported values are the percentage difference between CT and sCT, where CT was considered as gold standard. From top to bottom of each structure: the average value (red), the minimum and the maximum ones (in blue).

In more detail, differences in PTV coverage and Bladder, Femoral Head and Rectum constraints between CT and sCT are presented in Fig. 25, 26, 27, 28.

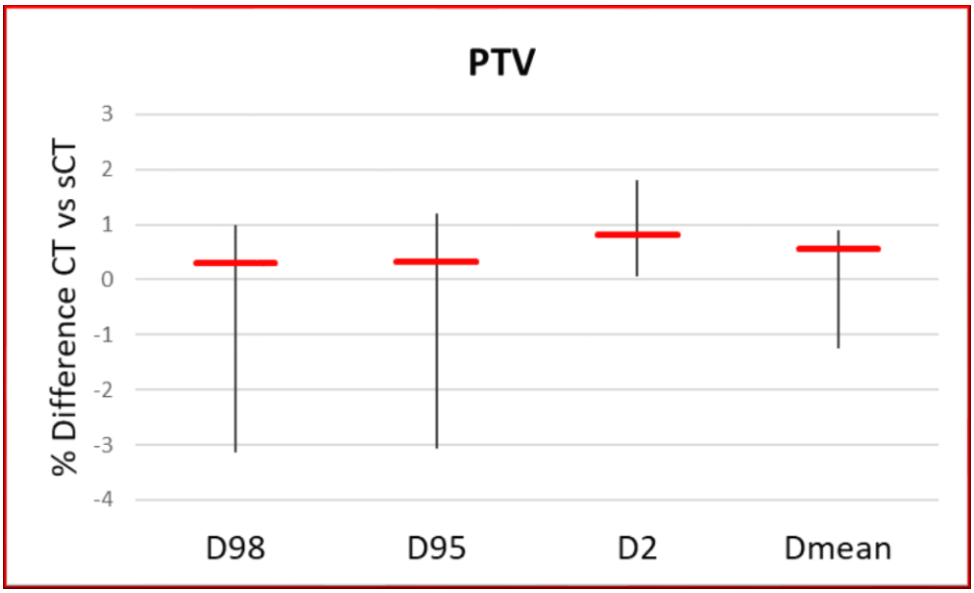

Fig. 25: Mean deviations and range of PTV DVH-parameters (D98, D95, D2, D_{mean}) for the 20 considered patients. The CT was considered as gold standard.

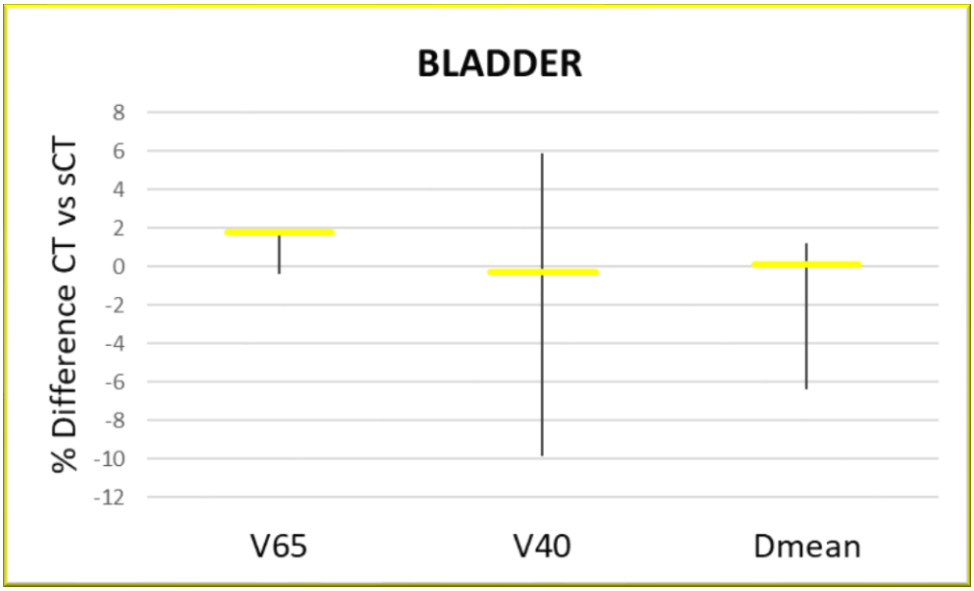

Fig. 26: Mean deviations and range of Bladder DVH-parameters (V65, V40, D_{mean}) for the 20 considered patients. The CT was considered as gold standard.

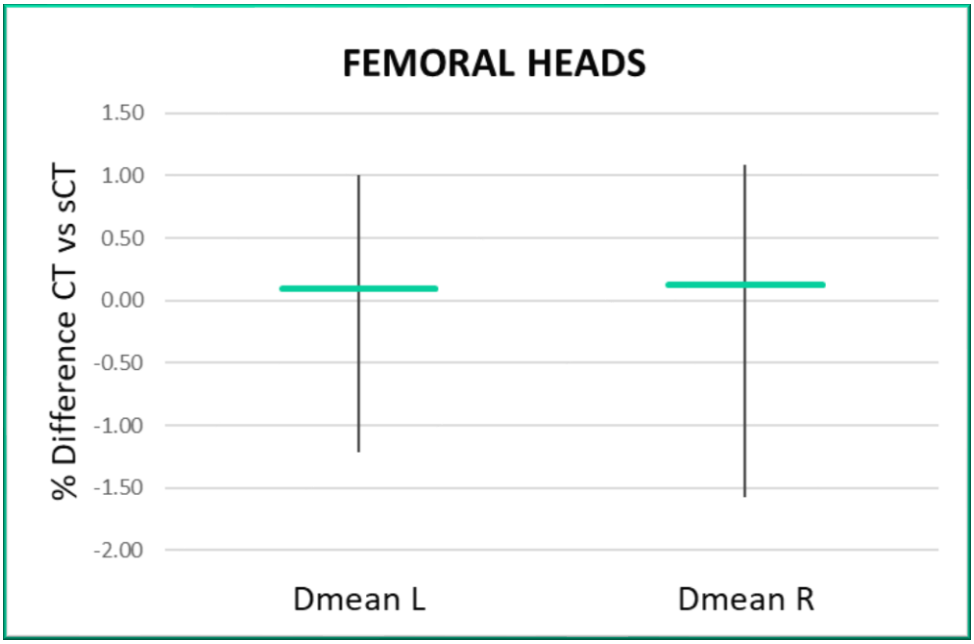

Fig. 27: Mean deviations and range of Femoral Heads DVH-parameters (D_{mean} L, D_{mean} R) for the 20 considered patients. The CT was considered as gold standard.

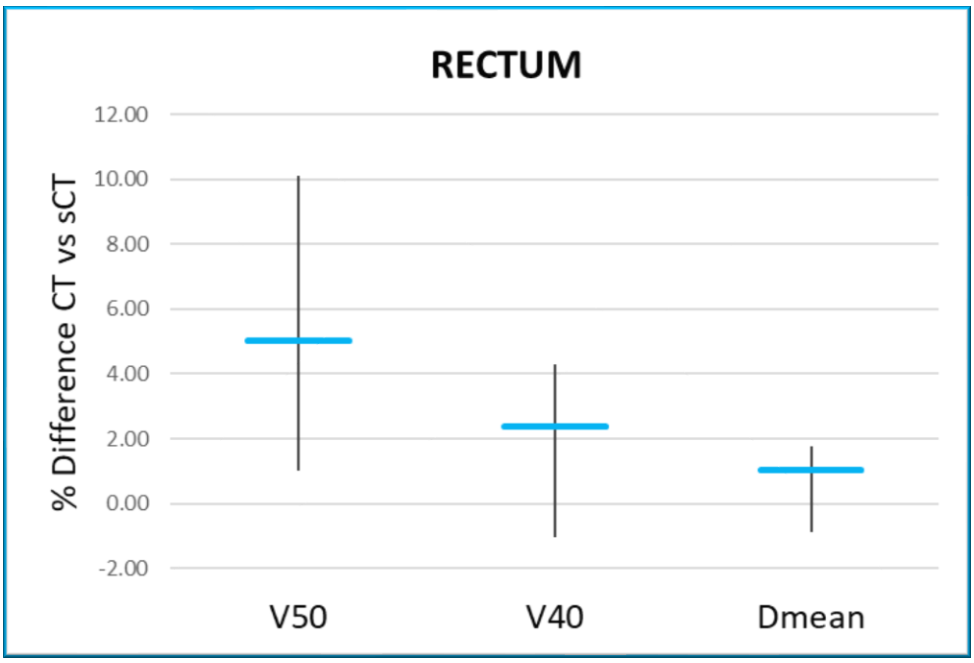

Fig. 28: Mean deviations and range of Rectum DVH-parameters (V50, V40, D_{mean}) for the 20 considered patients. The CT was considered as gold standard.

Further evaluations were performed by 2D local γ-analysis, as described in section 2.3.2. The obtained results for all three views are reported in Table 13.

View	3%-3 mm	2%-2 mm	2%-1 mm	1%-1 mm
Transverse	**99.9**	**99.4**	**97.5**	**87.1**
	99.4	97.7	94.6	78.3
	100.0	99.9	99.4	92.5
Coronal	**99.7**	**98.7**	**96.2**	**86.1**
	96.4	91.5	83.2	66.2
	100.0	99.7	98.5	90.9
Sagittal	**99.6**	**98.5**	**95.3**	**85.8**
	95.4	89.6	80.8	67.9
	100.0	99.6	97.8	92.4

Tab. 13: List of 2D γ-analysis score, evaluated over 20 patients for transverse, sagittal and coronal views with different combination of %Diff and DTA parameters. From top to bottom of each view: the average value (red), the minimum and the maximum ones (in blue).

Afterwards, the combination between the assignment of an average ED and the different contours in the two imaging modalities was evaluated. This phase consisted of two different steps. In the first one, the optimized plans, calculated on the CT images, were copied using the same field arrangements and recalculated on the sCTs, obtained by MRI. The results of mean DVH differences comparisons in terms of PTV coverage and OARs constraints are reported in Table 14.

Structure	DVH Parameter			
PTV (Prostate Gland)	**D98**	**D95**	**D2**	**D_{mean}**
	-1.41	**-0.90**	**-0.41**	**-0.34**
	-5.46	-2.62	-2.52	-1.35
	0.15	-0.07	1.28	1.03
PTV 2* (Seminal Vesicles)	**D98**	**D95**	**D2**	**D_{mean}**
	-1.14	**-0.51**	**0.65**	**1.15**
	-2.31	-1.11	-0.05	0.12
	0.29	0.05	1.28	2.64
Bladder		**V65**	**V40**	**D_{mean}**
		-27.49	**-33.48**	**-23.89**
		-45.93	-44.41	-35.37
		-1.13	-20.04	-6.46
Femoral Head			**Dmean L**	**Dmean R**
			-2.00	**-0.92**
			-7.68	-10.26
			15.21	12.15
Rectum		**V50**	**V40**	**D_{mean}**
		53.68	**25.99**	**11.66**
		29.50	13.36	10.11
		80.72	42.3	13.85

** Only 3 patients.*

Tab. 14: List of mean deviations of DVH parameters for PTV and OARs of 7 considered patients with CT and MRI images. The reported values are the percentage difference between CT and sCT plans with the same field arrangements, where CT was considered as gold standard. From top to bottom of each structure: the average value (red), the minimum and the maximum ones (in blue).

Subsequently, the previous plans were optimized on the new target and OAR volumes, defined on MR images, with the same plan constraints as CT-based ones; the relative evaluations are shown in Table 15.

Structure	DVH Parameter			
PTV (Prostate Gland)		**D98**	**D95**	**D2**
		-0.89	**-0.52**	**-0.01**
		-3.51	-2.89	-1.17
		1.48	0.86	0.99
PTV 2* (Seminal Vesicles)	**D98**	**D95**	**D2**	**D_{mean}**
	-1.18	**-0.67**	**0.15**	**0.17**
	-1.41	-0.77	-0.09	0.05
	-0.78	-0.56	0.38	0.26
Bladder		**V65**	**V40**	**D_{mean}**
		-36.85	**-27.68**	**-22.24**
		-46.41	-63.14	-52.37
		-26.69	4.46	6.63
Femoral Head			**Dmean L**	**Dmean R**
			-2.11	**-0.72**
			-11.49	-6.74
			9.55	7.96
Rectum		**V50**	**V40**	**D_{mean}**
		7.88	**7.74**	**4.22**
		4.56	3.76	-2.44
		11.98	15.01	14.00

** Only 3 patients.*

Tab. 15: List of mean deviations of DVH parameters for PTV and OARs of 7 considered patients with CT and MRI images. The reported values are the percentage difference between CT and sCT plans with re-optimized MR-based one, where CT was considered as gold standard. From top to bottom of each structure: the average value (red), the minimum and the maximum ones (in blue).

In both analyzed cases, the isocenter of the plane was chosen with the same shifts used in the CT-based plane, starting from the isocenter of the images.
Differences in PTV coverage and Bladder, Femoral Head and Rectum constraints between the two methods described above are presented in Fig. 29, 30, 31, 32.

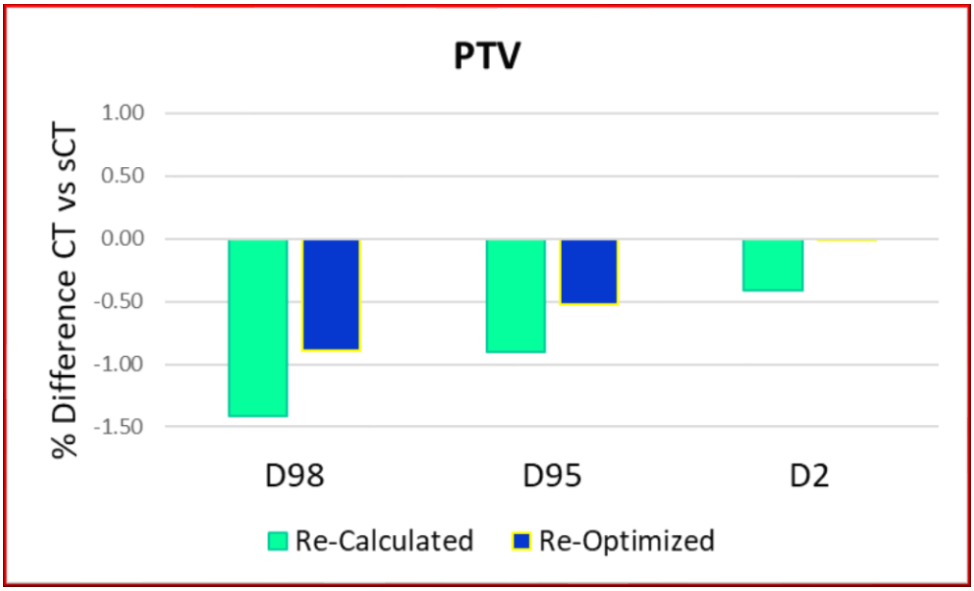

Fig. 29: Mean deviations and range of PTV DVH-parameters (D98, D95, D2, Dmean) for both the tests performed on the 7 considered patients. The CT was considered as gold standard.

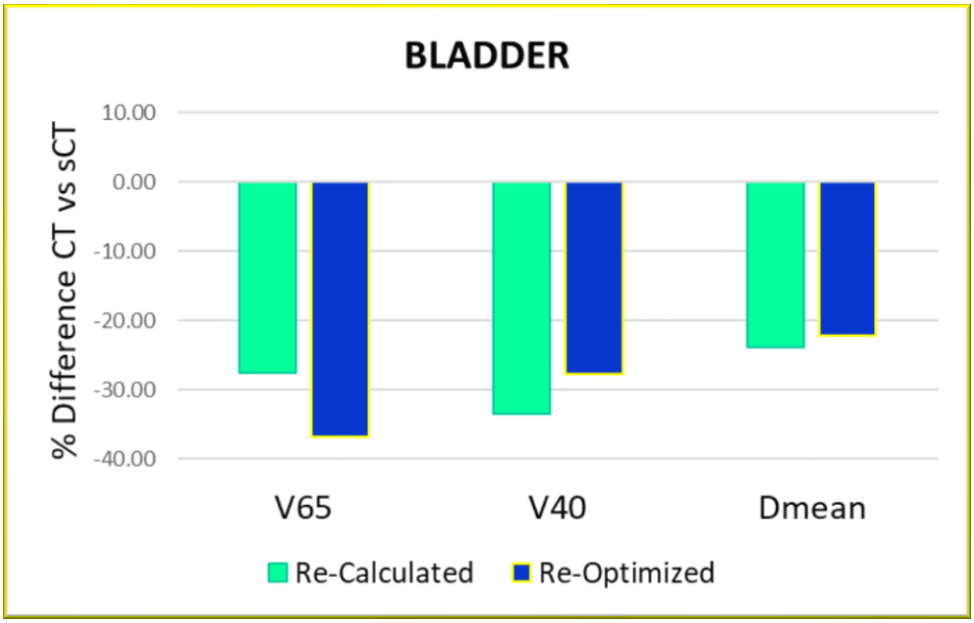

Fig. 30: Mean deviations and standard deviations of Bladder DVH-parameters (V65, V40, D_{mean}) for both the tests performed on the 7 considered patients with both CT and MRI images. The CT was considered as gold standard.

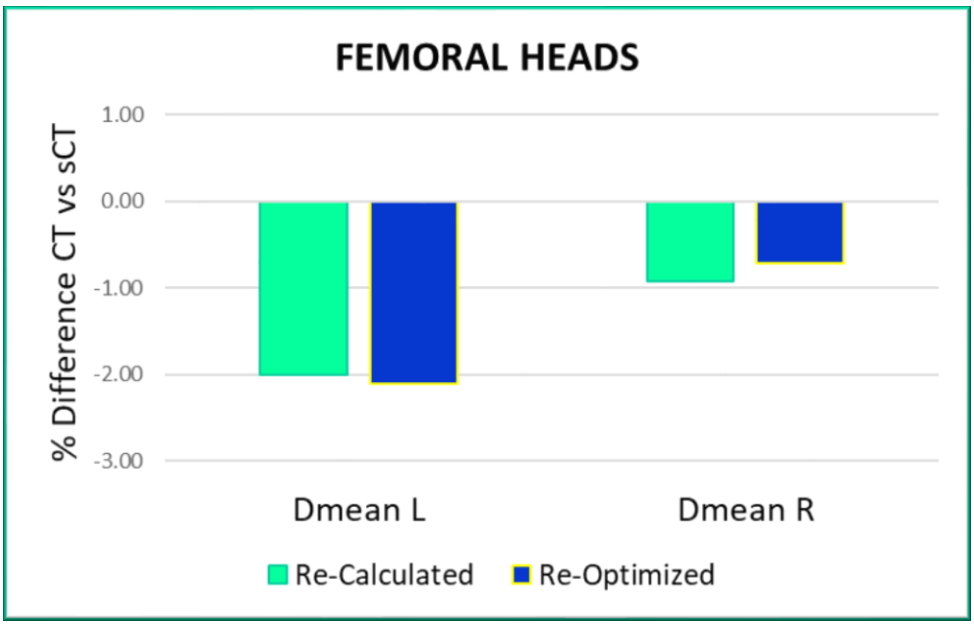

Fig. 31: Mean deviations and standard deviations of Femoral Heads DVH-parameters (D_{mean} L, D_{mean} R) for both the tests performed on the 7 considered patients with both CT and MRI images. The CT was considered as gold standard.

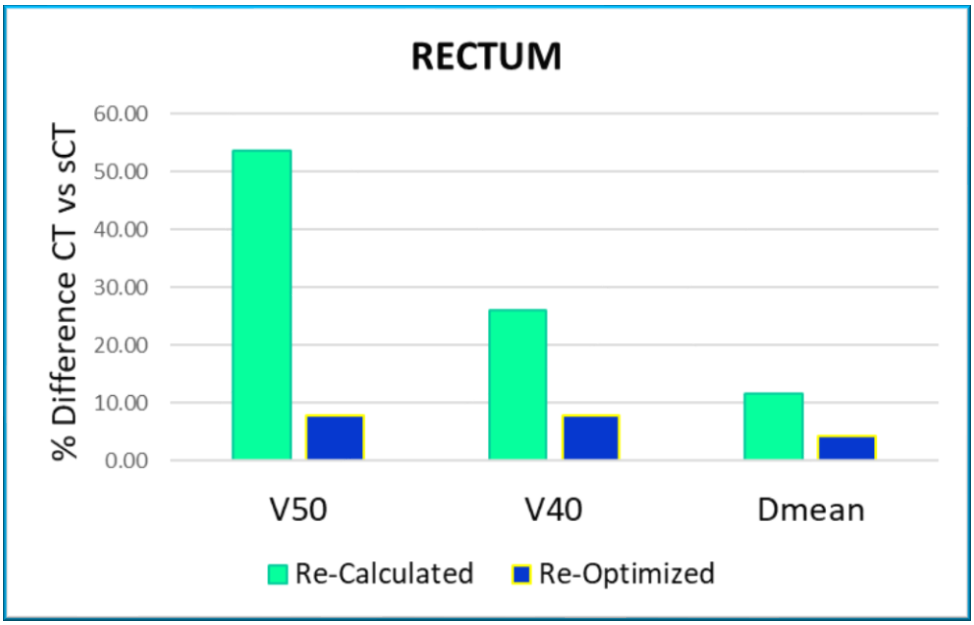

Fig. 32: Mean deviations and standard deviations of Rectum DVH-parameters (V50, V40, D_{mean}) for both the tests performed on the 7 considered patients with both CT and MRI images. The CT was considered as gold standard.

To better understand these results, a relevant example of differences of both bladder and rectum anatomies is reported below in the Fig. 33. From the CT images it is evident that the contours are changed noticeable during time between two acquisitions. So the obtained differences can be explained considering how the CT and MR were acquired: the two imaging modalities in fact were performed one after the other, with the patient that had to visit the toilet after the CT acquisition

and repeat the training by drinking half a liter of water. So, despite these cautions, the filling of the bladder and rectum was different, leading to a systematic underdosage of the bladder, and a resulting increase of dose in the rectum [121].

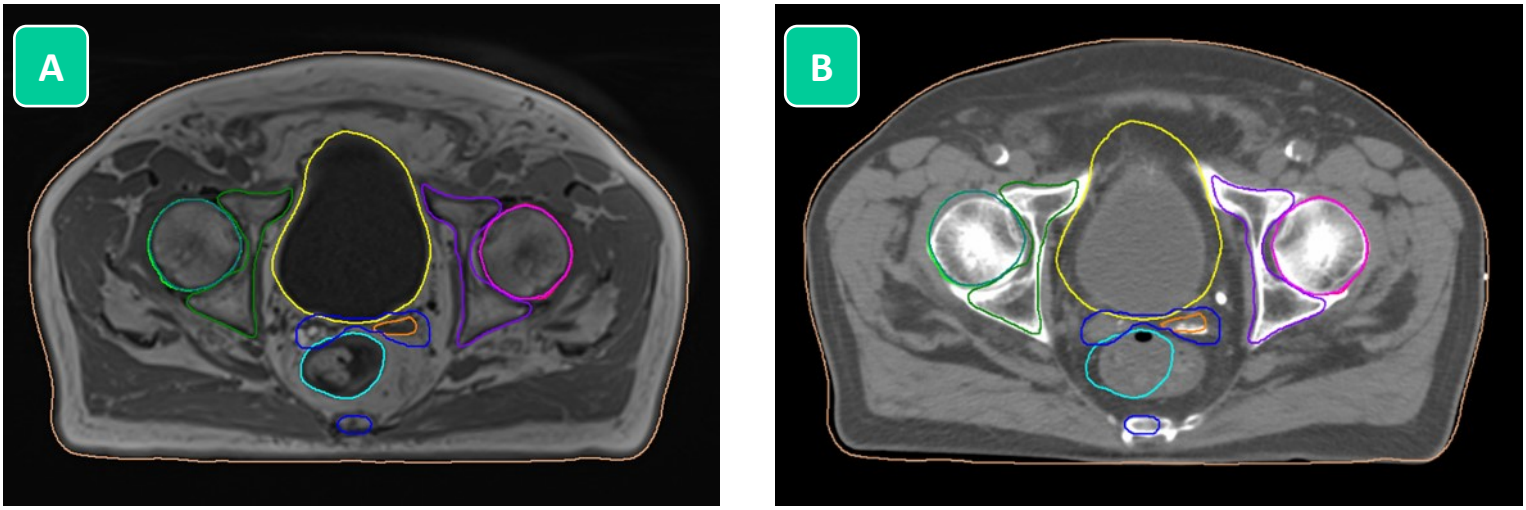

Fig. 33: Example of difference in patient anatomy between two different and consecutive acquisition, carried out with a same training. On the left, the MR images (A), while on the right the CT images where structures contoured on MR are copied (B).

In addition, compliance with the constraints, listed in Table 6, was evaluated for the re-optimization plans on MRI; the results are shown in the Table 16.

Patient	PTV	BLADDER		FEMORAL HEADS		RECTUM		
	D95	V60	V40	Dmean L	Dmean R	V70	V65	V40
1	☑	☑	☑	☑	☑	☑	☑	☑
2	☑	☑	☑	☑	☑	☑	☑	☒
3	☑	☑	☑	☑	☑	☑	☑	☑
4	☑	☑	☑	☑	☑	☑	☑	☑
5	☑	☑	☑	☑	☑	☑	☑	☑
6	☑	☑	☑	☑	☑	☑	☑	☑
7	☑	☑	☑	☑	☑	☑	☑	☑
Score	**7/7**	**7/7**	**7/7**	**7/7**	**7/7**	**7/7**	**7/7**	**6/7**

Tab. 16: List of compliances with the constraints for the plans re-optimized on sCT generated by MR images.

3.4. PATIENT SETUP VERIFICATION

The position shifts in the matching between CBCT and CT or MR images, and their differences, obtained through visual evaluation by three different radiation oncologists, are reported in Table 17 for selected fractions. The match between CBCT and CT was considered as the gold standard. Note that CT and MRI were previously registered by translating the isocenter of the planning images.

# Fraction	Lateral Shifts (cm)				
	CT	MR 1	MR 2	MR 3	Mean Difference
1	0.20	-0.20	-0.07	-0.06	0.31
2	-0.13	-0.06	-0.13	-0.30	0.03
3	0.20	-0.20	-0.20	-0.67	0.56
4	0.35	-0.27	0.00	-0.20	0.51
5	0.30	0.00	0.07	-0.11	0.31
6	-0.09	-0.13	-0.47	0.00	0.11
7	-0.39	-0.87	-0.87	-0.08	0.22
8	-0.15	-0.20	-0.60	-0.20	0.18
9	0.13	-0.13	-0.27	-0.10	0.30
Mean	**0.05**	**-0.23**	**-0.28**	**-0.19**	**0.28**
Range	-0.39 - 0.35	-0.87 - 0.00	-0.87 - 0.07	-0.67 – 0.00	0.03 – 0.56

# Fraction	Longitudinal Shifts (cm)				
	CT	MR 1	MR 2	MR 3	Mean Difference
1	-0.50	0.60	0.33	0.27	0.10
2	-0.45	0.00	0.27	0.47	0.20
3	0.16	0.13	0.13	0.37	-0.05
4	-0.07	-0.30	0.47	0.03	-0.14
5	0.69	0.93	0.80	0.55	-0.07
6	0.32	0.53	0.20	-0.45	0.23
7	0.16	-0.13	0.33	0.27	0.00
8	0.27	0.40	0.27	0.30	-0.05
9	0.16	0.20	0.18	0.50	-0.13
Mean	**0.08**	**0.26**	**0.33**	**0.26**	**0.01**
Range	-0.50 - 0.69	-0.30 - 0.93	0.13 - 0.80	-0.45 – 0.55	-0.14 – 0.23

# Fraction	Vertical Shifts (cm)				
	CT	MR 1	MR 2	MR 3	Mean Difference
1	-0.10	-0.29	-0.49	-0.29	0.26
2	-0.06	-0.42	-0.49	-0.39	0.37
3	-0.12	-0.69	-0.42	-0.22	0.32
4	-0.30	-0.55	-0.62	-0.22	0.16
5	-0.03	-0.42	-0.56	-0.44	0.44
6	0.25	-0.16	-0.56	-0.91	0.61
7	0.15	-0.56	-0.42	-0.77	0.64
8	-0.07	0.11	-0.55	-0.62	0.28
9	0.24	-0.16	0.42	-0.49	0.32
Mean	**0.00**	**-0.35**	**-0.42**	**-0.48**	**0.38**
Range	-0.30 - 0.25	-0.69 - 0.11	-0.62 - 0.42	-0.91 – 0.22	0.16 – 0.64

Tab. 17: List of measured shifts in CBCT-CT matching and CBCT-MR matching for different fractions and patients. From top to bottom: lateral, longitudinal, and vertical views. The visual evaluation on MR images were performed by three different observers, and the mean difference between the shifts in the two modalities are reported. In the last two rows: the average value (red), the minimum and the maximum ones (in blue).

In addition, the mean shifts obtained with the in-room verification positioning are compared with those of 20 patients previously treated using CBCT-CT match method, as shown in Table 18.

Lateral Shifts (cm)		Longitudinal Shifts (cm)		Vertical Shifts (cm)	
CT	MR	CT	MR	CT	MR
0.02	**-0.23**	**0.12**	**0.30**	**-0.07**	**-0.41**
-0.58 - 0.37	-0.87 - 0.04	-0.38 - 0.49	0.09 - 0.87	-0.42 - 0.17	-0.91 - 0.13

Tab. 18: Comparison of measured shifts in CBCT-CT matching and CBCT-MR matching for 20 patients previously treated with only CT and MRI-only patients. The red value is the average, the blue ones the minimum and the maximum.

DISCUSSIONS

The clinical implementation of MRI-Only radiotherapy treatment workflow for prostate cancer in a big multi-purpose hospital was investigated in this thesis. The resources available in Niguarda hospital were used in this work: a 1.5 T MRI-scanner (Magnetom Aera, Siemens Healthcare, Erlangen, Germany) and a standard linac (Synergy-S, Elekta AB, Stockholm, Sweden) were exploited. Here below several aspects of the implementation, examined in this thesis and in a previous work [103, 104], are discussed and compared with those of published works. There are no international agreement and shared guidelines on the acceptance criteria: individual hospital employs their own until standards are established.
Finally, benefits and drawbacks of the presented method are pointed out, paying special attention to the applicability of the proposed approach in a hospital with similar characteristics to ours. Further possible developments are also included.

4.1. MR IMAGING

The first step necessary for the implementation of the MRI-only workflow is certainly the choice and optimization of a suitable MRI sequence. The 3D T1 VIBE Dixon gradient echo sequence used for this work is a good compromise between image quality and acquisition time; it takes 2 minutes and 30 seconds, reducing the artifacts due to organ motions, breathing and patient movements [60, 122]. The image quality was considered adequate by both the head of Radiology department and a senior radiation oncologist.
A further advantage is in the contouring process, since the Dixon techniques provides four contrasts, with a high signal to noise ratio due to GRE sequence, in one single simultaneous acquisition; in this way, some images are preferred to contour the bones, others to delineate the soft tissues, switching from one contrast to another one without losing accuracy in the delineation process.
In order to acquire images with appropriate accuracy, to ensure a reproducible daily setup of the patient, a flat table-top, feet and knee supports, suitable markers and a calibrated laser system are required.
The use of an 8 mm wooden bi-laminate rigid flat table, shown in Fig. 6, together with feet and knee supports, is basic for prostate radiotherapy [61, 62]. They allowed to ensure the same setup as during irradiation at linac with limited patient discomfort.
In the patient positioning procedure, markers are necessary to identify the positions of the tattoos, made on the patient's skin, where lasers are usually centered on during both the imaging acquisition and treatment delivery. Clearly, the metallic ones used in planning CT acquisitions could not be used in the MR room. After several attempts, where home-made and commercial solutions were tested with our sequence, the LiquiMark™ MRI Markers (Suremark® - Simi Valley, California, USA) were chosen, since provided the better contrast in our MR images. In addition, they are easy to apply on the patient's skin.
Furthermore, a calibrated laser system is essential for a correct patient positioning in the scanner before acquisition. An external laser system is usually installed in the CT room; as the feasibility of implementing the MRI-only workflow was considered in this work, an MR safe external laser system

has not yet been purchased. It was therefore decided to use the internal laser system of the MRI scanner, after an appropriate check that the laser cross, projected from a single point inside the scanner, was centered in the isocenter and not tilted. The measurement results, presented in Table 8, lead to a mean tilt angle of 0.3°± 0.2° (range 0.2° to 0.4°) in all positions tested. This means a position difference corresponding to approximately 1±0.4 mm at 15-20 cm from the isocenter. So, it was possible to use this laser in the workflow.

Finally, the geometric distortion issue was addressed. High geometry accuracy is mandatory for MR images used for RT purposes, characterized by a large FOV, since distortions increase in magnitude with the radial distance from the isocenter. Nevertheless, there are two possible sources of geometric distortion: system or scanner related distortions, caused by inhomogeneities in the main magnetic field and gradient nonlinearities, and patient-induced distortions due mainly to magnetic susceptibility variations at the interface of different tissues [24]. The firsts are easier to measure and there are several works in the literature that deal with them, while measurements of patient-dependent geometric distortion are quite rare in published reports.

Besides, geometric distortions can be reduced by using magnetic field shimming [66, 67]. MR scanner are equipped with passive and active shimming. In any case, a preliminary discussion with the scanner manufacturer was deemed mandatory. Furthermore, our MRI scanner systems features TrueForm™ Magnet Design (Siemens Healthcare, Erlangen, Germany) is optimized for each patient for a cylindrical shape of the homogeneous volume of the magnetic field and leads to a better depiction of the edges of the 3D FOV. This is particularly beneficial for large FOV coronal imaging as abdomen-pelvis, as in the studied case. So, the manufacturer's idea was that the active shimming corrects the distortions in a suitable way and no further measurements were needed, other than those performed twice a year by the vendor and every three months by us with the ACR phantom.

However, although phantom studies experiments are unlikely to reflect the full complexity of the clinical case, including differences in patient setup, the system-related geometric distortions were previously measured and quantified. Differences between the calculated mean distance and the nominal distance were less than 2 mm for all radial distances below 30 cm from the isocenter in all views for the Dixon sequence tested. These results are consistent with those of several works in the literature, where different 1.5 T MRI scanner vendors (GE, Philips, Siemens) and large FOV phantom manufacturers (Spectronic, Philips, home-made) are presented [118]. Indeed, Gustafsson et al. [65], Torfeh et al. [46], Wyatt et al. [69] and Wang et al. [64] agree in defining a geometric uncertainty of about 2 mm at 20-25 cm from the isocenter. Then in this work, the geometrical distortions due to MRI can be can consider reasonably acceptable.

4.2. CONTOUR DELINEATION AND sCT GENERATION

The delineation on the images of the various structures of interest is a necessary but time-consuming manual procedure. In particular, in the MRI-only method choice for this work, the process is even longer using MR images as more structures, than those usually identified on CT images due to the demands of dose constraints [110], need to be contoured in order to assign them the right ED to allow the TPS to perform the dose distribution calculation.

The automatic contouring process developed in this work was implemented thanks to the Admire software (research version 1.13.5, Elekta AB, Stockholm, Sweden) on a Tesla K40c GPU (NVIDIA Corporation, Santa Clara, Florida, USA) with 12 GB of memory, as described in section 2.2.1. In this

way, the 12 structures were identified on 176 slices of MR images in an averaged time less than 20 minutes (19 min, 36 sec), with a maximum of 20 minutes and 25 seconds. The delineation results needed only small adaptations and were considerable acceptable by the head of Radiology Department and a senior radiation oncologist; a further 5 to 10 minutes are necessary to better define some contours and to identify the target. This was possible thanks to the large number of patients inserted as atlases and their variability, which allowed to adequately contour even non-standard patients.

Therefore, this method allows to make automatic the contouring process, saving time for the radiation oncologist and also reduces inter-observer variability. On the other hand, this auto-contouring process takes too long and hinders the possibilities of online adaptive radiotherapy, which instead is made possible by deep learning techniques, passing from about 15 minutes to a maximum of 60 seconds [82].

Regarding the choice of ED values, the one assigned to the bladder is consistent with that reported in the ICRU Report n. 46 [88], while for the remaining OARs, not all the data are reported in the publication and those reported depend on the age of the patient. The averaged values were carried out starting from 20 patients with mean dose of 77 years old (range 70-82), consistent with the age interval of the patients considered in this thesis work (71 - range 69/77 – for the first phase, 76 – range 73/78 – for the second one).

4.3. DOSIMETRIC EVALUATION

The dosimetric evaluation on sCT consisted of two different phases. In the first one, the assignment of a bulk ED to each structure, passing from heterogeneous values to homogeneous ones on the same CT images, was assessed. After that, the combination of bulk EDs and automatic contours on MRI images was investigated. In all cases, the percentage difference with respect to the CT, considered as gold standard, was evaluated.

In the first part, the percentage dose differences observed between DVH parameters of sCT- and CT-based plans, reported in Table 12, were not statistically significant on a 95% confidence level for PTV, bladder and femoral heads. In more detail, the differences of all the four PTV coverage constraints were about 0.5%, and in any case never higher than 0.8%, both for the main PTV (prostate gland) and for the secondary ones (seminal vesicles and pelvis). The D95, used in the clinic routine to assess plan coverage, showed a mean difference of 0.3% for the main PTV. Also considering the OARs, the discrepancies were limited, especially for bladder and femoral heads. For instance, the percentage difference of bladder D_{mean} and V40 resulted equal to 0.14% and -0.25% respectively; V65 reached 1.85% but on a very small volume and therefore not clinically significant (few cc). Likewise, the femoral heads showed D_{mean} discrepancies close to zero in both sides. Higher differences were found for the rectum: while the mean dose was about 1%, the V40 and V50 reached 2.4% and 5.0% respectively. This could be explained by different rectal filling of each patient that leads to a higher discrepancy if an average ED, which do not distinguish between the rectal wall and its filling, is assigned to that structure.

The obtained results are consistent with those reported in published papers. Korsholm et al. [123] reported a PTV percentage difference lower than 0.5% and a mean dose in the rectum near to 1%, Persson et al. [22] showed a PTV percentage discrepancy of 0.2% in D95 and a dose to rectum up to

1.5% in the higher doses, and Tyagi et al. [25] achieved a 0.5% percentage difference for the difference structures.

To better estimate the differences in dose distributions all over the patient images, further evaluations were performed by 2D local γ-analysis with 10% of dose threshold in transverse, coronal and sagittal views of most significant planes, as described in section 2.3.2 and reported in Table 13. Four tolerance criteria were utilized: the 3%-3mm is the one used in the Niguarda clinical routine for pre-treatment dose plans verification, the 2%-2mm and 2%-1mm are adopted to be sure that the obtained differences remain limited even with more strict criteria, while 1%-1mm was used to be more demanding.

The passing rate of 3%-3mm was approximately 100% in all directions, ranging from 99.6% in sagittal view to 99.9% in the transverse plane. For a more relevant evaluation, the 2%-2mm and 2%-1mm criteria were investigated. For the first criterion, its behavior was similar to that of the previous case, with a passing rate from 98.5% to 99.4% in sagittal and transverse view respectively. The 2%-1mm showed a similar trend, with transverse view passing rate that reached a mean value of 97.5% and the sagittal one which resulted equal to 95.3%. However, all these three considered criteria lead to acceptable results. The 1%-1mm values ranged from 85.8% to 87.1% pointing out that this criterion is too strict.

The results obtained are comparable with those in the literature, although in each study there is a different dose threshold, from 10% to 20%. Christiansen et al. [12], Greer et al. [14] Persson et al. [22] estimated passing rate of approximatively 99% for 2%-2mm criterion, slightly higher than those obtained in this thesis, since they performed a 3D analysis.

It was therefore possible to confirm that the use of bulk EDs assignment is acceptable and can be used in the planning workflow.

Subsequently, the combination between the assignment of an average ED and the different contours in the two imaging modalities was evaluated. The isocenter of the plane was chosen with the same shifts used in the CT-based plane, starting from the isocenter of the images.

First of all, the optimized plans, calculated on the CT images, were copied using the same field arrangements and recalculated on the sCTs, obtained by MRI (see Table 14). Thus, the previous plans were optimized on the new target and OAR volumes, since they were defined on MR images, with the same plan constraints as CT-based ones; the relative evaluations are shown in Table 15.

In the recalculation step, despite the negative sign, the mean percentage differences in PTV coverage were all below the 1%, except D98 which reached -1.4%. On the other hand, the differences for OARs were considerably higher: bladder received a mean percentage dose of -24%, V40 and V60 were approximatively around -30%. The femoral heads constraints also diverged from CT ones, with a mean dose lower than 1-2%. The rectum instead showed the opposite behavior, with the D_{mean} equal to +11.5%, while V40 was +26% and V50 more than +50%. These results can be explained considering how the CT and MR were acquired: the two imaging modalities in fact were performed one after the other, with the patient that had to visit the toilet after the CT acquisition and repeat the training by drinking half a liter of water. So, despite these cautions, the filling of the bladder and rectum was different, leading to a systematic underdosage of the bladder, and a resulting increase of dose in the rectum.

A similar behavior also occurred when the plan was re-optimized, with the constraints on the new structures contoured on the MR images. In this case the values obtained were slightly more limited; the PTV coverage differences were still about 0.5%, with D95 equal to -0.5%. The bladder and

femoral heads did not differ significantly from the values reported below, both in terms of D_{mean} and DVH constraints. The rectum instead showed lower values, with a mean dose difference of 4% and V40 and V50 lower than 8%.
However, this issue is not relevant in the implementation of the workflow, as only MRI acquisitions will be made for planning purposes. Rather, this behavior is representative of the differences in filling of different OARs, such as rectum and bladder, between one fraction and another of the treatment.
Moreover, the PTV and OARs compliance with the constraints, used in our center, was evaluated for the re-optimized plans on MRI, as reported in Table 16. For 7 patients and 8 different parameters, only 1 time over 56 the V40 of rectum exceeded the limits. So, this approach could be considered promising for a future implementation of adaptive radiotherapy [124].

4.4. Patient Setup Verification

The position shifts in the matching between CBCT and CT or MR images, and their differences, obtained manually through visual evaluation by three different radiation oncologists, are reported in Table 17 for selected fraction of different patients. The CT-based match was considered as the gold standard.
For 9 selected images of different fractions and patients, the shifts obtained through CT-CBCT registration, as described in the section 2.4, were compared to the those resulting from the evaluations of three radiation oncologists, who blindly matched the CBCT images with those from MRI. The mean shifts were 2.8±1.7 mm, 3.8±1.6 mm and 0.1±1.4 mm for transverse, longitudinal and vertical directions respectively. The obtained results were comparable with those presented in literature; Korhonen et al. [103], Wyatt et al. [104] and Doemer et al. [125] reported averaged shift values of a couple of millimeters.
In addition, the mean shifts of in-room verification positioning obtained by registration of CBCT-MR are compared with those of 20 patients previously treated using CBCT-CT match method, confirming differences of maximum 3 mm in all the directions.
Therefore, the accuracy of MR-CBCT matching method was assessed: despite the physiological differences of the rectum and bladder between the two imaging modalities, the average differences resulted approximately in a couple of millimeters, thus making this method suitable for in room verification.

4.5. Benefits and Drawbacks

Finally, the advantages and the critical aspects of the method proposed in this thesis are presented below, paying special attention to the applicability of this approach in a general hospital with similar characteristics to Niguarda.
The main benefit is certainly to plan on images with better contrast, also reducing the time and cost of a dual imaging modality. Another significant advantage is the automatic contouring process, which leads to lower variability in structures delineation and considerable time savings for the radiation oncologists.
On the other hand, there are several issues, both organizational and methodological, to be taken into account. First of all, a proper sequence has to be present on the MR scanner; a flat table, an

external laser system and suitable markers are also required for a correct acquisition, to ensure a reproducible daily setup. Besides, an additional slot on MR scanner dedicated to radiotherapy is mandatory. Hence, home-made or commercial software is needed to generate the sCT. Finally, adequate involvement and training of all staff, from medical physicists to radiation oncologists and technicians is fundamental.

As far as we are concerned, future developments will include the purchase of an MR safe external laser system and staff training gradually move to using MRI-only in the clinical routine of prostate district radiotherapy treatments. Meanwhile, the proposed method will be used for special cases, such as the one presented in the Addendum.

Afterwards a more ambitious future goal is to implement an MRI-only workflow also for other districts, such as the head and neck, where the improvement obtained using MR images (and automatic contouring) for planning purposes is evident.

CONCLUSIONS

The purpose of this work was to finalize the clinical implementation of MRI-Only radiotherapy treatment workflow for prostate cancer with a standard linac in a big general hospital. The resources available in Niguarda hospital were used in this work: a 1.5 T MRI-scanner (Magnetom Aera, Siemens Healthcare, Erlangen, Germany) and a standard linac (Synergy-S, Elekta AB, Stockholm, Sweden) were exploited.

In this thesis, which presented the development of a previous preliminary work, the whole process is described in terms of MR imaging acquisition, from imaging acquisition, passing through the collection of multi-atlases MR images to automatically implement the contouring process and thus generate the sCT useful for planning purposes, reaching the dosimetric validation of planning on sCT and ending with the verification of pre-treatment positioning by matching MR images with CBCT.

The 3D T1 VIBE Dixon gradient echo sequence used for this work is a good compromise between image quality and acquisition time; it takes 2 minutes and 30 seconds and provides 4 contrasts (Water, Fat, In-phase and Out-of-phase) useful for the visualization of target and different OARs. The acquisition on the MR scanner was possible thanks to the use of a self-made table-top, commercial MR safe markers and properly controlled internal laser system; furthermore, the geometric distortions, evaluated in the absence of the patient less than 2 mm, are minimized by the active shimming system of the scanner.

A hybrid method, which consists in a combination of bulk ED and multi atlas-based approach, was used to generate the synthetic CT (sCT) from MR images. For this purpose, the MR images of 20 volunteers and patients undergoing diagnostic acquisitions were collected, manually contoured and verified by a radiation oncologist, and then inserted in the database of ADMIRE software (research version 1.13.5, Elekta AB, Stockholm, Sweden), utilized for automatic contouring process. The delineation results, obtained in an average time of approximatively 20 minutes, are satisfactory, since the database was populated with a large number of individuals, with different ages and sizes. The achieved contoured images need further 5 to 10 minutes to better define some contours and to identify the target. These images are assigned a fixed ED for each structure, averaged over 20 patients in the RT database.

In order to accurately test the dose differences between the sCT and the gold standard CT, both in terms of homogeneous ED assignment and contours delineated on the MR images, different evaluations were made. At first, 20 VMAT prostate treatment plans, calculated on standard CT images with 10 MV X-rays, were copied using the same field arrangements and recalculated on the sCT. The mean deviation of PTV and OARs DVH parameters were approximately 0.5% and consistent with those reported in published papers, except the rectum were the percentage difference reached higher values (D_{mean} of 1% and V40 of 2.4%) due to different rectal filling. In addition, further evaluations were performed by 2D local γ-analysis with 10% of dose threshold in transverse, coronal and sagittal views. The average passing rate was from 98.5% and 99.4%, using an acceptance criterion of 2%-2mm.

Afterwards, the combination between the assignment of an average ED and the different contours in the two imaging modalities was evaluated for 7 patients underwent both to CT and MR acquisitions. The optimized plans, calculated on the CT images, were first copied using the same field arrangements and recalculated on the sCTs, obtained by MRI, and thus were optimized again

keeping the same plan constraints as CT-based ones. Despite the mean percentage differences in PTV coverage were limited, below the 1% in the first case and around 0.5% in the second one, the differences for OARs were considerably higher; mean percentage differences for bladder and femoral heads were approximatively -25% and -2% in both the described steps, while D_{mean} of rectum ranged from +11.5% to +4% and V40 passed from +26% to +8%.

Anyhow, this issue is not relevant in the implementation of the workflow, as only MRI acquisitions will be made for planning purposes. Rather, this behavior is representative of the differences in filling of different OARs, such as rectum and bladder, between two consecutive fractions of the treatment.

Moreover, however, the PTV and OARs compliance with the constraints, used in our center, was evaluated for the re-optimized plans: for 7 patients and 8 different parameters, only 1 time over 56 a constraint exceeded the limits.

Finally, the feasibility of in-room verification positioning using CBCT-MR matching was verified. For 9 selected images of different fractions and patients, the shifts obtained through CT-CBCT registration were compared to the those resulting from the evaluations of three radiation oncologists, who blindly and manually matched the CBCT images with those from MRI. The averaged differences in displacements between the two modalities resulted 2.8±1.7 mm, 3.8±1.6 mm and 0.1±1.4 mm for transverse, longitudinal and vertical directions respectively. Therefore, the accuracy of MR-CBCT matching method was assessed, despite the physiological differences of the rectum and bladder between the two imaging modalities.

The future goal is to gradually move to use of MRI-only in the clinical routine of prostate district radiotherapy treatments. Meanwhile, the proposed method will be used for special cases, such as the one presented in the Addendum.

REFERENCES

[1] *Chandarana H, Wang H, Tijssen R H N, Phil D, Das I J. Emerging Role of MRI in Radiation Therapy. J. Magn. Reson. Imaging. 2018;48:1468–1478. https://doi:10.1002/jmri.26271*

[2] *Karlsson M, Karlsson M G, Nyholm T, Amies C, Zackrisson B. Dedicated Magnetic Resonance Imaging in the Radiotherapy Clinic. Int. J. Radiat. Oncol. 2009;74(2): 644-651. https://doi:10.1016/j.ijrobp.2009.01.065*

[3] *Liney G, van der Heide U. MRI for Radiotherapy. Planning, Delivery and Response Assessment. Springer 2019 https://doi.org/10.1007/978-3-030-14442-5*

[4] *Menard C, van der Heide U. Introduction: Magnetic Resonance Imaging Comes of Age in Radiation Oncology. Semin. Radiat. Oncol. 2014;24(3):149-150. https://doi.org/10.1016/j.semradonc.2014.02.001*

[5] *Menard C, Paulson E, Nyholm T, McLaughlin P, Liney G, Dirix P, et al. Role of prostate MR imaging in radiation oncology. Radio.l Clin. North. Am. 2018;56:319–25. https://doi:10.1016/j.rcl.2017.10.012*

[6] *Rasch C, Barillot I, Remeijer P, Touw A, van Herk M, Lebesque JV. Definition of the prostate in CT and MRI: a multi-observer study. Int. J. Radiat. Oncol. Biol. Phys. 1999;43:57–66. https://doi:10.1016/s0360-3016(98)00351-4.*

[7] *Salembier C, Villeirs G, De Bari B, Hoskin P, Pieters BR, Van Vulpen M, et al. ESTRO ACROP consensus guideline on CT- and MRI-based target volume delineation for primary radiation therapy of localized prostate cancer. Radiother. Oncol. 2018;127:49–61. https://doi.org/10.1016/j.radonc.2018.01.014*

[8] *Villeirs G M, De Meerleer G O. Magnetic Resonance Imaging (MRI) anatomy of the prostate and application of MRI in radiotherapy planning. Eur. J. Radiol. 2007;63:361-368. https://doi:10.1016/j.ejrad.2007.06.030*

[9] *Torresin A, Brambilla M G, Monti A F, Moscato A, Brockmann M A, Schad L, Attenberger U I, Lohr F. Review of potential improvements using MRI in the radiotherapy workflow. Z. Med. Phys. 25 (2015) 210–2. http://dx.doi.org/10.1016/j.zemedi.2014.11.003*

[10] *Alongi F, Rigo M, Figlia V, Cuccia F, Giaj-Levra N, Nicosia L, Ricchetti F, Sicignano G, De Simone A, Naccarato S, Ruggieri R, Mazzola R. 1.5 T MR-guided and daily adapted SBRT for prostate cancer: feasibility, preliminary clinical tolerability, quality of life and patient-reported outcomes during treatment. Radiat. Oncol. 2020;15:69. https://doi.org/10.1186/s13014-020-01510-w*

[11] *Bird D, Henry A M, Sebag-Montefiore D, Buckley D L, Al-Qaisieh B, Speight R. A Systematic Review of the clinical Implementation of Pelvic Magnetic Resonance Imaging-Only Planning for External Beam Radiation Therapy. Int. J. Radiat. Oncol. Biol. Phys. 2019;105(3):479-492. https://doi.org/10.1016/j.ijrobp.2019.06.2530*

[12] *Christiansen R L, Jensen H, Brink C. Magnetic resonance only workflow and validation of dose calculations for radiotherapy of prostate cancer. Acta Oncol. 2017;56(6):787-791. http://dx.doi.org/10.1080/0284186X.2017.1290275.*

[13] *Corradini S. Alongi F, Andratschke N, Belka C, Boldrini L, Cellini F, Debus J, Guckenberg M, Horner-Rieber J, Lagerwaard F J, Mazzola R, Palacios M A, Philippens M E P, Raaijmakers C P J, Terhaard C H J, Valentini V, Niyazi M. MR-guidance in clinical reality: current treatment challenges and future perspectives. Radiat. Oncol. 2019;14:92. https://doi.org/10.1186/s13014-019-1308-y.*

[14] *Greer P, Martin J, Sidhom M, Hunter P, Pichler P, Choi J H, Best L, Smart J, Young T, Jameson M, Afinidad T, Wratten C, Denham J, Holloway L, Sridharan S, Rai R, Liney G, Raniga P, Dowling J. A Multi-center Prospective Study for Implementation of an MRI-Only Prostate Treatment Planning Workflow. Front. Oncol. 2019;9:826. http://doi:10.3389/fonc.2019.00826*

[15] *Johnstone R, Guerrero-Urbano T, Michaleidou A, Greener T, Miles E, Eaton D, Thomas C. Guidance on the use of MRI for treatment planning in radiotherapy clinical trials. Br. J. Radiol. 2020; 93: 20190161. https://doi org/10.1259/bjr.20190161.*

[16] *Kemppainen R, Suilamo S, Tuokkola T, Lindholm P, Deppe M H, Keyrilainen J. Magnetic resonance-only simulation and dose calculation in external beam radiation therapy: a feasibility study for pelvic cancers. Acta Oncol. 2017;56(6):792-798. https://doi.org/10.1080/0284186X.2017.1293290.*

[17] *Kapanen M, Collan J, Beule A, Seppala T, Saarilahti K, Tenhunen M. Commissioning of MRI-only based treatment planning procedure for external beam radiotherapy of prostate. Magn. Reson. Med. 2013;70:127–35. https://doi:10.1002/mrm.24459.*

[18] *Kerkmeijer L G W, Maspero M, Meijer G J, van der Voort van Zyp J R N, de Boer H C J, van den Berg C A T. Magnetic Resonance Imaging only Workflow for Radiotherapy Simulation and Planning in Prostate Cancer. J. Clin. Oncol. 2018;30:692-701. https://doi.org/10.1016/j.clon.2018.08.009.*

[19] *Lagendijk JJ, Raaymakers BW, van Vulpen M. The magnetic resonance imaging-linac system. Semin. Radiat. Oncol. 2014; 24:207-209. http://dx.doi.org/10.1016/j.semradonc.2014.02.009*

[20] *Nyholm T, Jonsson J. Counterpoint: Opportunities and Challenges of a Magnetic Resonance Imaging-Only Radiotherapy Work Flow. Semin. Radiat. Oncol. 2014 24:175-180. http://dx.doi.org/10.1016/j.semradonc.2014.02.005*

[21] *Owrangi A M, Greer P B, Glide-Hurst C K. MRI-only treatment planning: benefits and challenges. Phys. Med. Biol. 2018;63:1-15. https://doi.org/10.1088/1361-6560/aaaca4*

[22] *Persson E, Gustafsson C, Nordstrom F, Sohlin M, Gunnlaugsson A, Petruson K, et al. MR-OPERA: a multicenter/multivendor validation of magnetic resonance imaging only prostate treatment planning using synthetic computed tomography images. Int. J. Radiat. Oncol. Biol. Phys. 2017;99:692–700. https://doi:10.1016/j.ijrobp.2017.06.006.*

[23] *Persson E, Gustafsson C J, Ambolt P, Engelholm S, Ceberg S, Back S, Olsson L E, Gunnlaugsson A. MR-PROTECT: Clinical feasibility of a prostate MRI-only radiotherapy treatment workflow and*

investigation of acceptance criteria. Radiat. Oncol. 2020;15:77. https://doi.org/10.1186/s13014-020-01513-7.

[24] *Schmidt M A, Payne G S. Radiotherapy Planning using MRI. Phys. Med. Biol. 2015;60(22):R323-R361. https://doi:10.1088/0031-9155/60/22/R323*

[25] *Tyagi N, Fontenla S, Zelefsky M, Chon-Ton M, Ostergren K, Shah N, Warner L, Kadbi M, Mechalakos J, Hunt M. Clinical workflow for MR-only simulation and planning in prostate. Radiat. Oncol. 2017;12:119. https://doi:10.1186/s13014-017-0854-4*

[26] *Rasch C, Steenbakkers R, van Herk M. Target Definition in Prostate, Head, and Neck. Semin. Radiat. Oncol. 2005;15:136–45. https://doi:10.1016/j.semradonc.2005.01.005.*

[27] *Associazione Italiana di Oncologia Medica (AIOM), Associazione Italiana Registri Tumori (AIRTUM). I numeri del cancro in Italia 2019. 2019. Intermedia Editore.*

[28] *Cattaneo G M, Reni M, Rizzo G, Castellone P, Ceresoli G L, Cozzarini C, Ferreri A J M, Passoni P, Calandrino R. Target delineation in post-operative radiotherapy of brain gliomas: interobserver variability and impact of image registration of MR (pre-operative) images on treatment planning CT scans. Radiother. Oncol. 2005; 75:217-23. https://doi.org/10.1016/j.radonc.2005.03.012*

[29] *Debois M, Oyen R, Maes F, Verswijvel G, Gatti G, Bosmans H, Feron M, Bellon E, Kutcher G, Van Poppel H, Vanuystel L. The contribution of magnetic resonance imaging to the three-dimensional treatment planning of localized prostate cancer. Int. J. Radiat. Oncol. Biol. Phys. 1999;45(4):857-865. https://doi:10.1016/s0360-3016(99)00288-6*

[30] *Njeh CF. Tumor delineation: The weakest link in the search for accuracy in radiotherapy. J. Med. Phys. 2008;33(4):136–40. https://doi.org/10.4103/ 0971-6203.44472*

[31] *Nyholm, T, Nyberg M, Karlsson M G, Karlsson M. Systematization of spatial uncertainties for comparison between a MR and a CT-based radiotherapy work- flow for prostate treatments. Radiat. Oncol. 2009;54(4):1–9. https://doi.org/10.1186/1748-717X-4-54*

[32] *Parker CC, Damyanovich A, Haycocks T, Haider M, Bayley A, Catton C N. Magnetic resonance imaging in the radiation treatment planning of localized prostate cancer using intra-prostatic fiducial markers for computed tomography co-registration. Radiother. Oncol. 2003;66(2):217-224. https://doi:10.1016/s0167-8140(02)00407-3.*

[33] *Roach M 3rd, Faillace-Akazawa P, Malfatti C, Holland J, Hricak H. Prostate volumes defined by magnetic resonance imaging and computerized tomographic scans for three dimensional conformal radiotherapy. Int. J. Radiat. Oncol. Biol. Phys. 1996;35(5):1011-1018. https://doi:10.1016/0360-3016(96)00232-5.*

[34] *Gunnlaugsson A, Persson E, Gustafsson C, Kjellen E, Ambolt P, Engelholm S, Nilsson P, Olsson L E. Target definition in radiotherapy of prostate cancer using magnetic resonance imaging only workflow. phiRO. 2019;9:89-91. https://doi.org/10.1016/j.phro.2019.03.004*

[35] *Sande L, Langkilde N C, Holmberg M, Carl J. MRI target delineation may reduce long-term toxicity after prostate radiotherapy. Acta Oncol. 2014;53(6):809-814. https://doi.org/10.3109/0284186X.2013.865077*

[36] *Smith W L, Lewis C, Bauman G, Rodrigues G, D'souza D, Ash R, Ho D, Venkatesan V, Downey D, Fenster A. Prostate volume contouring: a 3D analysis of segmentation using 3DTRUS, CT, and MR. Int. J. Radiat. Oncol. Biol. Phys. 2007;67(4):1238-1247. https://doi.org/10.1016/j.ijrobp.2006.11.027*

[37] *Tzikas A, Karaiskos P, Papanikolaou N, Sandilos P, Koutsouveli E, Lavdas E, Scarleas C, Dardoufas K, Lind B K, Mavroidis P. Investigating the clinical aspects of using CT vs. CT-MRI images during organ delineation and treatment planning in prostate cancer radiotherapy. Technol. Cancer. Res. Treat. 2011;10(3):231-242. https://doi:10.7785/tcrt.2012.500198*

[38] *Roberson P L, McLaughlin P W, Narayana V, Troyer S, Hixson G V, Kessler M L. Use and uncertainties of mutual information for computed tomography/magnetic resonance (CT/MR) registration post permanent implant of the prostate. Med. Phys. 2005;32(2): 473-482. https://doi:10.1118/1.1851920*

[39] *Edmund JM, Nyholm T. A review of substitute CT generation for MRI-only radiation therapy. Radiat. Oncol. 2017;12:28–43. https://doi.org/10.1186/s13014-016-0747-y*

[40] *Tenhunen M, Korhonen J, Kapanen M, Seppala T, Koivula L, Collan J, Saarilahti K, Visapaa H. MRI-only based radiation therapy of prostate cancer: workflow and early clinical experience. Acta Oncol. 2018;57(7):902-907. https://doi.org/10.1080/0284186X.2018.1445284*

[41] https://www.usa.philips.com/healthcare/education-resources/publications/fieldstrength/mri-in-prostate-cancer

[42] *Guerreiro F, Burgos N, Dunlop A, Wong K, Petkar I, Nutting C, Harrington K, Bhide S, Newbold K, Dearnaley D, deSouza N M, Morgan V A, McClelland J, Nill S, Cardoso M J, Ourselin S, Oelfke U, Knopf A C. Evaluation of a multi-atlas CT synthesis approach for MRI-only radiotherapy treatment planning. Phys. Med. 2017;35:7-17. http://dx.doi.org/10.1016/j.ejmp.2017.02.017*

[43] *Keesman R, van de Lindt T N, Juan-Cruz C, van den Wollenberg W, van der Bijl E, Nowee M E, Sonke J-J, van der Heide U A, Fast M F. Correcting geometric image distortion in slice-based 4D-MRI on the MR-linac. Med. Phys. 2019;46(7):3044-3054. https://doi.org/ 10.1002/mp.13602*

[44] *Kemppainen R, Vaara T, Joensuu T, Kiljunen T. Accuracy and precision of patient positioning for pelvic MR-only radiation therapy using digitally reconstructed radiographs. Phys. Med. Biol. 2018;63(5):055009. https://doi.org/10.1088/1361-6560/aaad21*

[45] *Kim J, Garbarino K, Schultz L, Levin K, Movsas B, Siddiqui M S, Chetty I J, Glide-Hurst C. Dosimetric evaluation of synthetic CT relative to bulk density assignment-based magnetic resonance-only approaches for prostate radiotherapy. Radiat. Oncol. 2015;10:239. https://doi:10.1186/s13014-015-0549-7*

[46] *Torfeh T, Hammoud R, Perkins G, McGarry M, Aouadi S, Celik A, Hwang K-P, Stancanello J, Petric P, Al-Hammadi N. Characterization of 3D geometric distortion of magnetic resonance imaging scanners commissioned for radiation therapy planning. Magn. Reson. Imaging. 2016;34:645-653. http://dx.doi.org/10.1016/j.mri.2016.01.001*

[47] *Kim J, Miller B, Siddiqui S, Movsas B, Glide-Hurst C. FMEA of MR-Only Treatment Planning in the Pelvis. Pract. Radiat. Oncol. 2019;4:168-176. https://doi.org/10.1016/j.adro.2018.08.024*

[48] *Maspero M, Seevinck P R, Schubert G, Hoesl M A U, van Asselen B, Viergever M A, Lagendijk J J W, Meijer G J, van der Berg C A T. Quantification of confounding factors in MRI-based dose calculations as applied to prostate IMRT. Phys. Med. Biol. 2017;62:948-965. https://doi:10.1088/1361-6560/aa4fe7*

[49] *Dowling J A, Sun J, Pichler P, Rivest-Henault D, Ghose S, Richardson H, Wratten C, Martin J, Arm J, Best L, Chandra S S, Fripp J, Menk F W, Greer P B. Automatic Substitute Computed Tomography Generation and Contouring for Magnetic Resonance Imaging (MRI)-Alone External Beam Radiation Therapy From Standard MRI Sequences. Int. J. Radiat. Oncol. Biol. Phys. 2015;93(5):1144-1153. http://dx.doi.org/10.1016/j.ijrobp.2015.08.045*

[50] *Eggers H, Brendel B, Duijndam A, Herigault G. Dual-echo Dixon imaging with flexible choice of echo times. Magn. Reson. Med. 2011;65(1):96–107. https://doi:10.1002/mrm.22578*

[51] *Paulson E S, Erickson B, Schultz C, Li A. Comprehensive MRI simulation methodology using a dedicated MRI scanner in radiation oncology for external beam radiation treatment planning. Med. Phys. 2015;42(1):28-39. http://dx.doi.org/10.1118/1.4896096*

[52] *Kapanen M, Tenhunen M. T1/T2*-weighted MRI provides clinically relevant pseudo-CT density data for the pelvic bones in MRI-only based radiotherapy treatment planning. Acta Oncol. 2013; 52:612-18. https://doi:10.3109/0284186X.2012.692883.*

[53] *Korhonen J, Kapanen M. Absorbed doses behind bones with MR image-based dose calculations for radiotherapy treatment planning. Med. Phys. 2013;40(1):011701. http://dx.doi.org.pros.lib.unimi.it/10.1118/1.4769407*

[54] *Korhonen J, Kapanen M, Keyriläinen J, Seppälä T, Tenhunen M. A dual model HU conversion from MRI intensity values within and outside of bone segment for MRI-based radiotherapy treatment planning of prostate cancer. Med. Phys. 2014;41(1):011704-1-12. https://doi:10.1118/1.4842575.*

[55] *Rahmer J, Blume U, Bornert P. Selective 3D ultrashort TE imaging: comparison of "dual-echo acquisition and magnetization preparation for improving short-T 2 contrast. MAGMA. 2007; 20(2):83–92. https://doi: 10.1007/s10334-007-0070-6.*

[56] *Robson MD, Gatehouse PD, Bydder M, Bydder GM. Magnetic resonance: An introduction to ultrashort TE (UTE) imaging. J. Comput. Assist. Tomogr. 2003;27:825–46. https://doi:10.1097/00004728-200311000-00001.*

[57] *Dixon W T. Simple proton spectroscopic imaging. Radiology. 1984;153(1):189–94. https://doi:10.1148/radiology.153.1.6089263.*

[58] *Guerini H, Omoumi P, Guichoux F, Vuillemin V, Morvan G, Zins M, Thevenin F, Drape JL. Fat Suppression with Dixon Techniques in Musculoskeletal Magnetic Resonance Imaging: A Pictorial Review. Semin. Musculoskelet.. Radiol. 2015;19:335–347. http://dx.doi.org/10.1055/s-0035-1565913.*

[59] *Wyatt J J, Dowling J A, Kelly C G, McKenna J, Johnstone E, Speight R, Henry A, Greer P B, McCallum H M. Investigating the generalization of an atlas-based synthetic-CT algorithm to*

another centre and MR scanner for prostate MR-only radiotherapy. Phys. Med. Biol. 2017;62:N548-N560. https://doi.org/10.1088/1361-6560/aa9676

[60] *Gladwish A, Pang G, Cheung P, D'Alimonte L, Deabreu A, Loblaw A. Prostatic displacement during extreme hypofractionated radiotherapy using volumetric modulated arc therapy (VMAT). Radiat. Oncol. 2014;9, 262. https://doi.org/10.1186/s13014-014-0262-y*

[61] *Steenbakkers R J H M, Duppen J C, Betgen A, Lotz H T. Impact of knee support and shape of tabletop on rectum and prostate position. Int. J. Radiat. Oncol. Biol. Phys. 2005;60(5):1364-1372. https://doi: 10.1016/j.ijrobp.2004.05.060*

[62] *Sun J, Downling J A, Pichler P, Parker J, Martin J, Stanwell P, Arm J, Menk F, Greer P B. Investigation on the performance of dedicated radiotherapy positioning devices for MR scanning for prostate planning. J. Appl. Clin. Med. Phys. 2015;16(2):4-13. https://doi:10.1120/jacmp.v16i2.4848*

[63] *Walker A, Liney G, Metcalfe P, Holloway L. MRI distortion: considerations for MRI based radiotherapy treatment planning. Australas. Phys. Eng. Sci. Med. 2014;37:103-13. https://doi: 10.1007/s13246-014-0252-2.*

[64] *Wang D, Doddrell D M, Cowin G. A novel phantom and method for comprehensive 3-dimensional measurement and correction of geometric distortion in magnetic resonance imaging. Magn. Reson. Imaging. 2004;22:529-542. https://doi:10.1016/j.mri.2004.01.008*

[65] *Gustafsson C, Nordstrom F, Persson E, Brynolfsson J, Olsson LE. Assessment of dosimetric impact of system specific geometric distortion in an MRI only based radiotherapy workflow for prostate. Phys. Med. Biol. 2017;62:2976–2989. https://doi:10.1088/1361-6560/aa5fa2.*

[66] *Blasche M, Fischer D, Healthineers S. Magnet Homogeneity and Shimming. MReadings: MR in RT. Siemens White paper. 2017:3.*

[67] *Stanescu T, Wachowicz K, Jaffray DA. Characterization of tissue magnetic susceptibility-induced distortions for MRIgRT. Med. Phys. 2012;39(12):7185–93. https://doi:10.1118/1.4764481*

[68] *Adjeiwaah M, Bylund M, Lundman J A, Karlsson C T, Jonsson J H, Nyholm T. Quantifying the Effect of 3T Magnetic Resonance Imaging Residual System Distortions and Patient-Induced Susceptibility Distortions on Radiation Therapy Treatment Planning for Prostate Cancer. Int. J. Radiat. Oncol. Biol. Phys. 2018;100:317-324. https://doi.org/10.1016/j.ijrobp.2017.10.021*

[69] *Wyatt J, Hedley S, Johnstone E, Speight R, Kelly C, Henry A, Short S, Murray L, Sebag-Montefiore D, McCallum H. Evaluating the repetibility and set-up sensitivity of a large field of view distortion phantom and software for magnetic resonance-only radiotherapy. phiRO 2018;6: 31–38. https://doi.org/10.1016/j.phro.2018.04.005*

[*70] Ranta I, Kemppainen R, Keyrilainen J, Suilamo S, Heikkinen S, Kapanen M, Saunavaara J. Quality assurance measurements of geometric accuracy for magnetic resonance imaging-based radiotherapy treatment planning. Phys. Med. 2019;62:47-52. https://doi.org/10.1016/j.ejmp.2019.04.022*

[71] *Cunningham J M, Barberi E A, Miller J, Kim J P, Glide-Hurst C K. Development and evaluation of a novel MR-compatible pelvic end-to-end phantom. J. Appl. Clin. Med. Phys. 2019;20(1):265-275. https://doi:10.1002/acm2.12455*

[72] *Huang K C, Cao Y, Baharom U, Balter J M. Phantom-based characterization of distortion on a magnetic resonance imaging simulator for radiation oncology. Phys. Med. Biol. 2016;61(2):774–790. https://doi:10.1088/0031-9155/61/2/774*

[73] *Price R G, Knight R A, Hwang K-P, Bayram E, Nejad-Davarani S P, Glide-Hurst C K. Optimization of a novel large field of view distortion phantom for MR-only treatment planning. J. Appl. Clin. Med. Phys. 2017;18(4):51 ‑61. https://doi:10.1002/acm2.12090*

[74] *Sun J, Dowling J, Pichler P, Menk F, Rivest-Henault D, Lambert J, Parker J, Arm J, Best L, Martin J, Denham J W, Greer P B. MRI simulation: end-to-end testing for prostate radiation therapy using geometric pelvic MRI phantoms. Phys. Med. Biol. 2015;60:3097-3109. https:// doi:10.1088/0031-9155/60/8/3097*

[75] *Walker A, Liney G, Holloway L, Dowling J, Rivest-Henault D, Metcalfe P. Continuous table acquisition MRI for radiotherapy treatment planning: Distortion assessment with a new extended 3D volumetric phantom. Med. Phys. 2015;42(4):1982-1991. http://dx.doi.org/10.1118/1.4915920*

[76] *Andreasen D, Van Leemput K, Hansen RH, Andersen JA, Edmund JM. Patch-based generation of a pseudo CT from conventional MRI sequences for MRI-only radiotherapy of the brain. Med. Phys. 2015; 42:1596–605. https://doi: 10.1118/1.4914158.*

[77] *Chin A L, Lin A, Anamalayil S, Teo B-K K. Feasibility and limitations of bulk density assignment in MRI for head and neck IMRT treatment planning. J. Appl. Clin. Med. Phys. 2014;15(5):100-111. https:// 10.1120/jacmp.v15i5.4851*

[78] *Johnstone, E, Wyatt J J, Henry A M, Short S C, Sebag-Montefiore D, Murray L, Kelly C G, Mccallum H M, Speight R. Systematic Review of Synthetic Computed Tomography Generation Methodologies for Use in Magnetic Resonanc Imaging-Only Radiation Therapy. Int. J. Radiat. Oncol. Biol. Phys. 2018;100:199-217. https://doi:10.1016/j.ijrobp.2017.08.043.*

[79] *Largent A, Barateau A, Nunes J-C, Lafond C, Greer P B, Dowling J A, Saint-Jalmes H, Acosta O, de Crevoisier R. Pseudo-CT generation for MRI-only radiotherapy treatment planning: comparison between patch-based, atlas-based and bulk density methods. Radiat. Oncol. 2018. https://doi.org/10.1016/j.ijrobp.2018.10.002.*

[80] *Leu S C, Huang Z, Lin Z. Generation of Pseudo-CT using High-Degree Polynomial Regression on Dual-Contrast Pelvic MRI Data. Nature. 2020;10:8118. https://doi.org/10.1038/s41598-020-64842-3*

[81] *Maspero M, Savenije M H F, Dinkla A M, Seevinck P R, Intven M P W, Jurgenliemk-Schulz I M, Kerkmeijer L G W, van den Berg C A T. fast synthetic-CT generation using a generative adversial network for general pelvis MR-only radiotherapy. Phys. Med. Biol. 2018;63(18):185001. https://doi: 10.1088/1361-6560/aada6d.*

[82] *Savenije M H F, Maspero M, Sikkes G G, van der Voort van Zyp J R N, Kotte A N T J, Bol G H, van den Berg C A T. Clinical implementation of MRI-based organs-at-risk auto-segmentation with convolutional networks for prostate radiotherapy. Radiat. Oncol. 2020;15:104. https://doi.org/10.1186/s13014-020-01528-0*

[83] *Shafai-Erfani G, Wang T, Lei Y, Tian S, Patel P, Jani A B, Curran W J, Liu T, Yang X. Dose evaluation of MRI-based synthetic CT generated using a machine learning method for prostate cancer radiotherapy. Med. Dosim. 2019;44:e64-e70. https://doi.org/10.1016/j.meddos.2019.01.002*

[84] *Siversson C, Nordstrom F, Nilsson T, Nyholm T, Jonsson J, Gunnlaugsson A, et al. Technical Note: MRI only prostate radiotherapy planning using the statistical decomposition algorithm. Med. Phys. 2015;42:6090–7. https://doi:10.1118/1.4931417*

[85] *Tyagi N, Fontenla S, Zhang J, Cloutier M, Kadbi M, Mechalakos J, et al. Dosimetric and workflow evaluation of first commercial synthetic CT software for clinical use in pelvis. Phys. Med. Biol. 2017;62:2961–75. https://doi:10.1088/1361-6560/aa5452*

[86] *Chen L L, Price R A, Wang L, Li J, Qin L H, McNeeley S, Freedman G M, Pollack A. MRI-based treatment planning for radiotherapy: Dosimetric verification for prostate IMRT. Int. J. Radiat. Oncol. Biol. Phys. 2004: 60(2):636-47. https://doi:10.1016/j.ijrobp.2004.05.068*

[87] *Lee Y K, Bollet M, Charles-Edwards G, Flower M A, Leach M O, Mcnair H, Moore E, Rowbottom C, Webb S. Radiotherapy treatment planning of prostate cancer using magnetic resonance imaging alone. Radiother. Oncol. 2003;66:203-216. https://doi:10.1016/s0167-8140(02)00440-1*

[88] *Greer P B, Dowling J A, Lambert J A, Fripp J, Parker J, Denham J W, Wratten C, Capp A, Salvado O. A magnetic resonance imaging-based workflow for planning radiation therapy for prostate cancer. Med. J. Australia. 2011;194(4):24-27. https://doi:10.5694/j.1326-5377.2011.tb02939.x*

[89] *Lambert J, Greer P B, Menk F, Patterson J, Parker J, Dahl K, Gupta S, Capp A, Wratten C, Tang C, Kumar M, Dowling J, Hauville S, Hughes C, Fisher K, Lau P, Denham J W, Salvado O. MRI-guided prostate radiation therapy planning: Investigation of dosimetric accuracy of MRI-based dose planning. Radiother. Oncol. 2011;98:330-4. https://doi:10.1016/j.radonc.2011.01.012*

[90] *ICRU 1992. ICRU Report n.46. Photon, Electron, Proton and Neutron Interaction Data for Body Tissues.*

[91] *Edmund J M, Kjer H M, Van Leemput K, Hansen R H, Andersen J A L, Andreasen D. A voxel-based investigation for MRI-only radiotherapy of the brain using ultra short echo times. Phys. Med. Biol. 2014;59:7501–7519. https://doi:10.1088/0031-9155/59/23/7501*

[92] *Johansson A, Karlsson M, Nyholm T. CT substitute derived from MRI sequences with ultrashort echo time. Med. Phys. 2011; 38:2708-2714. https://doi:10.1118/1.3578928.*

[93] *Andreasen D, Van Leemput K, Edmund J M. A patch-based pseudo- CT approach for MRI-only radiotherapy in the pelvis. Med Phys 2016; 43:4742. https://doi:10.1118/1.4958676*

[94] *Dowling J A, Lambert J, Parker J, Salvado O, Fripp J, Capp A, Wratten C, Denham J W, Greer P B. An atlas-based electron density mapping method for magnetic resonance imaging (MRI)-*

alone treatment planning and adaptive MRI-based prostate radiation therapy. Int. J. Radiat. Oncol. Biol. Phys. 2012;83(1):E5–E11. https://doi:10.1016/j.ijrobp.2011.11.056.

[95] *Sjolund J, Forsberg D, Andersson M, Knutsson H. Generating patient specific pseudo-CT of the head from MR using atlas-based regression. Phys. Med. Biol. 2015 60:825–39. https://doi:10.1088/0031-9155/60/2/825*

[96] *Gudur M S R, Hara W, Le Q T, Wang L, Xing L, Li R J. A unifying probabilistic Bayesian approach to derive electron density from MRI for radiation therapy treatment planning. Phys. Med. Biol. 2014;59:6595–6606. https://doi:10.1088/0031-9155/59/21/6595*

[97] *Chen S, Qin A, Zhou D, Yan D. Technical Note: U-net-generated synthetic CT images for magnetic resonance imaging-only prostate intensity-modulated radiation therapy treatment planning. Med. Phys. 2018;45(12):5659-5665. https://doi.org/10.1002/mp.13247*

[98] Han X*. MR-based synthetic CT generation using a deep convolutional neural network method. Med. Phys. 2017;44(4):1408-1419. https://doi-org.pros.lib.unimi.it/10.1002/mp.12155]*

[99] *Arabi H, Dowling J A, Burgos N, Han X, Greer P B, Koutsouvelis N, Zaidi H. Comparative study of algorithms for synthetic CT generation from MRI: Consequences for MRI-guided radiation planning in the pelvic region. Med. Phys. 2018;45:5218-5233. https://doiorg.pros.lib.unimi.it/10.1002/mp.13187*

[100] *Köhler MVT, Grootel MV, Hoogeveen R, Kemppainen R, Renisch S. MR-only simulation for radiotherapy planning. Philips White paper. 2015.*

[101] *Low D A, Harms W B, Mutic S, Purdy J A. A technique for the quantitative evaluation of dose distributions. Med. Phys. 1998;25(5):656-661. https://doi-org.pros.lib.unimi.it/10.1118/1.598248*

[102] *Ezzell G A, Burmeister J W, Dogan N, LoSasso T J, Mechalakos JG, Mihailidis D, Molineu A, Palta J R, Ramsey C R, Salter B J. IMRT commissioning: Multiple institution planning and dosimetry comparisons, a report from AAPM Task Group 119. Med. Phys. 2009;36(11):5359–5373. https://doi-org.pros.lib.unimi.it/10.1118/1.3238104*

[103] *Korhonen J, Kapanen M, Sonke J-J, Wee L, Salli E, Keyrilainen J, Seppala T, Tenhuenen M. Feasibility of MRI-based reference images for image-guided radiotherapy of the pelvis with either cone-beam computed tomography or planar localization images. Acta Oncol. 2015;54:889-895. https:// DOI: 10.3109/0284186X.2014.958197*

[104] *Wyatt J J, Brooks R L, Ainslie D, Wilkins E, Raven E, Pilling K, Pearson R A, McCallum H M. The accuracy of Magnetic Resonance – Cone Beam Computed Tomography soft-tissue matching for prostate radiotherapy. phiRO. 2019;12:49-55. https://doi.org/10.1016/j.phro.2019.11.005*

[105] *Nici S (2019). MRI-only in prostate radiotherapy planning using multiple individual atlases: a preliminary study on a 1.5 T scanner. Scuola di Specializzazione in Fisica Medica, Milano.*

[106] Nici S, Monti A F, Lizio D, Pellegrini R, Brambilla M G, Carbonini C, Arias Garces M J, Felisi M M J, Bortolato B, Frassica C, Coletti C, Vanzulli A, Torresin A. MRI-only in prostate radiotherapy planning using multiple individual atlates: a preliminary study. ESTRO 2020. PH-0412.

[107] Mutic S, Palta J R, Butker E K, Das I J, Huq M S, Dick Loo L-N, Salter B J, McCollough C H, Van Dyk J. Quality assurance for computed-tomography simulators and the computedtomography-simulation process: Report of the AAPM Radiation Therapy Committee Task Group No. 66. Med. Phys. 2003;30(10):2762–2792. https://doi: 10.1118/1.1609271

[108] AAPM. AAPM report no. 100: Acceptance testing and quality assurance procedures for magnetic resonance imaging facilities. Alexandria, VA: AAPM; 2010.

[109] ACR. MRI quality control manual. Reston, VA: ACR; 2015.

[110] Santoni R, Arcangeli S, Ingrosso G, Antognoni P, Mazzeo E, D'angelillo RM, Buglione M, Borghesi S, Petitti T, Orecchia R. Linee guida Carcinoma della Prostata – AIRO, 2016. Tumori J 2016; 102: S1-S79.https://doi.org/10.5301/TJ.2016.15934

[111] Van der Velde J, Wouters J, Vercauteren T, De Gersem W, Achten E, De Neve Wilfried, Van Hoof T. Optimal number of atlases and label fusion for automatic multi-altas based brachial plexus contouring in radiotherapy treatment planning. Radiat. Oncol. 2016;11:1. https:// DOI 10.1186/s13014-015-0579-1

[112] Rohlfing T, Brandt R, Menzel R, Russakoff D B, Maurer C R. Quo vadis, atlas-based segmentation?. In Handbook of biomedical image analysis. 2005; 435-86. Springer.

[113] Warfield S K, Zou K H, Wells W M. Simultaneous truth and performance level estimation (STAPLE): an algorithm for the validation of image segmentation. IEEE transactions on medical imaging. 2004;23(7):903-21. https://doi:10.1109/TMI.2004.828354.

[114] Warfield S K, Zou K H, Wells W M. Validation of image segmentation by estimating rater bias and variance. Philos. Trans. A. Math. Phys. Eng. Sci. 2008;366(1874):2361–75. https:// doi: 10.1098/rsta.2008.0040

[115] Han X, Elekta AB. A Locally Adaptive, Intensity-Based Label Fusion Method for Multi-Atlas Auto-Segmentation. MO: Maryland Heights; 2012.

[116] Coupe P, Manjon J V, Fonov V, Pruessner J, Robles M, Collins D L. Patch-based segmentation using expert priors: Application to hippocampus and ventricle segmentation. Neuroimage. 2011;54(2):940–954. https://doi:10.1016/j.neuroimage.2010.09.018.

[117] Viola P, Wells W M. Alignment by maximization of mutual information. Int. J. Comput. Vis. 1997;24(2):137-154. https://doi.org/10.1023/A:1007958904918

[118] Arsigny V, Commowick O, Ayache N, Pennec X. A Log-Euclidean Polyaffine Framework for Locally Rigid or Affine Registration. Biomedical Image Registration. WBIR 2006. Lecture Notes in Computer Science, vol 4057. Springer, Berlin, Heidelberg. https://doi.org/10.1007/11784012_15

[119] ABAS: Intra-Patient Deformable Image Registration for Adaptive Radiotherapy – A White Paper. CMS Software, Elekta Inc.

[120] ICRU 2010. ICRU Report n.83. Prescribing, Recording, and Reporting Photon-beam Intensity-modulated Radiation Therapy (IMRT).

[121] Stroom J C, Kroonwijk M, Pasma K L, Koper P C, Van Dieren E B, Heijmen B J. Detection of internal organ movement in prostate cancer patients using portal images. Med. Phys. 2000;27: 452-461. https://doi.org/10.1118/1.598913

[122] Weygand J, Fuller C D, Ibbott G S, Mohamed A S R, Ding Y, Yang J, Hwang K-P Wang J. Spatial Precision in Magnetic Resonance Imaging-Guided Radiation Therapy: The Role of Geometric Distortions. Int. J. Radiat. Oncol. Biol. Phys. 2016;95(4):1304-1316. http://dx.doi.org/10.1016/j.ijrobp.2016.02.059

[123] Korsholm M E, Waring L W, Edmund J M. A criterion for the reliable use of MRI-only radiotherapy. Radiat. Oncol. 2014;9:16. http://www.ro-journal.com/content/9/1/16

[124] Tetar S U, Bruynzeel A M E, Lagerwaard F J, Slotman B J, Bohoudi O, Palacios M A. Clinical implementation of magnetic resonance imaging guided adaptive radiotherapy for localized prostate cancer. phiRO. 2019;9:69-76. https://doi.org/10.1016/j.phro.2019.02.002

[125] Doemer A, Chetty I J, Glide-Hurst C, Nurushev T, Hearshen D, Pantelic M, Traughber M, Kim J, Levin K, Elshaikh M A, Walker E, Movsas B. Evaluating organ delineation, dose calculation and daily localization in an open-MRI simulation workflow for prostate cancer patients. Radiat. Oncol. 2015;10(1):37. https://DOI:10.1186/s13014-014-0309-0

ADDENDUM

MRI-only in a prostate cancer patient with bilateral metal hip prostheses: a case study

ABSTRACT

Outline of a practical method to perform prostate cancer radiotherapy in patients with bilateral metal hip prostheses. The proposed workflow is based exclusively on MRI-imaging, which replaces CT, useless due to relevant artifacts. The resulting VMAT plan leads to target homogeneous coverage, sparing both organs at risk and prostheses.

BACKGROUND AND AIM

As the population ages, the number of patients with hip replacements undergoing external beam radiotherapy treatment (EBRT) for the prostate cancer is expected to increase. The incidence of prostate cancer increases significantly from the age of 60 years onwards and hip replacement surgery grows in this age group too [1, 2].

Metallic implants are challenging in radiotherapy treatment planning, mainly for two reasons: image artifacts in planning-CT images, which make difficult or impossible to delineate target and organs at risks (OARs) and high inaccuracy in the dosimetric outcome arising from the inability to predict tissue electron densities (ED).

In the prostatic region this behavior is particularly relevant: dose attenuation through the metal hip prosthesis can drastically change the dose uniformity in the target, also producing local dose perturbations at the hip interface, especially in Treatment Planning Systems (TPS) with older algorithms [3, 4, 5, 6, 7].

For single hip prosthesis, image artifacts are usually not too much severe and allow a reasonable definition of target volumes [5]. Besides, a treatment plan setup that avoids the beam entrance through the metallic device is also achievable [6].

When bilateral hip prostheses (b-HP) are present, the artefacts can make CT images useless for target definition, particularly for prostate tumor, where it is already difficult to identify the apex of the prostate or the prostatic lodge after surgery. Several different solutions are proposed in literature, as MVCT performed on TomoTherapy systems [4, 5, 8, 9, 10, 11]; in particular, MR images are not sensitive to such severe artefacts and are good candidates for the delineation of targets and OARs.

Treatment planning strategies that take into account the presence of hip prostheses have been previously described in literature: in particular, the use of VMAT plans is well established [12, 13, 14, 15].

In this study a new method to deal with b-HP patients who underwent radiotherapy treatment for prostate cancer, based exclusively on Magnetic Resonance Imaging (MRI-only), is proposed. Issues regarding artefacts, EDs mismatch and dosimetry inaccuracy can be faced and more efficiently solved in this way.

MATERIAL AND METHODS

This study concerns a 73-year-old man with an elevate risk acinar adenocarcinoma of the prostate, with a pretreatment Prostate Specific Antigen (PSA) of 10.1ng/mL and a Gleason Pattern Score (GPS) of 4+4=8 and 3+3=6 in the right and left lobe. Considering the high-risk class, androgen deprivation therapy (ADT) consisting of Luteinizing Hormone – Releasing Hormone (LHRH) analogue administration 3 months before the start of RT was essential. Furthermore, the patient has bilateral titanium alloy hip prostheses.

The presence of bilateral prostheses created heavy CT artifacts; for this reason, the classical CT planning approach was not feasible. In order to overcome this problem, MR images with assigned ED were used, thus generating a synthetic CT (sCT) (Fig. 1).

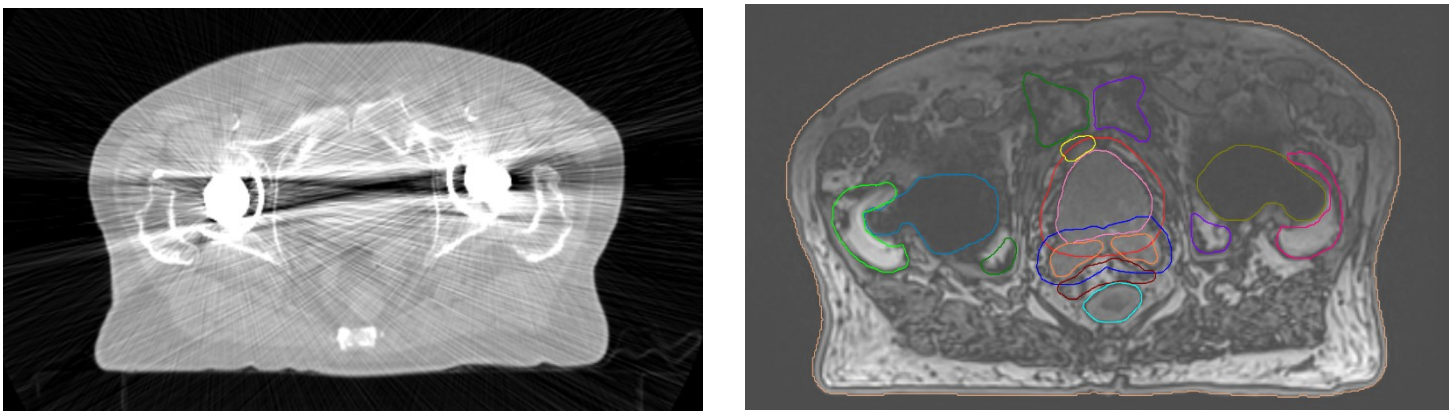

Fig. 1: Comparison between CT images (on the left), characterized by relevant artifacts, and MRI ones, used to generate the sCT for the treatment plan.

The images were acquired on a 1.5 T Siemens Aera MRI scanner (Siemens Healthcare, Erlangen, Germany). During simulation the patient had a full bladder (half liter of water, half an hour before) and was positioned supine over a flat table, with ankle and knee supports to ensure reproducible daily setup. The MRI acquisition was performed by a large field of view (FOV) 3D T1 VIBE Dixon sequence, optimized with a slice thickness of 1 mm and scan time less than 3 minutes [16]; it is a good compromise between image quality and acquisition time, reducing the breathing artifacts, which generally creates distortions in OARs and the discomfort of the patient. In addition, the bandwidth used, equal to 445 Hz/pixel, made it possible to keep the artifacts quite constrained.

Images were contoured by an auto-segmentation software (Admire, research version 1.13.5, Elekta AB, Stockholm, Sweden), based on a deformable image registration algorithm and an MRI internal database of 20 patients, previously subjected to radiological examinations for diagnostic purposes; only the prostheses were contoured manually. All contours (body and OARs) were validated by a senior radiation oncologist. Two Planning Target Volumes (PTV), Prostate gland (PTVp) and Seminal Vesicles (PTVsv), were manually drown by the same radiation oncologist [17, 18]. Then, the sCT was generated by assigning an ED to each contour; these values were averaged on CTs of 20 prostate patients treated in our center over the last year [16]. The ED values of the prostheses were deduced from manufacturer data.

Two competitor VMAT plans with 10MV X-rays, a complete arc (C-arc) and a partial one (P-arc), were calculated by a Monte Carlo based TPS Monaco® (version 5.51, Elekta AB, Stockholm, Sweden),

avoiding as much as possible the prostheses regions [6, 12, 13, 14] and following dose-volume constraints used in our center [18, 19]. The prescribed dose in 30 fractions was 72 Gy for PTVp and 63 Gy for PTVsv [18].

Moreover, the chosen plan calculated on the sCT images was copied using the same field arrangements and recalculated on the same MR images, assigning an ED value equal to 1 in all the region affected by artifacts. In this way the impact of the selected technique was evaluated, compared to the usual choice of contouring the artifacts and assigning them a density equal to that of water.

Finally, the feasibility of matching the daily CBCT and MR reference images was tested, by means of visual evaluations by three different radiation oncologists, after previous verification that the CBCT did not present evident CT-like artifacts. The alignment was made using only translation, considering both the PTV and bones in the manual matching. The acquisition was performed with 120 kV, 660 mAS and medium collimator FOV.

RESULTS

The use of MR images allowed the contouring of targets and OARs, which otherwise would have been very difficult and inaccurate in this case.

In the P-arc plan, the beam entrances through the prostheses have been avoided for about 50° on both sides. Nevertheless, the C-arc plan was chosen; despite the same coverage of both PTVs and a similar OARs sparing, the mean and maximum doses to both prostheses were significantly lower (about 10%). In detail, the target coverage dose of 95% ($V_{95\%D}$) of PTVp and PTVsv were and 98.2% and 100% for the C-arc and 98.9% and 100% for the P-arc, respectively. About OARs, the volumes of rectum and bladder receiving 40 Gy were 35.5% and 34.9% for the C-arc, and 34.7% and 34.9% for the P-arc. Prostheses received a mean dose (D_{mean}) equal to 9.0 Gy (with a maximum dose ($D_{0.035}$) equal to 26.0. Gy) and 8.9 Gy ($D_{0.035}$ 27.4 Gy) in the C-arc, while 9.7 Gy ($D_{0.035}$ 30.4 Gy) and 10.2 Gy ($D_{0.035}$ 29.7 Gy) in the P-arc.

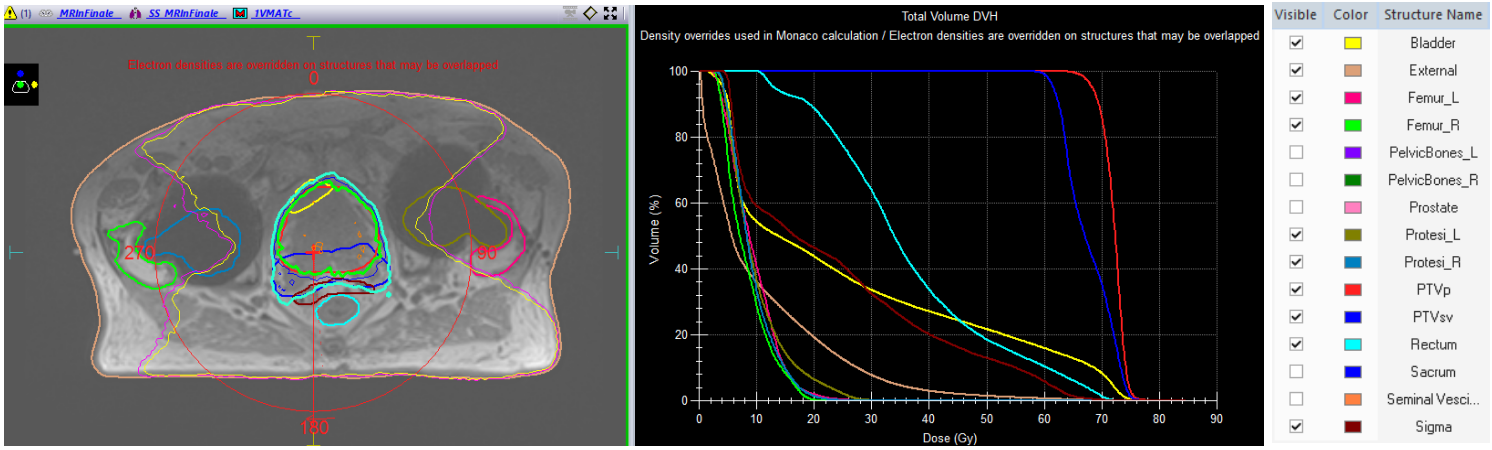

Fig. 2: The final plan chosen: on the left the isodoses' distribution (in green the 95% of the PTVp and in light blue the 95% of the PTVsv), while on the right the corresponding dose volume histogram.

Once selected, the C-arc plan was further optimized in order to improve OARs sparing, as shown in Fig. 2. The D_{95} were 95.0% and 99.3% for PTVp and PTVsv, with an improvement in sparing of rectum

and bladder, whose volumes receiving 40 Gy were 33.8% and 27.1% respectively. The D_{mean} received by the prostheses were 9.7 Gy ($D_{0.035}$ 34.7 Gy) for the left one and 9.1 Gy ($D_{0.035}$ 26.7 Gy) for the right one.
Moreover, for the plans recalculated with the same field arrangements on the MR images, where an ED value equal to that of water was assigned in all the region affected by artifacts, the doses were significantly higher. In fact, the $V_{95\%D}$ of PTVp and PTVsv in this case were 4.0% and 0.5% higher than the previously values. Furthermore, the volumes of rectum and bladder receiving 40 Gy were 35.1% and 27.8%, respectively 4.1% and 2.7% more.
Finally, the match between CBCT and MR images for re-positioning purpose was manually done by the same radiation oncologists, who considered the sCT image quality acceptable in different fractions, despite the apex of the prostate was affected by some streak artifacts in CBCT Images. The average obtained shifts were 8 mm, -2 mm and 9 mm in lateral, longitudinal and vertical directions, with standard deviations equal to 1 mm, 2 mm and 2 mm respectively. This could be explained considering the limited quality of CBCT in this bilateral hip prostheses case, and besides considering that between the MR imaging and the RT several weeks have passed.

DISCUSSIONS

The difficulties in CT-planning for patients with implanted metal hip prosthesis are well known, both as regards the delineation of volumes and the calculation of the dose distribution by the TPS [3, 4, 5, 6, 13, 15]. These aspects are even more significant for patients with b-HP. As a matter of fact, the first issue concerns the presence of relevant artifacts in CT images, which makes the classical CT-planning procedure unfeasible, especially in the prostate region. There are some alternatives reported in literature [4, 5, 8, 9, 10, 11]; the most suitable one is the use of the MVCT on Tomotherapy system. The delineation of the volumes of interest is possible thanks to the use of energy in the mega voltage range; the artifacts region is then contoured and a fixed ED of 1 is assigned to it. Anyhow, the use of MR images is certainly a good solution, since the volumes of interest are more clearly visible and consequently smaller than those contoured on CT images, up to 20% [4, 5]. The advantage of the method proposed in this work is that it does not require any registration between CT and MR images. In addition, the EDs of sCT used in this work for planning purposes are more accurate than those emerging from CT images, heavily compromised by metal artifacts. In fact, in those regions each structure has an assigned ED, in contrast to the usual choice to attribute a density equal to water in the whole compromised region [5, 7, 13, 14].
Another relevant aspect is related to the dosimetric evaluation. Nowadays, inverse planning, in particular VMAT technique, is considered a standard also for this kind of patients [13, 14, 15, 20], since it is possible to avoid the prostheses region as recommended in literature [3, 6]. Moreover, the dose attenuation through the titanium prostheses is better modeled than in the past inside modern MonteCarlo based TPSs [21, 22].
The use of MR images allowed radiotherapy to be performed, which otherwise would not have been considered as a possible treatment for this patient, since it was not possible to contour the volumes of interest on the CT images.
The complete arc was chosen over the partial one since the mean and maximum dose to both the prostheses were lower, with the same coverage of the PTVs and with the same OARs sparing. There is no indication of a maximum permitted dose in literature, but it is recommended to keep the doses

to the prosthesis as low as possible [6]. The doses received by the prostheses, 9.7 Gy ($D_{0.035}$ 34.7 Gy) for the left one and 9.1 Gy ($D_{0.035}$ 26.7 Gy) for the right one, are equal or slightly higher, comparing our study with other works, with a similar dose prescription [7, 13, 15]; respecting this proposal, we prefer to spare as much as possible the rectum and the bladder, whose volumes receiving 40 Gy were 33.8% and 27.1% respectively.
Furthermore, even if the volumes of interest were identified with the help of MR images, the uncertainty obtained by assigning to artifacts a density equal to that of water in such a large region would have led to a dosimetric uncertainty equal to 3- 4% more both in the target and in the main organs at risk. In this way, the resulting plan would lead to significant under-dosage, which could compromise the outcome of the treatment.

Sctructure	DVH Parameter	sCT	sCT (ED=1)	% Difference
PTV (Prostate Gland)	$V_{95\%D}$ (%)	95.00	98.82	**4.0**
PTV 2 (Seminal Vesicles)	$V_{95\%D}$ (%)	99.30	99.80	**0.5**
Bladder	V40 (%)	27.10	27.80	**2.7**
Rectum	V40 (%)	33.80	35.10	**4.1**

Fig. 3: List of mean deviations of DVH parameters for PTV and between the plan calculated on the sCT, considered as standard, and the one obtained with the same MR images but assigning an ED equal to 1 to all the region affected by artifacts.

At the end, the match feasibility for in room-verification, using MR images instead of classical CTs, was verified. This process was previously tested with images of other patients, not affected by artifacts, by comparing the shifts of CBCT-CT match with those obtained by CBCT-MR one. In this case this was not possible: the feasibility was based on visual evaluations of three different radiation oncologists. They considered acceptable the quality of the images, also in the critical central area of the FOV, without the need to implant metal markers in the prostate. In addition, the standard deviations of averaged shifts over 10 fractions resulted within 2 mm in all directions.

CONCLUSION

The proposed method seems to be promising for those double prostheses prostate patients who otherwise would not have easily access to radiotherapy treatment, showing agreement with the CT-based workflow, both in terms of dosimetry and regarding image guided radiation therapy.

ADDENDUM REFERENCES

[1] Torre M, Carrani E, Luzi I, Ceccarelli S, Laricchiuta P. Registro italiano ArtroProtesi. Report Annuale 2018. Il Penisero Scientifico Editore 2018.

[2] Siegel R L, Miller K D, Jemal A. Cancer Statistics, 2020. CA Cancer J. Clin. 2020; 70(1): 7-30. https://doi:10.3322/caac.21590

[3] Eng T Y. Dose attenuation through a titanium alloy hip prosthesis. Med. Dosim. 2000; 25(1): 7-8. https://doi:10.1016/s0958-3947(99)00021-7

[4] Rosewall T, Kong V, Vesprini D, Catton C, Chung P, Menard C, Bayley A. Prostate delination using CT and MRI for radiotherapy patients with bilateral hip prostheses. Radiother. Oncol. 2009; 90:325-30. https://doi:10.1016/j.radonc.2008.11.015

[5] Charnley N, Morgan A, Thomas E, Wilson S, Bacon S, Wilson D, Bottomley D. The use of CT-MR image registration to define target volumes in pelvic radiotherapy in the presence of bilateral hip replacements. Brit. J. Radiol. 2005; 78: 634-36. https://doi:10.1259/bjr/28412864

[6] Reft C, Alecu R, Das IJ, et al. Dosimetric considerations for patients with HIP prostheses undergoing pelvic irradiation. Report of the AAPM Radiation Therapy Committee Task Group 63. Med. Phys. 2003;30:1162–82. https://doi:10.1118/1.1565113

[7] James L. Prostate irradiation in patients with hip prostheses – a retrospective analysis. J. Radiother. Pract. 2006; 5: 147-156. https://doi:10.1017/S1460396906000203

[8] Aubin M, Morin O, Chen J, Gillis A, Pickett B, Aubry J F, Akazawa C, Speight J, Roach III, Pouliot J. The use of Megavoltage Cone-Beam CT to Complement CT for Target Definition in Pelvic Radiotherapy in the Presence of Hip Replacement. Br. J. Radiol. 2006; 79(947): 918-21. https://doi:10.1259/bjr/19559792

[9] Falcinelli L, Palumbo I, Radicchia V, Arcidiacono F, Lancellotta V, Montesi G, Matrone F, Zucchetti C, Marcantonini M, Bini V, Aristei C. Prostate cancer: contouring target and organs at risk by kilovoltage and megavoltage CT and MRI in patients with and without hip prosthese. Br. J. Radiol. 2015; 88 20150509. https://doi:10.1259/bjr.20150509

[10] Chapman D, Smith S, Barnett R, Bauman G, Yartsev S. Optimization of tomotherapy treatment planning for patients with bilateral hip prostheses. Radiat. Oncol. J. 2014;9:43. http://www.ro-journal.com/content/9/1/43

[11] Kling J, Patel K M. Prostate treatment with helical TomoTherapy in patients with bilateral hip prostheses-Two case studies. Med. Dosim. 2013;38:30-34. http://dx.doi.org/10.1016/j.meddos.2012.05.003

[12] Ng W L, Brunt J, Temple S, Saipillai, Haridass A, Wong H, Malik Z, Eswar C. Volumetric modulated arc therapy in prostate cancer patients with metallic hip prostheses in a UK center. Rep. Pract. Oncol. Radiother. 2015; 20: 273-77. https://dx.doi.org/10.1016/j.rpor.2015.03.006

[13] Prabhakar R, Kumar M, Cheruliyil S, Jayakumar S, Balasubramanian S, Cramb J. Volumetric modulated arc therapy for prostate cancer patients with hip prosthesis. Rep. Pract. Oncol. Radiother. 2013; 18: 209-213. https://dx.doi.org/10.1016/j.rpor.2013.03.006

[14] Rana S B, Pokharel S. A dosimetric study of volumetric modulated arc therapy planning techniques for treatment of low-risk prostate cancer in patients with bilateral hip prostheses. South Asian J Cancer 2012; 56: 703-07. https://doi: 10.1111/j.1754-9485.2012.02456.x

[15] SuA,Reft C, Rash C, Price J, Jani A B. A case study of radiotherapy planning for a bilateral metal hip prosthesis prostate cancer patient. Med. Dosim. 2005;30(3):169-175. https://doi:10.1016/j.meddos.2005.06.001

[16] Nici S, Monti A F, Lizio D, Pellegrini R, Brambilla M G, Carbonini C, Arias Garces M J, Felisi M M J, Bortolato B, Frassica C, Coletti C, Vanzulli A, Torresin A. MRI-only in prostate radiotherapy planning using multiple individual atlates: a preliminary study. ESTRO 2020. PH-0412.

[17]Gay H A, Barthold H J, O'Meara E, Bosch W R, El Naqa I, Al-Lozi R, Rosenthal S A, Lawton C, Lee W R, Sandler H, Zietman A, Myerson R, Dowson L A, Willet C, Kachnic L, Jhingran A, Portelance L, Ryu J, Small Jr W, Gaffney D, Viswanathan A N, Michalski J M. Pelvic normal tissue contouring guidelines for radiation therapy: aRadiation Therapy Oncology Group consensus panel atlas. Int. J. Radiat. Oncol. Biol. Phys. 2012; 83(3): e353-62. https:/doi:10.1016/j.ijrobp.2012.01.023.

[18] Santoni R, Arcangeli S, Ingrosso G, Antognoni P, Mazzeo E, D'angelillo RM, Buglione M, Borghesi S, Petitti T, Orecchia R. Linee guida Carcinoma della Prostata – AIRO, 2016. Tumori J 2016; 102: S1-S79.https://doi.org/10.5301/TJ.2016.15934

[19] Chennupati S K, Pelizzari C A, Kunnavakkam R, Liauw S L. Late toxicity and quality of life after definitive treatment of prostate cancer: redefining optimal rectal sparing constraints for intensity-modulated radiation therapy. Cancer Med. 2014; 3(4): 954-61. https://doi:10.1002/cam4.261

[20] Martin D A, Hruby G, Whitaker M K, Foo K Y-M. Constrained-beam inverse planning for intensity-modulated radiation therapy of prostate cancer patients with bilateral hip prostheses. J. Med. Imag. Radiat. On. 2012; 56: 703-07. https://doi:10.1111/j.1754-9485.2012.02456.x

[21] Han T, Mikell J K, Salehpour M, Mourtada F. Dosimetric comparison of Acuros XB deterministic radiation transport method with MonteCarlo and model-based convolution methods in heterogeneous media. Med. Phys. 2011; 38(5): 2651-2664. https://doi:10.1118/1.3582690.

[22] Snyder J E, Hyer D E, Flynn R T, Boczkowski A, Wang D. The commissioning and validation of Monaco treatment planning system on an Elekta VersaHD linear accelerator. J Appl. Clin. Med. Phys. 2019; 20:1: 184-193. https://doi:10.1002/acm2.12507

ACKNOWLEDGMENTS

Desidero per prima cosa ringraziare tutti coloro che hanno collaborato alla realizzazione di questo lavoro di tesi, rendendolo possibile.
Ringrazio la S.C. Fisica Sanitaria, in particolar modo il Dott. Torresin, il Dott. Lizio ed il Dott. Monti per i preziosi consigli ed il continuo supporto nelle diverse fasi di questo lavoro. Un particolare ringraziamento va alla Dott.ssa Nici, che con passione e tenacia ha avviato questo progetto: i tuoi suggerimenti sono stati fondamentali.
Un grazie speciale va al Dott. Pellegrini di Elekta per l'entusiasmo e la propositività che hanno contraddistinto questi mesi di lavoro insieme, e per aver messo a disposizione le soluzioni software, fondamentali per la realizzazione della tesi.
Vorrei poi ringraziare la S.C Radioterapia; grazie al Dott. Palazzi, che si è mostrato disponibile allo sviluppo di questo progetto, alla Dott.ssa Bortolato, che con interesse e curiosità mi ha consigliato in diverse occasioni, alla Dott.ssa Potente, per aver eseguito (sempre con il sorriso) le acquisizioni sui pazienti ed infine alla Dott.ssa Sibio e alla Dott.ssa Carsana per la loro generosa disponibilità.
Un sentito grazie va anche a tutta la S.C Radiologia, dal Professor Vanzulli per aver permesso di realizzare questo lavoro, al Dott. Frassica e a tutti i tecnici di radiologia per le acquisizioni RM effettuate.

Tre anni sono lunghi e, come per ogni percorso nella vita, è decisamente più fortunato chi ha il piacere di condividerlo piuttosto che farlo in solitaria.
In questo senso, il ringraziamento più importante va certamente ai miei genitori, a mio fratello Luca e a tutta la mia famiglia, che mi ha incoraggiato e sostenuto, credendo sempre in me.
Un grazie di cuore va agli amici di sempre e quelli incontrati durante questo percorso, per aver fatto in modo che affrontassi ogni ostacolo con il sorriso.
Infine, un enorme grazie va a tutta la Fisica Sanitaria, che mi ha fatto sentire a casa sin dal primo giorno e mi ha permesso di imparare moltissimo, sia sul piano lavorativo, sia umano. Grazie di cuore!
Un grazie speciale va agli specializzandi incontrati in questi anni, amici più che colleghi, con cui ho avuto piacere di condividere tempo al lavoro e fuori, divertendomi.
Un ringraziamento finale va a chi è nel mio cuore, sempre. È anche grazie a tutti voi se sono riuscito a portare a termine questo percorso.